

This is to certify that the thesis entitled

THE METAL FLUX SYNTHESIS AND CRYSTAL GROWTH OF BINARY AND TERNARY BORIDES

presented by

Britt Andrew Vanchura II

has been accepted towards fulfillment of the requirements for the

M.S. degree in Chemistry

Major, Professor's Signature

Date

MSU is an Affirmative Action/Equal Opportunity Institution

LIBRARY Michigan State University

PLACE IN RETURN BOX to remove this checkout from your record. TO AVOID FINES return on or before date due. MAY BE RECALLED with earlier due date if requested.

DATE DUE	DATE DUE	DATE DUE

2/05 p:/CIRC/DateDue.indd-p.1

THE METAL FLUX SYNTHESIS AND CRYSTAL GROWTH OF BINARY AND TERNARY BORIDES

Ву

Britt Andrew Vanchura II

A THESIS

Submitted to
Michigan State University
in partial fulfillment of the requirements
for the degree of

MASTER OF SCIENCE

Department of Chemistry

2006

ABSTRACT

THE METAL FLUX SYNTHESIS AND CRYSTAL GROWTH OF BINARY AND TERNARY BORIDES

By

Britt Andrew Vanchura II

Borides form a large class of compounds with diverse structural and physical properties. Traditionally, high-temperature furnaces, arc welders, and radiofrequency (RF) induction furnaces have been used to reach the elevated synthesis temperatures of most borides. By using a low-melting point metal as a solvent-like flux, the reaction temperatures for boride synthesis can be lowered by several hundred degrees. Our group has recently had success using molten gallium to synthesize the new borides $RE_{3-x}C_2Si_8(B_{12})_3$ (RE = Tb and Er) and β -SiB₃, which are only obtainable through flux synthesis. Literature searches have found that molten copper and aluminum have also been used successfully as fluxes for the synthesis and crystal growth of many borides.

In the present work we expanded the use of gallium as a metal flux by synthesizing and growing crystals of borides in the Cr-B, Mo-B, W-B, Mn-B, Re-B, Ho-Mn-B, and RE-Re-B (RE = Dy, Er, Yb) systems. Molten copper was used to synthesize borides from the Cr-B, Ru-B, and RE-Ru-B systems. Structural characterization by single crystal x-ray diffraction was carried out on all borides produced from the metal fluxes. The structures of the borides and general observations on the metal flux technique and its applications to boride synthesis are discussed.

Copyright by

Britt Andrew Vanchura II

2006

ACKNOWLEDGEMENTS

I would like to thank my wife Jaime for being the wonderful person that she is.

Nobody could be more supportive, encouraging, and understanding. My daughter

Caroline has been an inspiration. Even on the bad days she's there to great me with a "Da!" and hug. I could never thank my parents enough for all that they have done. I thank God everyday for giving me such a loving family.

I would like to thank my advisor, Mercouri Kanatzidis, for all his help, support, and advice. The help and support from past and present Kanatzidis group members is greatly appreciated. The support staff in the chemistry department has been a tremendous help, even when things were more than a little crazy.

TABLE OF CONTENTS

LIST OF TAI	BLES	viii
LIST OF FIG	URES	xiii
LIST OF ABI	BREVIATIONS	xv
Chapter One	The Metal Flux Technique in Boride Synthesis A. Introduction B. The Metal Flux Technique C. Structural Features in Borides D. Chemical and Physical Properties of Borides	1 1 5
Chapter Two	References The Metal Flux Synthesis of Group Six Borides A. Introduction B. Experimental Reagents Furnaces Synthesis and Isolation Cr ₅ B ₃ Cr ₃ B ₄ Cr ₂ B ₃ Cr _{B₂} MoB WB C. Physical Measurements Energy Dispersive Spectroscopy Single Crystal X-ray Crystallography D. Structural Description Cr ₅ B ₃ Cr ₃ B ₄ Cr ₂ B ₃ Cr ₅ B ₂ MB (M= Mo, W) E. Results and Discussion F. Conclusions References	1315151717171919202121383838383838
Chapter Three	The Metal Flux Synthesis of Group Seven Borides A. Introduction B. Experimental Reagents Furnaces	48 49 49 50
	Synthesis and Isolation	51

	MnB	51
	MnB_4	52
	ReB ₂	52
	HoMnB ₄	53
	$REReB_4$ (RE = Dy, Er, Yb)	54
	C. Physical Measurements	
	Energy Dispersive Spectroscopy	
	Single Crystal X-ray Crystallography	
	D. Structural Description	
	MnB	
	MnB ₄	
	ReB ₂	
	HoMnB ₄ and REReB ₄ (RE = Dy, Er, Yb)	
	E. Results and Discussion	
	MnB	
	MnB ₄	
	ReB ₂	
	HoMnB ₄	
	·	
	REReB ₄ (RE = Dy, Er, Yb)	
	General Discussion	
	F. Conclusions	
	References	84
Ola A A A	The Market Condition of the Condition of	0.6
Chapter Four	The Metal Flux Synthesis of Ruthenium Borides	
	A. Introduction	
	B. Experimental	
	Reagents	
	Furnaces	
	Synthesis	
	Ru_7B_3 , Ru_2B_3 , and RuB_2	
	β -RuB ₂	
	$RERu_4B_4$ (RE = Y, Ce, Sm, Dy, Yb)	
	$RE_x(Ru_4B_4)_y$ (RE = Pr, Nd)	90
	Isolation from flux	90
	C. Physical Measurments	91
	Energy Dispersive Spectroscopy	91
	Single Crystal X-ray Crystallography	92
	D. Structural Description	
	Ru ₇ B ₃	
	Ru_2B_3	110
	RuB_2	
	β-RuB ₂	
	$RERu_4B_4$ (RE = Y, Ce, Sm, Dy, Yb)	
	E. Results and Discussion	
	F. Conclusions.	
	References	
	7.47.47.47.40.0000000000000000000000000	

Chapter Five	Gallium-Rich Gallides Isolated as By-Products from Molten Flux	
React	ons Containing Boron	123
	A. Introduction	
	B. Experimental	124
	Reagents	
	Furnaces	
	Synthesis and Isolation	124
	MnGa _{4.65}	124
	ReGa _{4.5}	
	Ni _{0.57} Ga _{4.43}	126
	C. Physical Measurements	127
	Energy Dispersive Spectroscopy	127
	Single Crystal X-ray Crystallography	127
	D. Structural Description	136
	MGa _{4+x} (M= Mn,Re)	136
	Ni _{0.57} Ga _{4.43}	140
	E. Results and Discussion	142
	F. Conclusions	144
	References	145
Chapter Six	Conclusions and Future Work	146
-	References	150
Appendix	RF Furnace Design and Setup	151

LIST OF TABLES

Table 2-1.	Crystal data and structure refinement for Cr ₅ B _{3.}	24
Table 2-2.	Atomic coordinates (x 10 ⁴) and equivalent isotropic displaceme	nt
	parameters (Å ² x 10 ³) for Cr ₅ B ₃ .	25
Table 2-3.	Anisotropic displacement parameters (Å ² x 10 ³) for Cr ₅ B ₃ .	25
Table 2-4.	Bond distances (Å) for Cr ₅ B ₃ .	26
Table 2-5.	Crystal data and structure refinement for Cr ₃ B ₄ .	27
Table 2-6.	Atomic coordinates (x 10 ⁴) and equivalent isotropic displacement	
	parameters (Å ² x 10 ³) for Cr ₃ B ₄ .	28
Table 2-7.	Anisotropic displacement parameters (Å ² x 10 ³) for Cr ₃ B ₄ .	28
Table 2-8.	Bond distances (Å) for Cr ₃ B ₄ .	29
Table 2-9.	Crystal data and structure refinement for Cr ₂ B ₃ .	30
Table 2-10.	Atomic coordinates (x 10 ⁴) and equivalent isotropic displacement	nt
	parameters ($Å^2x 10^3$) for Cr_2B_3 .	31
Table 2-11.	Anisotropic displacement parameters ($Å^2x\ 10^3$) for Cr_2B_3 .	31
Table 2-12.	Bond distances (Å) for Cr ₂ B ₃ .	32
Table 2-13.	Crystal data and structure refinement for CrB ₂ .	33
Table 2-14.	Atomic coordinates (x 104) and equivalent isotropic displacem	ent
	parameters ($Å^2x 10^3$) for CrB ₂ .	34
Table 2-15.	Anisotropic displacement parameters (Å ² x 10 ³) for CrB ₂ .	34
Table 2-16.	Bond distances (Å) for CrB ₂ .	34
Table 2-17.	Crystal data and structure refinement for MoB and WB.	35

Table 2-18.	Atomic coordinates (x 10 ⁴) and equivalent isotropic displacement	
	parameters (Å ² x 10 ³)for MoB and WB.	36
Table 2-19.	Anisotropic displacement parameters (Å2x 103) for MoB and W	Ъ. 36
Table 2-20.	Bond distances (Å) for MoB.	37
Table 2-21.	Bond distances (Å) for WB.	37
Table 3-1.	Crystal data and structure refinement for MnB.	58
Table 3-2.	Atomic coordinates (x 104) and equivalent isotropic displacement	
	parameters (Å ² x 10 ³) for MnB.	59
Table 3-3.	Anisotropic displacement parameters (Å ² x 10 ³) for MnB.	59
Table 3-4.	Bond distances (Å) for MnB.	59
Table 3-5.	Crystal data and structure refinement for MnB ₄ .	60
Table 3-6.	able 3-6. Atomic coordinates (x 104) and equivalent isotropic displacer	
	parameters (Å ² x 10 ³) for MnB ₄ .	61
Table 3-7.	Anisotropic displacement parameters (Å ² x 10 ³) for MnB ₄ .	61
Table 3-8.	Bond distances (Å) for MnB ₄ .	61
Table 3-9.	Crystal data and structure refinement for ReB ₂ .	62
Table 3-10.	Atomic coordinates (x 104) and equivalent isotropic displacement	ent
	parameters ($Å^2x$ 10 ³) for ReB ₂ .	63
Table 3-11.	Anisotropic displacement parameters (Å ² x 10 ³) for ReB ₂ .	63
Table 3-12.	Bond distances (Å) for ReB ₂ .	63
Table 3-13.	Crystal data and structure refinement for HoMnB ₄ .	64
Table 3-14.	Atomic coordinates (x 104) and equivalent isotropic displacement	nent
	parameters (Å ² x 10 ³) for HoMnB ₄ .	65

Table 3-15.	Anisotropic displacement parameters (Å ² x 10 ³) for HoMnB ₄ .	65
Table 3-16.	Crystal data and structure refinement for REReB ₄ (RE= Dy, Er)	66
Table 3-17.	Crystal data and structure refinement for YbReB ₄ .	67
Table 3-18.	Atomic coordinates (x 104) and equivalent isotropic displacement	
	parameters ($Å^2x$ 10 ³) for REReB ₄ (RE = Dy, Er, Yb).	68
Table 3-19.	Anisotropic displacement parameters (Å ² x 10 ³) for REReB ₄ (RE	= Dy,
	Er, Yb).	69
Table 3-20.	Bond distances (Å) for $HoMnB_4$ and $REReB_4$ ($RE = Dy$, Er , Yb).	70
Table 4-1.	Crystal data and structure refinement for Ru ₇ B ₃ .	95
Table 4-2.	Atomic coordinates (x 104) and equivalent isotropic displacement	nt
	parameters ($Å^2x 10^3$) for Ru_7B_3 .	96
Table 4-3.	Anisotropic displacement parameters (Å ² x 10 ³) for Ru ₇ B ₃ .	96
Table 4-4.	Selected bond distances (Å) for Ru ₇ B ₃ .	97
Table 4-5.	Crystal data and structure refinement for Ru ₂ B ₃ .	98
Table 4-6.	Atomic coordinates (x 104) and equivalent isotropic displacemen	nt
	parameters ($Å^2x 10^3$) for Ru_2B_3 .	99
Table 4-7.	Anisotropic displacement parameters (Å ² x 10 ³) for Ru ₂ B ₃ .	99
Table 4-8.	Selected bond distances (Å) for Ru ₂ B ₃ .	99
Table 4-9.	Crystal data and structure refinement for RuB ₂ .	100
Table 4-10.	Atomic coordinates (x 104) and equivalent isotropic displacemen	nt
	parameters ($Å^2x 10^3$) for RuB ₂ .	101
Table 4-11.	Anisotropic displacement parameters (Å ² x 10 ³) for RuB ₂ .	101
Table 4-12.	Selected bond distances (Å) for RuB ₂ .	101

Table 4-13.	Crystal data and structure refinement for β -RuB ₂ .	102
Table 4-14.	Atomic coordinates (x 104) and equivalent isotropic displacement	
	parameters (Å ² x 10 ³) for β -RuB ₂ .	103
Table 4-15.	Anisotropic displacement parameters ($Å^2x$ 10 ³) for β -RuB ₂ .	103
Table 4-16.	Selected bond distances (Å) for β-RuB ₂ .	103
Table 4-17.	Crystal data and structure refinement for RERu ₄ B ₄ (RE= Y, Ce).	104
Table 4-18.	Crystal data and structure refinement for RERu ₄ B ₄ (RE= Sm, Dy)	. 105
Table 4-19.	Crystal data and structure refinement for YbRu ₄ B ₄ .	106
Table 4-20.	Atomic coordinates (x 104) and equivalent isotropic displaceme	nt
	parameters ($Å^2x$ 10 ³) for RERu ₄ B ₄ (RE = Y, Ce, Sm, Dy, Yb).	107
Table 4-21.	Anisotropic displacement parameters (Å ² x 10 ³) for RERu ₄ B ₄ (RE	z = Y,
	Ce, Sm, Dy, Yb).	108
Table 4-22.	Bond distances (Å) for RERu ₄ B ₄ (RE = Y, Ce, Sm, Dy, Yb).	109
Table 5-1.	Crystal data and structure refinement for MnGa _{4.65} and ReGa _{4.5} .	130
Table 5-2.	Atomic coordinates (x 10 ⁴) and equivalent isotropic displacement	
	parameters ($Å^2x$ 10 ³) for MnGa _{4.65} and ReGa _{4.5} .	131
Table 5-3.	Anisotropic displacement parameters (Å ² x 10 ³) for MnGa _{4+x} and	
	ReGa _{4+x} .	132
Table 5-4.	Bond distances (Å) for MnGa _{4.65} and ReGa _{4.5} .	133
Table 5-5.	Crystal data and structure refinement for Ni _{0.57} Ga _{4.43} .	134
Table 5-5.	Atomic coordinates (x 104) and equivalent isotropic displacement	
	parameters (Å 2 x 10 3) for Ni _{0.57} Ga _{4.43} .	135
Table 5-7.	Anisotropic displacement parameters (Å ² x 10 ³) for Ni _{0.57} Ga _{4.43} .	135

LIST OF FIGURES

Figure 1-1.	1. Various geometric arrangements of boron atoms in borides: (a) isol		
	atoms (B:M < 0.5), (b) isolated pairs (B:M \approx 0.67), (c) zigzag cha	ain	
	(B:M = 1), (d) double chain (B:M \approx 1.3), (e) triple chain (B:M = 1.5), (f)		
	two-dimensional network ($2.0 \le B:M \le 2.5$).	6	
Figure 2-1	(a) Representation of Cr ₅ B ₃ along the b-axis (b) Boron pairs in Cr	r ₅ B ₃ (Cr	
	atoms omitted for clarity).	39	
Figure 2-2.	Double and triple chains of boron atoms in (a) Cr ₃ B ₄ and (b) Cr ₂ B ₃ ,		
	respectively.	40	
Figure 2-3.	(a) CrB ₂ structure seen along c-axis (b) Planar-nature of boron layers in		
	CrB ₂ .	42	
Figure 2-4.	Structure of MB (M = Mo, W) viewed down the b-axis	43	
Figure 3-1.	(a) Structure of CrB-type MnB with boron atom chains parallel to page.		
	The boron atom chains are perpendicular to the page in (b) FeB-type MnB		
	and (c) CrB-type MnB.	72	
Figure 3-2.	(a) The structure of MnB ₄ viewed down the a-axis (b) Sheet of I	acture of MnB ₄ viewed down the a-axis (b) Sheet of RuB ₂	
	with similarly puckered hexagonal sheets of B atoms.	73	
Figure 3-3.	(a) Structure of ReB ₂ and (b) an individual graphite-like layer of	boron	
	atoms.	75	
Figure 3-4.	(a) Structure of YCrB ₄ -type compounds (b) View down a-axis sh	owing	
	alternating layers of metal atoms and boron atoms.	76	
Figure 3-5.	SEM micrograph of a MnB ₄ crystal.	79	

Figure 3-6.	SEM micrograph of a cluster of ReB ₂ crystals.	79
Figure 3-7.	SEM micrograph of HoMnB ₄ .	81
Figure 3-8.	SEM micrograph of DyReB ₄ .	81
Figure 4-1.	(a) Structure of Ru ₇ B ₃ and (b) the stellaquadrangula building unit.	. 111
Figure 4-2.	(a) Structure of Ru ₂ B ₃ and the (b) puckered boron layer and (c) plana	
	layer of boron atoms.	112
Figure 4-3.	Structure of RuB ₂ crystallizing with the (a) RuB ₂ -type and (b) ReB ₂ -type	
	structures.	113
Figure 4-4.	Structure of RERu ₄ B ₄ (RE = Y, Ce, Sm, Dy, Yb) shown down	
	the b-axis.	115
Figure 4-5.	SEM micrographs of (a) RuB ₂ and (b) β-RuB ₂ .	117
Figure 4-6.	SEM micrographs of (a) CeRu ₄ B ₄ and (b) CeRuB ₄ .	119
Figure 5-1.	Structure of MGa _{4+x} (M = Mn, Re) viewed down the c -axis.	137
Figure 5-2.	View down the c-axis of (a) MnGa _{4.5} and (b) PdGa ₅ .	138
Figure 5-3.	Connectivity along the c-axis in (a) MGa _{4+x} and (b) PdGa ₅ .	139
Figure 5-4.	(a) Structure of $Ni_{0.57}Ga_{4.43}$ and (b) the parent γ -brass structure.	141
Figure 5-5.	SEM micrographs of (a) MnGa ₄ and (b) ReGa _{4.5} .	143
Figure A-1.	Cross-sectional view of (a) BN susceptor holder and Mo susceptor	along
	(b) vertical and (c) horizontal axes.	153
Figure A-2.	General setup for RF furnace.	154

LIST OF ABBREVIATIONS

CCD Charge Coupled Device

SEM Scanning Electron Microscope

EDS Energy Dispersive Spectroscopy

RF Radio Frequency

CHAPTER ONE

The Metal Flux Technique in Boride Synthesis

A. Introduction

The metal flux technique is an interesting alternative to traditional solid state synthesis techniques. Low melting point metals are used as a solvent in this technique to facilitate greater diffusion of the reagents and to aid in single crystal growth. The application of the flux technique to the synthesis of borides has had some success, but the potential seems to be much greater. An examination of the metal flux technique, basic boride structural features, and properties of note for borides is presented.

B. The Metal Flux Technique

Solid state synthesis often requires the use of high temperature equipment.

Traditionally, high-temperature furnaces, arc welders, and radio frequency (RF) induction furnaces have been used to reach the elevated temperatures at which synthesis takes place. While working at elevated temperatures may be required for any reaction to take place, it can also be very limiting. A desired ternary phase may be inaccessible in a system of reagents because more thermodynamically stable binary phases are formed. Efforts to combat binary formation include frequent grinding and reheating of reagents, using less-stable binary or ternary phase starting materials, and using very long annealing steps in heating profiles. The metal flux technique is a practical alternative to the traditional solid state techniques.

The metal flux technique makes use of a metal with a relatively low melting point, in which the reagents of interest have some solubility, to act as a solvent for the reaction. The melting point of the metal need only be low in relation to the other reagents in use. For instance, copper, with a melting point of 1092 °C has been used successfully as a flux for many different systems containing metals with higher melting points from the d- and f-blocks. The liquid metal flux acts as a solvent and often allows for greater diffusion of the reagents, which allows the reagents to react at temperatures well below their melting points. The lower reaction temperature allows crystals to grow with fewer defects, a boon when the crystals are going to be used in properties measurements.²

Another advantage to using a metal flux is that the fluxes can getter impurities from a reaction environment, allowing a clean environment for crystal growth.³ This advantage is easily overlooked, but ensures a critical oxygen-free environment.

Generally flux reactions are run at lower temperatures, so the reactivity of the reagents with oxygen is already less than that found in traditional techniques. Because most flux reactions have a large excess of the flux metal, oxygen, or any other impurity, is much more likely to react with the flux metal than the intended reagents.

Disadvantages do exist in the use of metal fluxes. At times, finding an appropriate metal in which the reagents are soluble can be difficult or impossible. Because the flux is soluble with so many materials there can be unexpected incorporation of reaction vessel materials into the reactions. We have found that tantalum and quartz tubes react too readily with gallium and copper and are destroyed by these fluxes. Yet, the most challenging part of using the flux may be in how to extract the reaction products

from the solvent-like flux. These problems must be taken into consideration when attempting a new molten metal flux synthesis.

Our group has implemented the metal flux in exploratory synthesis for many multinary systems. Many new alumindes, 4,5 silicides, 6,7 and germanides 8,9 were found, which led to interest in extending the technique to systems including boron. Initial successes included the synthesis of a new binary phase, β -SiB₃, 10 and a series of quaternary phases, RE_{1.8}C₂Si₈(B₁₂)₃ (RE= Y, Tb, Er). Further inspection of the literature showed that metal fluxes have been used successfully for the synthesis and growth of quite a few borides. $^{12-23}$

The first reports of growth of borides from molten metals dealt with mixtures of iron and aluminum as the flux metals. ¹² Iron melts near 1500 °C, but aluminum melts at only 660 °C, and boils near 2500 °C, which allows researchers a very large, and easily attainable, temperature range in which to carry out experiments. Using aluminum as the flux metal also allows the use of more accessible oxide starting reagents because the aluminum can reduce the oxides to elemental reagents while in the flux. ¹³ The advantage of using these oxides is that the preparation for synthesis can be done out on a bench top, rather than inside a glovebox. These advantages made aluminum the flux metal of choice for borides. It has produced crystals of many different borides, ranging from simple binary borides ¹⁴⁻¹⁷ to ternaries that include aluminum. ¹⁸

One of the main problems with using aluminum as the flux metal is that it makes stable binaries, not only with many metals, but also with boron. Aluminum diboride is a common side product in flux reactions, and we have found at least three different aluminum dodecaborides that form from reactions rich in aluminum and boron. There

have been no reports of true ternary borides grown from an aluminum flux that do not include aluminum in the structure. To make ternaries that do not incorporate aluminum, other metals must be used as the flux.

Copper has been used with some success in the flux growth of binary crystals in the Nb-B¹⁹ and W-B²⁰ systems. In the last decade the use of a copper flux was extended to ternary RE-Rh-B²¹ and RE-B-C²² systems and quaternary RE-Rh-B-C²³ and RE-B-C-N²² systems. An advantage to using copper over aluminum is that there are no known Cu-B binaries to inhibit other borides from forming. Disadvantages to using copper include its high melting temperature (1092 °C) and the inability to use oxides as reagents.

Our group has found gallium to be a useful flux metal in the synthesis of RE-B-Si-C and Si-B compounds. After having difficulty isolating aluminum-free ternary silicides from an aluminum flux, our group moved to gallium and found that gallium stayed out of the ternary phases. Seeing that aluminum was also incorporated into many borides, we again moved to gallium thinking results similar to those found with silicides could follow. A new binary phase, β-SiB₃, ¹⁰ and series of quaternary phases, RE_{1.8}C₂Si₈(B₁₂)₃ (RE= Y, Tb, Er), ¹¹ showed the thinking to be correct and provided a basis for a closer examination into the use of a gallium flux for the synthesis of multinary borides.

Gallium has several characteristics that make it an interesting flux metal. As in aluminum, there is a very large difference between the melting (29 °C) and boiling points (2400 °C) of gallium, so there is seemingly a large range for reaction temperatures. However, boron has a very low solubility in gallium below about 1000°C. Thus, potential components in multinary borides can form stable non-boride phases that crash

out of the reaction mixture before boron has even had a chance to react. By working at 1000 °C and above we looked to determine the applicability of the gallium flux in the synthesis of a wider range of borides.

If successful, this synthesis technique could prove its usefulness by providing larger, better-formed crystals than those previously made, allowing for better property analyses. In addition, the unique chemistry of boron, which is responsible for the great diversity of known borides, could be extended to previously unknown phases.

C. Structural Features in Borides

Borides are a large and diverse class of compounds. This diversity is readily seen in the geometric arrangement of the boron atoms in borides, shown in Figure 1-1, which varies based on the ratio of boron to metal atoms found in the compound.^{24, 25} In metalrich borides, in which the boron-to-metal ratio (B:M) is less than 0.5, the boron atoms are isolated from each other, as shown in Figure 1-1a, and only metal-metal or metal-boron bonds are formed. When more boron is incorporated into the structure, increasing B:M to approximately 0.67, boron-boron bonds begin to form, resulting in isolated boron pairs, as shown in Figure 1-1b. A further increase in B:M to 1.0 allows the isolated boron pairs to link together and form the zigzag boron atom chain shown in Figure 1-1c. These chains will link together as more boron is added, resulting in double chains (Figure 1-1d) for B:M near 1.3, and triple chains (Figure 1-1e) for B:M around 1.5. Two-dimensional networks are formed when B:M increases to between 2.0 and 2.5. These networks most commonly comprise six-membered rings of boron atoms, as shown in Figure 1-1f,

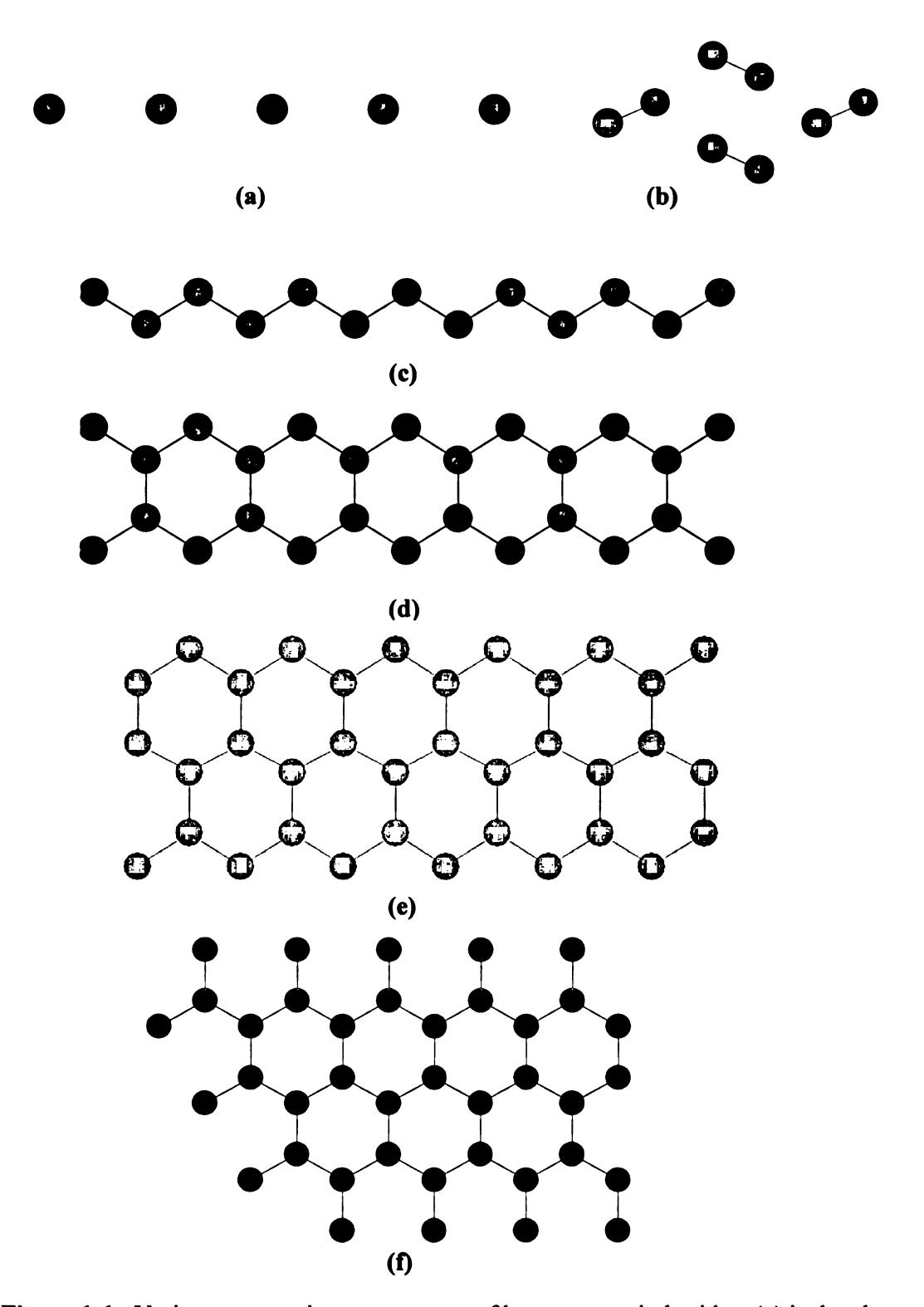


Figure 1-1. Various geometric arrangements of boron atoms in borides: (a) isolated atoms (B:M < 0.5), (b) isolated pairs (B:M \approx 0.67), (c) zigzag chain (B:M =1), (d) double chain (B:M \approx 1.3), (e) triple chain (B:M = 1.5), (f) two-dimensional network (2.0 \leq B:M \leq 2.5).

however, rings with five and seven boron atoms are also well known.²⁶⁻²⁸ Boron-rich compounds, with B:M values greater than 2.5, contain three-dimensional networks of boron atoms. The most common polyhedra formed by the boron atoms are octahedra, icosahedra, and cubo-octahedra.

The rich structural variety of borides is even more impressive when compared to that found in carbides and nitrides. Both carbides and nitrides have limited structural variety due in part to geometric factors. One such geometric factor is based on Hägg's rule, which states that interstitial compounds with a ratio of nonmetal to metal radii less than 0.59 will adopt a simple structure, such as body-centered cubic, face-centered cubic, hexagonal close-packed, or hexagonal. Because carbon and nitrogen atoms have rather small radii compared to most metals, they can occupy the octahedral holes between metal atoms, creating simple structures, as predicted by Hägg. Boron atoms tend to be larger, exceeding Hägg's 0.59-ratio rule, and prefer a trigonal prismatic coordination environment. The trigonal prismatic coordination environment and larger atom sizes bring boron atoms within bonding distance to each other, leading to the pairs, chains, etc. that are present throughout boride structural chemistry.

D. Chemical and Physical Properties of Borides

Accompanying the structural diversity in borides is an equally wide diversity of chemical and physical properties. Many borides have a great deal of chemical stability. Nowhere is this stability more evident than when borides are separated from a molten metal flux. To remove products from a copper flux, for instance, the ingot containing the now-solid flux and products is placed into an etching solution, a bath of nitric acid.

Regardless of concentration, the acid has little effect on the boride crystals, but completely removes the copper. Similar results are seen in aluminum flux reactions, where the etching solution can be either hydrochloric acid or sodium hydroxide. Again, minimal damage is done to the boride crystals while completely removing the metal. In cases where the boride crystals must be dissolved, warm or boiling aqua regia is used because the dissolution is often too slow at room temperature, leaving the boride crystals intact and unharmed.¹⁰

The strong covalent bonding in borides leads to great thermal stability. This stability allows borides to be used in many high temperature applications, such as thermoelectric conversion materials. 30-32 Promising results have been found for boron-rich borides, and an entire thermoelectric device was recently made consisting entirely of boron-rich components. 33 The current results on boride thermoelectric components are not optimized yet, so future work in this area looks to maximize effectiveness of these devices in harsh environments where other systems fail.

Borides have consistently found use in harsh industrial applications because they are hard and incompressible materials. The hardness of the compounds comes from the directional covalent bonds in borides, while the incompressibility is due to electrostatic repulsion between atoms and can be correlated with the valence electron density of the compounds.³⁴ The advantage of borides over more traditional industrial products is made apparent in their application in the cutting of iron-based metals. Boride coated tools are used instead of diamonds, which have superior hardness, but also react chemically with the iron in the metal.³⁵ The added chemical and thermal stability of borides give them potential for many industrial applications.

Superconductivity is not exactly a rare property for a boride to exhibit. However, when the critical transition temperature (T_c) associated with that superconductivity is 39 K, as in magnesium diboride, ³⁶ it is something of which to take note. Magnesium diboride had been prepared and its structure known for nearly fifty years before it was tested for superconductivity. The T_c of 39 K is the highest known for a bulk sample outside of the copper oxides, and led to a flurry of research in borides in recent years. Our group is included in that flurry and we hope that the molten metal flux technique can help isolate a boride with an even high T_c.

References

- 1. Prokhorov, A. M.; Lyakishev, N. P.; Burkhanov, G. S.; Dement'ev, V. A., High Purity Transition-Metal Borides: Promising Materials for Present Day Technology. *Inorganic Materials* **1996**, 32, (11), 1195-1201.
- 2. Kanatzidis, M. G.; Pöttgen, R.; Jeitschko, W., The Metal Flux- A Preparative Tool for Intermetallic Compounds. *Angewandte Chemie International Edition* **2005**, 44, (43), 6996-7023.
- 3. Fisk, Z.; Remeika, J. P., Growth of Single Crystals from Molten Metal Fluxes. In *Handbook on the Physics and Chemistry of the Rare Earths*; K.A. Gschneidner, J.; Eyring, L.,Eds. Elsevier Science: 1989; Vol. 12, pp 53-70.
- 4. Latturner, S.; Kanatzidis, M. G., Formation of Multinary Intermetallics from Reduction of Perovskites by Aluminum Flux--M₃Au_{6+x}Al₂₆Ti (M = Ca, Sr, Yb), a Stuffed Variant of the BaHg₁₁ Type. *Inorganic Chemistry* **2004**, 43, 2-4.
- 5. Latturner, S. E.; Bilc, D.; Ireland, J. R.; Kannewurf, C. R.; S.D.Mahanti; Kanatzidis, M. G., REAu₃Al₇ (RE = rare earth): New Ternary Alumindes Grown from Aluminum Flux. *Journal of Solid State Chemistry* **2003**, 170, (1), 48-57.
- 6. Latturner, S.; Kanatzidis, M. G., REAu₄Al₈Si: The End Member of a New Homologous Series of Intermetallics Featuring Thick AuAl2 layers. *Chemical Communications* **2003**, (18), 2340-2341.
- 7. Salvador, J. R.; Malliakas, C.; Gour, J. R.; Kanatzidis, M. G., RE₅Co₄Si₁₄ (RE= Ho, Er, Tm, Yb): Silicides Grown from Ga Flux Showing Exceptional Resistance to Chemical and Thermal Attack. *Chemistry of Materials* **2005**, 17, 1636-1645.
- 8. Wu, X.; Bilc, D.; Mahanti, S. D.; Kanatzidis, M. G., V₂Al₅Ge₅: First Ternary Intermetallic in the V-Al-Ge System Accessible in Liquid Aluminum. *Chemical Communications* **2004**, 1506-1507.
- 9. Wu, X.; Kanatzidis, M. G., REAuAl₄Ge₂ and REAuAl₄(Au_xGe_{1-x})₂ (RE= rare earth element): Quaternary Intermetallics Grown in Liquid Aluminum. *Journal of Solid State Chemistry* **2005**, 178, 3233-3242.
- 10. Salvador, J. R.; Bilc, D.; S.D.Mahanti; Kanatzidis, M. G., Stabilization of β-SiB₃ from Liquid Ga: A Boron-Rich Binary Semiconductor Resistant to High-Temperature Air Oxidation. *Angewandte Chemie International Edition* **2003**, 42, 1929-1932.
- 11. Salvador, J. R.; Bilc, D.; S.D.Mahanti; Kanatzidis, M. G., Gallium Flux Synthesis of Tb_{3-x}C₂Si₈(B₁₂)₃: A Novel Quaternary Boron-Rich Phase Containing B₁₂ Icosahedra. *Angewandte Chemie International Edition* **2002**, 41, (5), 844-846.

- 12. Bernard, A. U.S. Patent 3096149, 1963.
- 13. Okada, S.; Tanaka, T.; Leithe-Jasper, A.; Michiue, Y.; Gurin, V. N., Crystal Growth and Structure Analysis of a New Scandium Aluminum Boride Sc₂AlB₆. *Journal of Solid State Chemistry* **2000**, 154, 49-53.
- 14. Okada, S.; Atoda, T.; Higashi, I., Structural Investigation of Cr₂B₃, Cr₃B₄, and CrB by Single-Crystal Diffractometry. *Journal of Solid State Chemistry* **1987**, 68, 61-67.
- 15. Okada, S.; Atoda, T.; Higashi, I.; Takahashi, Y., Preparation of Single Crystals of MoB₂ by the Aluminum-flux Technique and Some of Their Properties. *Journal of Materials Science* **1987**, 22, 2993-2999.
- 16. Okada, S.; Hamano, K.; Higashi, I.; Lundström, T.; Tergenius, L.-E., Preparation of Single Crystals of a New Compound, Ta₅B₆ by the Aluminum Flux Method. *Bulletin of the Chemical Society of Japan* **1990**, 63, 687-691.
- 17. Higashi, I.; Takahashi, Y.; Atoda, T., Crystal Growth of Borides and Carbides of Transition Metals from Molten Aluminum Solutions. *Journal of Crystal Growth* 1976, 33, 207-211.
- 18. Becher, H. J.; Krogmann, K.; Peisker, E., Über das ternäre Borid Mn₂AlB₂. Zeitschrift für anorganische und allgemeine Chemie **2004**, 344, (3-4), 140-147.
- 19. Okada, S.; Hamano, K.; Lundström, T.; Higashi, I. In Crystal Growth of the New Compound Nb₂B₃, and the Borides NbB, Nb₅B₆, Nb₃B₄, and NbB₂, Using the Copper-Flux Method, Boron-Rich Solids, Albuquerque, New Mexico, 1986; Emin, D.; Aselage, T.; Beckel, C. L.; Howard, I. A.; Wood, C., Eds. American Institute of Physics: Albuquerque, New Mexico, 1985; pp. 456-459.
- 20. Okada, S.; Kudou, K.; Lundström, T., Preparations and Some Properties of W₂B, δ-WB, and WB₂ Crystals from High-Temperature Metal Solutions. *Japanese Journal of Applied Physics* **1995**, 34, (1), 226-231.
- 21. Shishido, T.; Ye, J.; Sasaki, T.; Note, R.; Obara, K.; Takahashi, T.; Matsumoto, T.; Fukuda, T., Growth of Single Crystals in the Systems with R-Rh-B and R-Rh-B-C (R= Rare Earth Element) from Molten Copper Flux. *Journal of Solid State Chemistry* 1997, 133, 82-87.
- 22. Zhang, F. X.; Tanaka, T., Single Crystal Growth of Some Rare-Earth Boron-Rich Compounds in RE-B-C(N) and RE-B-Si Systems. *Journal of Crystal Growth* **2004**, 271, 159-164.
- 23. Ye, J.; Shishido, T.; Kimura, T.; Matsumoto, T.; Fukuda, T., End Member of the Rhodium-Based Quaternary Borocarbides, ErRh₂B₂C. *Acta Crystallographica* **1998**, C54, 1211-1214.

- 24. Etourneau, J.; Hagenmuller, P., Structure and Physical Features of the Rare-Earth Borides. *Philosphical Magazine B* **1985**, 52, (3), 589-610.
- 25. Lundström, T., Structure, Defects and Properties of Some Refractory Borides. *Pure and Applied Chemistry* **1985**, 57, (10), 1383-1390.
- 26. Rogl, P., New Ternary Borides with YCrB₄-type Structure. *Materials Research Bulletin* 1978, 13, 519-523.
- 27. Kuz'ma., Y. B., Crystal Structure of the compound YCrB₄ and its analogs. *Kristallografiya* **1970**, 15, 372-374.
- 28. Sobczak, R.; Rogl, P., Magnetic Behavior of New Ternary Metal Borides with YCrB₄-type Structure. *Journal of Solid State Chemistry* **1979**, 27, 343-348.
- 29. Chen, J. G., Carbide and Nitride Overlayers on Early Transition Metal Surfaces: Preparation, Characterization, and Reactivities. *Chemical Reviews* 1996, 96, 1447-1498.
- 30. Mori, T., High Temperature Thermoelectric properties of B₁₂ Icosahedral Cluster-containing Rare Earth Boride Crystals. *Journal of Applied Physics* **2005**, 97, 093703.
- 31. Nakayama, T.; Shimizu, J.; Kimura, K., Thermoelectric Properties of Metal-Doped β-Rhombohedral Boron. *Journal of Solid State Chemistry* **2000**, 154, 13-19.
- 32. Imai, Y.; Mukaida, M.; Ueda, M.; Watanabe, A., Screening of the Possible Boronbased n-type thermoelectric conversion materials on the basis of the calculated densities of states of metal borides and doped β -boron. *Intermetallics* **2001**, 9, 721-734.
- 33. Takeda, M.; Kurita, Y.; Yokoyama, K.; Miura, T. In Synthesis and High Temperature Thermoelectric Properties of Alkaline-Earth Metal Hexaborides MB₆ (M=Ca,Sr,Ba), 2003 MRS Fall Meeting, Boston, MA.
- 34. Cumberland, R. W.; Weinberger, M. B.; Gilman, J. J.; Clark, S. M.; Tolbert, S. H.; Kaner, R. B., Osmium Diboride, An Ultra-Incompressible, Hard Material. *Journal of the American Chemical Society* **2005**, 127, 7264-7265.
- 35. Gao, F.; Hou, L.; He, Y., Origin of Superhardness in Icosahedral B₁₂ Materials. *Journal of Physical Chemistry B* **2004**, 108, 13069-13073.
- 36. Nagamatsu, J.; Nakagawa, N.; Muranaka, T.; Zenitani, Y.; Akimitsu, J., Superconductivity at 39K in Magnesium Diboride. *Nature* **2001**, 410, 63-64.

CHAPTER TWO

The Metal Flux Synthesis of Group Six Borides

A. Introduction

The group 6 elements form a very interesting series of binary borides. Chromium borides seem to vary in structure based on B:M ratio, as outlined earlier in this work. The boron atoms in these borides go from isolated atoms to isolated pairs, pairs to chains, chains to double chains, double chains to triple chains, triple chains to 2-D networks, and 2-D to 3-D networks with increasing B:M ratios. Molybdenum and tungsten borides follow most of the structural patterns according to B:M ratios. However, no molybdenum or tungsten borides with B:M ratios of 1.5 or 1.67 have been isolated. Interestingly, there are more borides with B:M \geq 2.0 for molybdenum and tungsten than there are for chromium.

Slight variations in the B:M ratios above 2.0 lead to various 2-D and 3-D boron networks for the molybdenum and tungsten borides. MoB_{2-x}, Mo_{2-x}, Mo_{2-x}, Mo_{1-x}B₃, WB₂, and W₂B₅ all have layers with planar hexagonal boron rings. Mo₂B₅ and W₂B₅ also have layers with puckered hexagonal boron rings. The structures of MoB_{2-x}, WB₂, MoB₄, and WB₄ all have a common feature: planar layers of boron hexagons. However, in the tetraborides, these layers are linked to form a 3-D network. Pairs of boron atoms replace one-third of the molybdenum or tungsten atoms in the metal atom layers of the diboride structures, linking the boron atoms of the tetraboride structure into a 3-D network.

Further interest into group 6 borides came from previous results with the molten metal flux technique. A Japanese group of researchers has used aluminum as the flux metal for the synthesis of borides. Initially, W₂B₅ was the only binary boride to grow from the flux reactions. Ternary phases incorporating aluminum were found in both the chromium and molybdenum systems, but no binary group 6 borides were found. Over a decade later, the same group reported that they could grow binary crystals in both the chromium-boron and molybdenum-boron systems by introducing a slow-cooling step into the heating profile following the soak at maximum temperature. Nearly twenty years after the initial research into the tungsten-boron system, two other W-B binaries, W₂B and WB, were grown in molten aluminum. Also in the new article was the report of copper flux synthesis of W₂B and WB in single-crystalline form.

Armed with the knowledge that both aluminum and copper had worked as fluxes for group 6 boride syntheses, we wanted to see if we could extend the technique to include gallium as a flux metal. Extending the use of a copper flux to chromium and molybdenum borides was also of interest because of its success in forming tungsten borides. No ternary group 6 borides synthesized from a molten metal flux have been reported (excluding the aluminum-containing borides). Thus, the chance to apply the flux technique to synthesize ternary compounds was also an exciting possibility.

Our initial gallium flux reactions targeted multinary group 6 borides, such as YbCr(Si,B)₄, YMo₃B₂, and NiW₂B₁₅. Despite many attempts targeting various ternary and quaternary borides, the only borides formed where binary phases. Copper flux reactions had similar results. While not giving up on our goal of synthesizing ternary borides from a metal flux, we did shift focus slightly, and started targeting binary borides

that had formed out of the multinary systems. In this chapter we describe the synthesis and structural characterization of binary borides synthesized using gallium and/or copper fluxes.

B. Experimental

Reagents:

All reagents were used as received without further purification: (i) Boron metal, 99% purity, -325 mesh, Cerac Specialty Inorganics, Milwaukee, WI, (ii) Chromium metal, 99.95% purity, -200 mesh, Cerac Specialty Inorganics, Milwaukee, WI, (iii) Molybdenum metal, 99.9% purity, Cerac Specialty Inorganics, Milwaukee, WI, (iv) Tungsten metal, 99.9% purity, Cerac Specialty Inorganics, Milwaukee, WI, (v) Gallium 3-5 mm shot, 99.99% purity, Plasmaterials, Livermore, CA, (vi) Copper metal cuttings, Mallinckrodt Specialty Chemicals Co., Paris, KY, (vii) Dysprosium metal (filed from ingot) 99.9% purity, Chinese Rare Earth Information Center, Inner Mongolia, China, (viii) Yttrium metal, 99.9% purity, -40 mesh, Cerac Specialty Inorganics, Milwaukee, WI, (ix) Nickel metal powder, 98-99% purity, -325 mesh, E.H. Sargent & Company.

Furnaces:

Commercial tube furnaces from Applied Test Systems, Inc. were used to heat reactions sealed in quartz tubes. Furnace controllers from the Omega Company were used to program heating profiles for individual reactions. Furnace temperatures were monitored during reactions by thermocouples connected to the Omega controllers. To extend the life of the furnaces, the operating temperature for prolonged heating was limited to 1000 °C.

A commercial, high-temperature, vertical tube furnace, with controller, from the Mellen Company was used for copper flux reactions. Heating profiles for individual reactions were programmed into the furnace controller. Thermocouples connected to the furnace controller were used to monitor furnace temperatures during reactions. To extend the life of the furnace, the operating temperature for prolonged heating was limited to 1350 °C.

A Lindberg Blue high-temperature, horizontal tube furnace was used for gallium and copper flux reactions. Heating profiles for individual reactions were programmed into the accompanying Lindberg UP150 furnace controller. Thermocouples connected to the furnace controller were used to monitor furnace temperatures during reactions. The maximum operating temperature for the furnace was 1500 °C.

A radio frequency (RF) furnace was constructed from an Ameritherm XP7.5CE Induction Heater and fused quartz reaction chamber. A molybdenum cylinder, machined to act as a reaction crucible holder, was used as a susceptor. A boron nitride cylinder was machined to hold the molybdenum crucible in the center of the reaction chamber. Details on the RF furnace setup are given in the appendix of this work.

RF furnace temperatures were controlled manually using the Ameritherm control unit. Reaction temperatures were monitored using an Ircon SA Series Infrared

Thermometer. During the course of some reactions, films deposited inside the reaction chamber would prevent the IR thermometer from accurately reporting furnace temperatures. In such circumstances, reaction temperatures were approximated based on power settings for the Ameritherm control unit and a series of calibration runs conducted

by heating only the molybdenum cylinder. Temperatures greater than 1700 °C were easily reached with this furnace.

Synthesis and Isolation:

Cr₅B₃: Boron (2 mmol) and chromium (2 mmol) powders were mixed and added to an alumina crucible, along with dysprosium filings (1 mmol). Pieces of copper totaling 2.54 g (40 mmol) were then placed in the crucible. After the addition of a loose-fitting alumina lid, the crucible was placed in the RF furnace. The RF furnace was evacuated under vacuum to a pressure near 10⁻³ Torr and flushed with nitrogen. Heating was initiated with the system under vacuum. The temperature was raised to 1400 °C in approximately 25 minutes and then held at that temperature for 2 hours, at which time the power to the furnace was shut off and the furnace was allowed to cool to room temperature.

After cooling, the crucible was removed from the furnace and placed into a bath of half-concentrated HNO₃. The etching solution entered the crucible through the loose-fitting lid. An overnight soak was used to completely remove the copper flux, however, many product crystals were removed from the flux after a 3- to 4-hour soak. Extended soaking in the bath was not found to damage the crystals. Silver, plate-like crystals were isolated in an estimated 20-30% percent yield based on chromium. Elemental analysis performed by EDS showed that chromium and boron were the only elements present in the plate-like crystals. The remainder of the collected product comprised elemental chromium and traces of DyB₆.

Cr₃B₄: Boron (4 mmol) and chromium (1 mmol) powders were mixed and added to an alumina crucible. Pieces of copper totaling 2.0 g were then placed in the crucible.

The crucible was suspended in a high-temperature tube furnace and heated under a slow flow of argon. The furnace was heated to 1300 °C in 13 hours and held at that temperature for 10 hours, at which point the power to the furnace was shut off and the furnace was allowed to cool to room temperature.

After cooling, the crucible was removed from the furnace and placed into a bath of half-concentrated HNO₃ in order to remove the copper flux. An overnight soak was used to completely remove the copper flux, however, many crystals were removed from the flux after a 3- to 4-hour soak. Extended soaking in the bath was not found to damage the crystals. Silver, plate-like crystals were isolated in approximately 20 to 40% yields based on chromium. The remainder of the collected product comprised Cr₂B₃, CrB₂, and elemental chromium.

Cr₂B₃: Boron (2 mmol) and chromium (1 mmol) powders were mixed and added to an alumina crucible. Pieces of gallium shot totaling 1.6 g were then placed in the crucible. The alumina crucible was then placed in 13 mm diameter quartz tube, evacuated under vacuum to a pressure near 10⁻⁴ Torr, and then sealed using an oxygen-acetylene torch. The quartz tube was then heated in a commercial tube furnace under a heating profile that increased the furnace temperature to 1000 °C in 10 hours, held the temperature constant for 96 hours, and then allowed the furnace to cool to room temperature.

After cooling, the quartz tube was opened and the alumina crucible was placed in a half-concentrated HCl bath in order to remove the excess gallium. Most of the gallium was removed after an overnight soak, but longer soaks can be used without damage to the recovered product. Silver needle-shaped crystals were isolated in approximately 40 to

60% yields based on chromium. The remainder of the product comprised CrB₂ and elemental chromium.

CrB₂: Boron (10 mmol) and chromium (1 mmol) powders were mixed and added to a glassy carbon crucible, along with yttrium (1 mmol). Pieces of gallium shot totaling 2.0 g were then placed in the crucible. The crucible was placed in the RF furnace, evacuated under vacuum to a pressure near 10⁻³ Torr, and flushed with argon. Heating was initiated under vacuum and the temperature was raised to 1300 °C in ten minutes. After holding at that temperature for 45 minutes, the power to the furnace was shutoff, and the furnace was allowed to cool to room temperature.

After cooling, the crucible was removed from the furnace and placed into a bath of 3M I₂ in DMF in order to remove the gallium flux. An overnight soak was found to be insufficient for removing all of the gallium, so soaking was continued for an additional 3 days. Extended soaking in the bath was not found to damage the crystals. Silver, hexagonal plate-like crystals were isolated in an estimated 30 to 40% yield based on chromium. Elemental analysis performed by EDS showed that chromium and boron were the only elements present in these crystals.

MoB: Boron (3 mmol), molybdenum (1 mmol), and yttrium (0.3 mmol) were added to a graphite crucible. Pieces of gallium shot totaling 1.6 g were then added, along with a loose-fitting graphite cap, and the crucible was placed in the RF furnace. The RF furnace was evacuated under vacuum to a pressure near 10⁻³ Torr and flushed with argon. Heating was initiated with the system under vacuum. The temperature was raised to 1300 °C in approximately 15 minutes and then held at that temperature for 15 minutes, at

which time insufficient cooling water flow shut off the power to the furnace. The furnace then cooled to room temperature.

After cooling, the crucible was placed in a bath of 3 M I₂ in DMF in order to remove the remaining gallium flux. An overnight soak was found to be insufficient for removing all of the gallium, so soaking continued for an additional 2 days. Extended soaking in the bath was not found to damage the crystals. Silver, plate-like crystals were a minor product (estimated 10 to 20% yield based on molybdenum). Purple powder and crystals of YB₆ were present in 20-30% yields based on yttrium. The remainder of the product collected comprised unreacted boron powder and traces of YB₆.

WB: Boron (7.5 mmol), nickel (0.5 mmol), and tungsten (1 mmol) powders were mixed and added to an alumina crucible along with pieces of gallium shot totaling 1.45 g. A quartz filter was placed in the crucible which was then placed in 13mm diameter quartz tube, evacuated under vacuum to a pressure near 10⁻⁴ Torr, and sealed using an oxygenacetylene torch. The tube was then heated in a commercial tube furnace under a heating profile that increased the furnace temperature to 1000 °C in 10 hours, held the temperature constant for 48 hours, allowed the furnace to cool to 850 °C in 5 hours, held the temperature constant for an additional 48 hours, and then allowed the furnace to cool to 250 °C in 60 hours.

The quartz tube was removed from the furnace at 250 °C and centrifuged to remove excess gallium. After centrifugation, the tube was opened and the crucible was placed in a bath of 5 M I₂ in DMF in order to remove the remaining gallium flux. An overnight soak was found to be insufficient for removing all of the gallium, so soaking continued for an additional 2 days. Extended soaking in the bath was not found to

damage the crystals. Silver, prismatic crystals were a minor product (estimated 10-20% yield based on tungsten). Hexagonal plates of Ni₂Ga₃ were the major product, while rectangular prismatic crystals of NiGa₄ were also a minor product (10-20% yield based on nickel). The remainder of the product collected was unreacted boron powder and traces of a tungsten-gallium phase.

C. Physical Measurements

Energy Dispersive Spectroscopy: Energy dispersive spectroscopy (EDS) analyses were carried out on selected crystals to determine their chemical composition. The analyses were performed with a JEOL JSM-6400 scanning electron microscope (SEM) equipped with Noran Vantage Energy Dispersive Spectroscopy (Si:Li) detector and Norvar window for standardless quantization of elements with $Z \ge 4$. The crystals were affixed to an alumina sample holder with double-sided carbon tape. The EDS data were acquired at an accelerating voltage of 10kV with a 30 to 60 second accumulation time.

Single-Crystal X-ray Crystallography: Single crystals were mounted on a glass fiber with super glue and their intensity data were collected on either a Bruker SMART platform CCD diffractometer, or a STOE IPDS II diffractometer using Mo Kα radiation at 50 kV and 40 mA.

Individual frames of Cr_3B_4 and WB examined with the Bruker machine were collected with a 0.3° ω rotation. The SMART software was used for data collection, and SAINT¹⁰ software was used for data extraction and reduction. After applying analytical

absorption corrections, structure solution and refinement were completed using direct methods and the SHELXTL¹¹ suite of programs.

Samples examined with the STOE (Cr₅B₃, Cr₂B₃, CrB₂, and MoB) had individual frames collected on a 34 cm image plate with a 60 second exposure time and a 1.0° ω rotation. The X-SHAPE¹² and X-RED-32¹³ software packages were used for data extraction and reduction and to apply an analytical absorption correction. Direct methods and the SHELXTL suite were used to solve and refine the structures.

The crystal structure refinement data for Cr₅B₃ are listed in Table 2-1. Atomic parameters found in the previous structure report¹⁴ were used as a starting point for structural refinement. The atomic positions and isotropic displacement parameters are listed in Table 2-2. Anisotropic displacement parameters for the chromium and boron atoms are found in Table 2-3. The bond distances, listed in Table 2-4, match well with those calculated from previous reports.

The crystal structure refinement data for Cr₃B₄ are listed in Table 2-5. Atomic parameters found in previous structure reports^{7, 15} were used as a starting point for structural refinement. The atomic positions and isotropic displacement parameters are listed in Table 2-6. Anisotropic displacement parameters for the chromium and boron atoms are found in Table 2-7. The bond distances, listed in Table 2-8, match well with those found in previous reports.

The crystal structure refinement data for Cr₂B₃ are listed in Table 2-9. The atomic positions and isotropic displacement parameters are listed in Table 2-10. Anisotropic displacement parameters for the chromium and boron atoms are found in Table 2-11.

The bond distances, listed in Table 2-12, match well with those calculated from the previous report on the structure.⁷

The crystal structure refinement data for CrB₂ are listed in Table 2-13. The atomic positions and isotropic displacement parameters are listed in Table 2-14. Anisotropic displacement parameters for the chromium and boron atoms are found in Table 2-15. The bond distances are listed in Table 2-16.

The crystal structure refinement data for MoB and WB are listed in Table 2-17.

Atomic parameters found for MoB were used as a starting point for structural refinement of WB. The atomic positions and isotropic displacement parameters for both compounds are listed in Table 2-18. Anisotropic displacement parameters for the all of the atoms are found in Table 2-19. The structure of WB needs further refinement to pinpoint the location of the boron atom. The anisotropic displacement parameters for this atom are quite large and would be reduced with a more accurate atom location. Additional work with absorption correction for the crystal can also help reduce the anisotropic values. The bond distances for MoB and WB, listed in Table 2-20 and Table 2-21, respectively, match well with those calculated from the previous report.²

Table 2-1. Crystal data and structure refinement for Cr₅B₃.

Formula weight 292.43

Temperature 293(2) K

Wavelength 0.71073 Å

Crystal system Tetragonal

Space group I4/mcm

Unit cell dimensions a = 5.4334(8) Å $\alpha = 90^{\circ}$

b = 5.4334(8) Å $\beta = 90^{\circ}$

c = 10.031(2) Å $\gamma = 90^{\circ}$

Volume 296.14(9) Å³

Z 4

Density (calculated) 6.559 g/cm³

Absorption coefficient 17.451 mm⁻¹

F(000) 540

Crystal size $0.098 \times 0.080 \times 0.035 \text{ mm}^3$

Theta range for data collection 4.06 to 36.70°

Index ranges $-9 \le h \le 9, -8 \le k \le 8, -16 \le l \le 16$

Reflections collected 2235

Independent reflections 220 [R(int) = 0.0994]

Completeness to theta = 36.70° 99.1 %

Refinement method Full-matrix least-squares on F²

Data / restraints / parameters 220 / 0 / 16

Goodness-of-fit on F² 1.098

Final R indices [I>2sigma(I)] R1 = 0.0618, wR2 = 0.1592 R indices (all data) R1 = 0.0698, wR2 = 0.1661

Extinction coefficient 0.026(7)

R1 =
$$\sum ||F_o| - |F_c|| / \sum |F_o|$$
 and wR2 = $[\sum (|F_o|^2 - F_c|^2)^2 / \sum (wF_o|^2)^2]^{1/2}$

Table 2-2. Atomic coordinates (x 10^4) and equivalent isotropic displacement parameters (Å²x 10^3) for Cr_5B_3 .

	х	У	Z	U(eq)
Cr(1)	3285(1)	1715(1)	1459(1)	7(1)
Cr(2)	0	0	0	7(1)
B(1)	0	0	2500	8(2)
B(2)	-1161(12)	-3839(12)	0	4(1)

U(eq) is defined as one third of the trace of the orthogonalized U^{ij} tensor.

Table 2-3. Anisotropic displacement parameters (Å²x 10³) for Cr₅B₃.

	Ω_{11}	U^{22}	U33	U ²³	U13	U12
Cr(1)	7(1)	7(1)	6(1)	0(1)	0(1)	0(1)
Cr(2)	6(1)	6(1)	7(1)	0	0	0
B(1)	8(3)	8(3)	7(4)	0	0	0
B(2)	5(2)	5(2)	3(3)	0	0	-3(3)

The anisotropic displacement factor exponent takes the form: $-2\pi^2$ [h^2 $a^{*2}U^{11}$ + ... + 2 h k a^* b^* U^{12}]

Table 2-4. Bond distances (Å) for Cr₅B₃.

Crl	B2	2x	2.1621(3)
Crl	B2	1x	2.1916(2)
Crl	B1	2x	2.2684(2)
Crl	CR1	lx	2.4127(4)
Crl	Cr2	2x	2.4892(3)
Cr2	B2	4x	2.1786(3)
Cr2	Crl	8x	2.4892(3)
B1	Crl	8x	2.2684(2)
B2	B2	1x	1.7865(2)
B2	Crl	4x	2.1621(3)
B2	Cr2	2x	2.1786(3)
B2	Crl	2x	2.1916(2)

Table 2-5. Crystal data and structure refinement for Cr₃B₄.

Formula weight 199.24

Temperature 293(2) K

Wavelength 0.71073 Å

Crystal system Orthorhombic

Space group Immm

Unit cell dimensions a = 2.9550(10) Å $\alpha = 90^{\circ}$

b = 2.9823(10) Å $\beta = 90^{\circ}$

c = 13.030(4) Å $\gamma = 90^{\circ}$

Volume 114.83(7) Å³

Z 2

Density (calculated) 5.762 g/cm³

Absorption coefficient 13.527 mm⁻¹

F(000) 184

Theta range for data collection 3.14 to 28.21°

Index ranges $-3 \le h \le 3, -3 \le k \le 3, -16 \le l \le 16$

Reflections collected 689

Independent reflections 102 [R(int) = 0.0176]

Completeness to theta = 29.05° 100.0 %

Refinement method Full-matrix least-squares on F²

Data / restraints / parameters 102 / 0 / 17

Goodness-of-fit on F² 1.072

Final R indices [I>2sigma(I)] R1 = 0.0145, wR2 = 0.0338 R indices (all data) R1 = 0.0183, wR2 = 0.0371

Extinction coefficient 0.0031(5)

R1 = $\sum ||F_o| - |F_c|| / \sum |F_o|$ and wR2 = $[\sum (|F_o|^2 - F_c|^2)^2 / \sum (wF_o|^2)^2]^{1/2}$

Table 2-6. Atomic coordinates ($x 10^4$) and equivalent isotropic displacement parameters ($\mathring{A}^2x 10^3$) for Cr_3B_4 .

	x	у	z	U(eq)
Cr(1)	0	0	0	2(1)
Cr(2)	-5000	0	-1862(1)	2(1)
B(1)	-5000	-5000	-668(3)	3(1)
B(2)	-5000	-5000	-1393(3)	4(1)

U(eq) is defined as one third of the trace of the orthogonalized U^{ij} tensor.

Table 2-7. Anisotropic displacement parameters (Å²x 10³) for Cr₃B₄.

	U ¹¹	U ²²	U33	U ²³	U13	U12
Cr(1)	2(1)	3(1)	1(1)	0	0	0
Cr(2)	1(1)	3(1)	2(1)	0	0	0
B(1)	0(2)	5(2)	4(2)	0	0	0
B(2)	5(2)	1(2)	5(2)	0	0	0

The anisotropic displacement factor exponent takes the form: $-2\pi^2$ [h^2 $a^{*2}U^{11}$ + ... + 2 h k a^* b^* U^{12}]

Table 2-8. Bond distances (Å) for Cr₃B₄.

Crl	B2	8x	2.2699(3)
Crl	Bl	4x	2.3353(3)
Cr2	B2	2x	2.1410(3)
Cr2	B1	4x	2.1824(3)
Cr2	B1	1 x	2.2707(5)
B1	B2	2x	1.7381(3)
B1	Cr2	4x	2.1824(3)
B1	Cr2	1 x	2.2707(5)
B1	Crl	2x	2.3353(3)
B2	B1	2x	1.7381(3)
B2	B2	1 x	1.7561(4)
B2	Cr2	2x	2.1410(3)
B2	Crl	4x	2.2699(3)

Table 2-9. Crystal data and structure refinement for Cr₂B₃.

Formula weight 136.43

Temperature 293(2) K

Wavelength 0.71073 Å

Crystal system Orthorhombic

Space group Cmcm

Unit cell dimensions a = 3.0059(6) Å $\alpha = 90^{\circ}$

b = 18.084(4) Å $\beta = 90^{\circ}$

c = 2.9436(6) Å $\gamma = 90^{\circ}$

Volume 160.01(6) Å³

Z 4

Density (calculated) 5.663 g/cm³
Absorption coefficient 12.949 mm⁻¹

F(000) 252

Theta range for data collection 2.25 to 29.13°

Index ranges $-4 \le h \le 4, -24 \le k \le 24, -4 \le l \le 3$

Reflections collected 737

Independent reflections 145 [R(int) = 0.0286]

Completeness to theta = 29.13° 98.6 %

Refinement method Full-matrix least-squares on F²

Data / restraints / parameters 145 / 0 / 22

Goodness-of-fit on F² 1.257

Final R indices [I>2sigma(I)] R1 = 0.0316, wR2 = 0.0503

R indices (all data) R1 = 0.0320, wR2 = 0.0503

Extinction coefficient 0.066(6)

R1 = $\sum ||F_o| - |F_c|| / \sum |F_o|$ and wR2 = $[\sum (|F_o|^2 - F_c|^2)^2 / \sum (wF_o|^2)^2]^{1/2}$

Table 2-10. Atomic coordinates (x 10^4) and equivalent isotropic displacement parameters (\mathring{A}^2x 10^3) for Cr_2B_3 .

	X	у	Z	U(eq)
Cr(1)	0	4276(1)	2500	2(1)
Cr(2)	0	7036(1)	2500	2(1)
B(1)	0	8280(5)	2500	5(2)
B(2)	0	1191(5)	2500	4(2)
B(3)	0	235(5)	2500	3(2)

U(eq) is defined as one third of the trace of the orthogonalized U^{ij} tensor.

Table 2-11. Anisotropic displacement parameters (\mathring{A}^2x 10³) for Cr_2B_3 .

	Π_{11}	U ²²	U33	U ²³	U13	U ¹²
Cr(1)	4(1)	1(1)	2(1)	0	0	0
Cr(2)	2(1)	1(1)	2(1)	0	0	0
B(2)	0(5)	4(4)	8(5)	0	0	0
B(3)	3(5)	2(4)	4(4)	0	0	0
B(1)	8(6)	6(4)	2(4)	0	0	0

The anisotropic displacement factor exponent takes the form: $-2\pi^2$ [h^2 $a^{*2}U^{11} + ...$

Table 2-12. Bond distances (Å) for Cr₂B₃.

Cr1	B2	4x	2.2654(3)
Crl	В3	4x	2.2817(3)
Crl	В3	2x	2.2936(3)
Crl	Bl	2x	2.3433(3)
Cr2	B2	2x	2.1462(3)
Cr2	Bl	4x	2.1808(3)
Cr2	B1	1 x	2.2548(4)
B1	B2	2x	1.7555(3)
B1	Cr2	4x	2.1808(3)
В1	Cr2	1 x	2.2548(4)
Bl	Crl	2x	2.3433(3)
B2	В3	1 x	1.7247(3)
B2	B1	2x	1.7555(3)
B2	Cr2	2x	2.1462(3)
B2	Crl	4x	2.2654(3)
В3	В3	2x	1.6990(3)
В3	B2	1 x	1.7247(3)
В3	Crl	4x	2.2817(3)
В3	Crl	2x	2.2936(3)

Table 2-13. Crystal data and structure refinement for CrB₂.

Formula weight 73.62

Temperature 100(2) K

Wavelength 0.71073 Å

Crystal system Hexagonal

Space group P6/mmm

Unit cell dimensions a = 2.9604(4) Å $\alpha = 90^{\circ}$

b = 2.9604(4) Å $\beta = 90^{\circ}$

c = 3.0574(6) Å $\gamma = 120^{\circ}$

Volume 23.205(6) Å³

Z 2

Density (calculated) 10.536 g/cm³

Absorption coefficient 22.350 mm⁻¹

F(000) 68

Theta range for data collection 6.66 to 29.02°

Index ranges $-4 \le h \le 4, -3 \le k \le 3, -4 \le l \le 4$

Reflections collected 219

Independent reflections 24 [R(int) = 0.0289]

Completeness to theta = 29.02° 100.0 %

Refinement method Full-matrix least-squares on F²

Data / restraints / parameters 24 / 0 / 6

Goodness-of-fit on F² 1.296

Final R indices [I>2sigma(I)] R1 = 0.0163, wR2 = 0.0402

R indices (all data) R1 = 0.0163, wR2 = 0.0402

Extinction coefficient 1.0(5)

 $R1 = \sum ||F_o| - |F_c|| / \sum |F_o| \text{ and } wR2 = \left[\sum (|F_o|^2 - F_c|^2)^2 / \sum (wF_o|^2)^2\right]^{1/2}$

Table 2-14. Atomic coordinates ($x 10^4$) and equivalent isotropic displacement parameters ($\mathring{A}^2x 10^3$) for CrB₂.

	х	у	z	U(eq)
Cr(1)	0	0	5000	1(1)
B(1)	-3333	3333	0	1(1)

U(eq) is defined as one third of the trace of the orthogonalized U^{ij} tensor.

Table 2-15. Anisotropic displacement parameters (Å²x 10³) for CrB₂.

	Ω_{11}	U22	U33	U23	Π13	U ¹²
 Cr(1)	1(1)	1(1)	0(1)	0	0	1(1)
B(1)	1(1)	1(1)	0(2)	0	0	0(1)

The anisotropic displacement factor exponent takes the form: $-2\pi^2$ [h^2 $a^{*2}U^{11} + ...$

 $+ 2 h k a* b* U^{12}$]

Table 2-16. Bond distances (Å) for CrB₂.

Crl	B1	12x	2.2943(3)
B1	B1	3x	1.7069(2)
B1	Crl	6x	2.2943(2)

Table 2-17. Crystal data and structure refinement for MoB and WB

Formula	МоВ	WB	
Formula weight	106.75	194.66	
Crystal system	Tetragonal	Tetragonal	
Space group	I4 ₁ /amd	I4 ₁ /amd	
Unit cell dimensions	a = 3.1103(4) Å	a = 3.1138(8) Å	
	b = 3.1103(4) Å	b = 3.1138(8) Å	
	c = 16.899(3) Å	c = 16.929(9) Å	
Volume	163.48(4) Å ³	164.14(10) Å ³	
Z, Density (calculated)	8, 8.674 g/cm ³	8, 15.755 g/cm ³	
Absorption coefficient	14.713 mm ⁻¹	139.427 mm ⁻¹	
F(000)	376	632	
Crystal size, mm	0.004 x 0.052 x 0.096	0.004 x 0.072 x 0.106	
Theta range for data collection	4.73 to 29.11°	4.71 to 28.30°	
Index ranges	$-4 \le h \le 3,$	$-3 \le h \le 3,$	
	$-4 \le k \le 3,$	$-3 \le k \le 3,$	
	$-21 \le l \le 21$	$-21 \le l \le 21$	
Reflections collected	679	524	
Independent reflections	76 [R(int) = 0.0454]	65 [R(int) = 0.0435]	
Completeness to θ_{max}	100.0 %	91.5%	
Refinement method	Full-matrix least-squares on F ²		
Data / restraints / parameters	76/0/9	65/0/10	
Goodness-of-fit on F ²	1.075	1.384	
Final R indices [I>2σ(I)]	R1 = 0.0206,	R1 = 0.0663,	
	wR2 = 0.0456	wR2 = 0.1680	
R indices (all data)	R1 = 0.0308,	R1 = 0.0669,	
	wR2 = 0.0469	wR2 = 0.1688	
Extinction coefficient	0.013(2)	0.015(5)	

R1 = $\sum ||F_o| - |F_c|| / \sum |F_o|$ and wR2 = $[\sum (|F_o^2 - F_c^2|)^2 / \sum (wF_o^2)^2]^{1/2}$

Table 2-18. Atomic coordinates ($x 10^4$) and equivalent isotropic displacement parameters ($\mathring{A}^2x 10^3$) for MoB and WB.

	x	у	Z	U(eq)
Mo(1)	0	2500	721(1)	3(1)
B(2)	-5000	2500	-309(6)	4(2)
W(1)	0	2500	724(1)	4(2)
B(1)	-5000	-2500	300(40)	40(30)

U(eq) is defined as one third of the trace of the orthogonalized U^{ij} tensor.

Table 2-19. Anisotropic displacement parameters ($Å^2x$ 10³) for MoB and WB.

	U11	U ²²	U ³³	U ²³	U13	U ₁₂
Mo(1)	2(1)	2(1)	6(1)	0	0	1(1)
B(1)	4(5)	3(5)	6(4)	0	0	0(1)
W(1)	6(2)	5(2)	0(2)	0	0	0
B(1)	0(40)	130(80)	0(30)	0	0	0

The anisotropic displacement factor exponent takes the form: $-2\pi^2$ [h^2 $a^{*2}U^{11}$ + ...

 $+ 2 h k a* b* U^{12}$]

Table 2-20. Bond distances (Å) for MoB.

Mol	B2	4x	2.3070(2)
Mol	B2	2x	2.3353(3)
Mol	B2	1x	2.4826(5)
B2	B2	2x	1.8739(2)
B2	Mol	4x	2.3070(2)
B2	Mol	2x	2.3353(3)
B2	Mol	1 x	2.4826(5)

Table 2-21. Bond distances (Å) for WB.

W1	B1	4x	2.3153(4)
W1	В1	2x	2.3307(7)
Wl	B1	1x	2.4979(13)
BI	Bl	2x	1.8604(4)
B1	Wl	4x	2.3153(4)
B1	WI	2x	2.3307(7)
B1	W1	1 x	2.4979(13)

D. Structural Description

Cr₅B₃: The structure of Cr₅B₃ (Figure 2-1a) was first reported by Bertaut and Blum,¹⁴ and came to be the representative of its own structure type. A common characteristic for the structure type is the formation of dumbbell-like pairs of atoms, shown in Figure 2-1b. An investigation of the coordination environments of the atoms reveals elongated octahedra of boron atoms around Cr1 and antiprisms of chromium atoms around B1. The trigonal prismatic coordination commonly found for boron atoms is seen in the chromium atoms around B2.

Cr₃B₄: The structure of Cr₃B₄ belongs to the Ta₃B₄-structure type and was first described by researchers in Sweden.¹⁵ The structure type is characterized by double chains of boron atoms that link together to form a series of side-sharing hexagons (Figure 2-2a). The structure can also be described, as in the work by Okada, *et al.*,⁷ by stacking sheets of AlB₂-type structure. A ½, ½, 0 unit cell translation of the AlB₂ structure builds the Cr₃B₄ structure. The sheets forming the structure are then interconnected through Cr-Cr bonds.

Cr₂B₃: A description of the Cr₂B₃ structure, which belongs to the V₂B₃-structure type, was given by Okada, *et al.*, in the first account on the structure of the compound.⁷ As with Cr₃B₄, the structure can be built by ½, ½, 0 unit cell translations of an AlB₂-type structure. In this compound, triple chains of boron atoms link together and form two columns of hexagons (Figure 2-2b). The previous structural description by Okada also points out that the interatomic distances between chromium atoms (2.62 Å) are larger than the distance in the elemental metal (2.498 Å), suggesting that Cr–B and B–B bonds hold the sheets in the structure together.

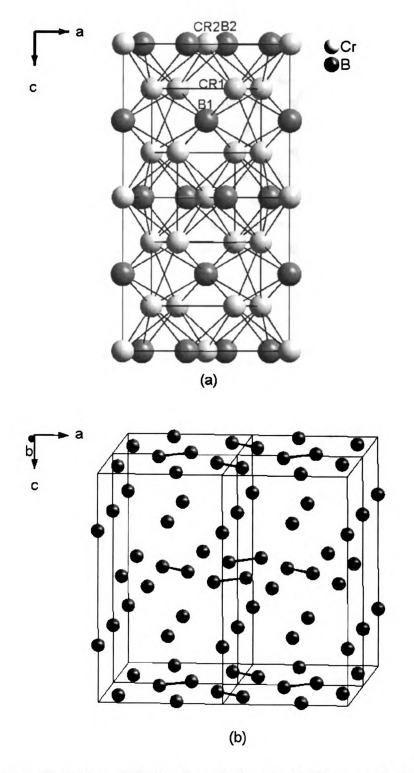
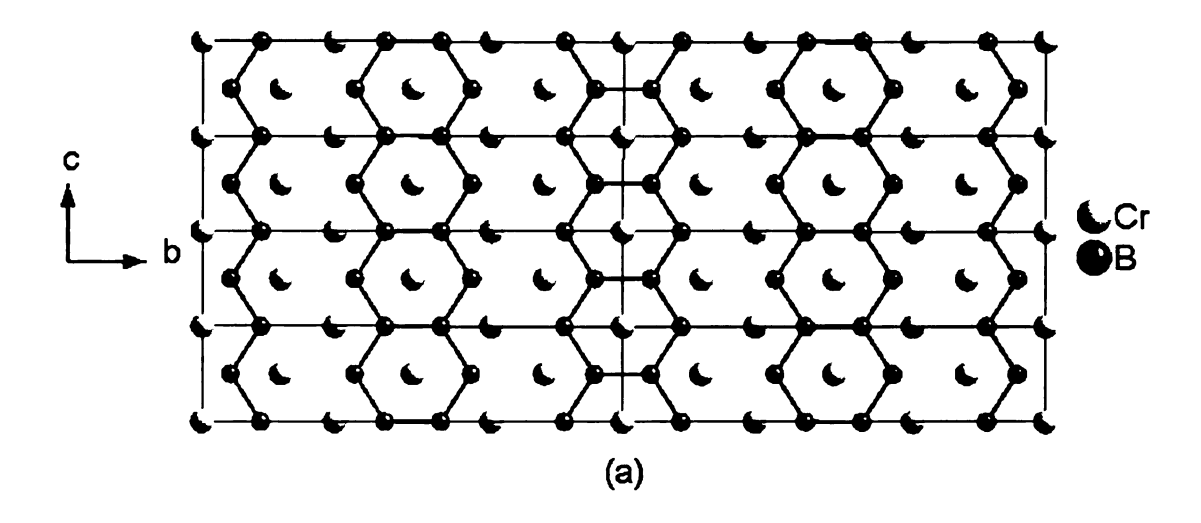


Figure 2-1 (a) Representation of Cr_5B_3 along the b-axis. (b) Boron pairs in Cr_5B_3 (Cr atoms omitted for clarity).



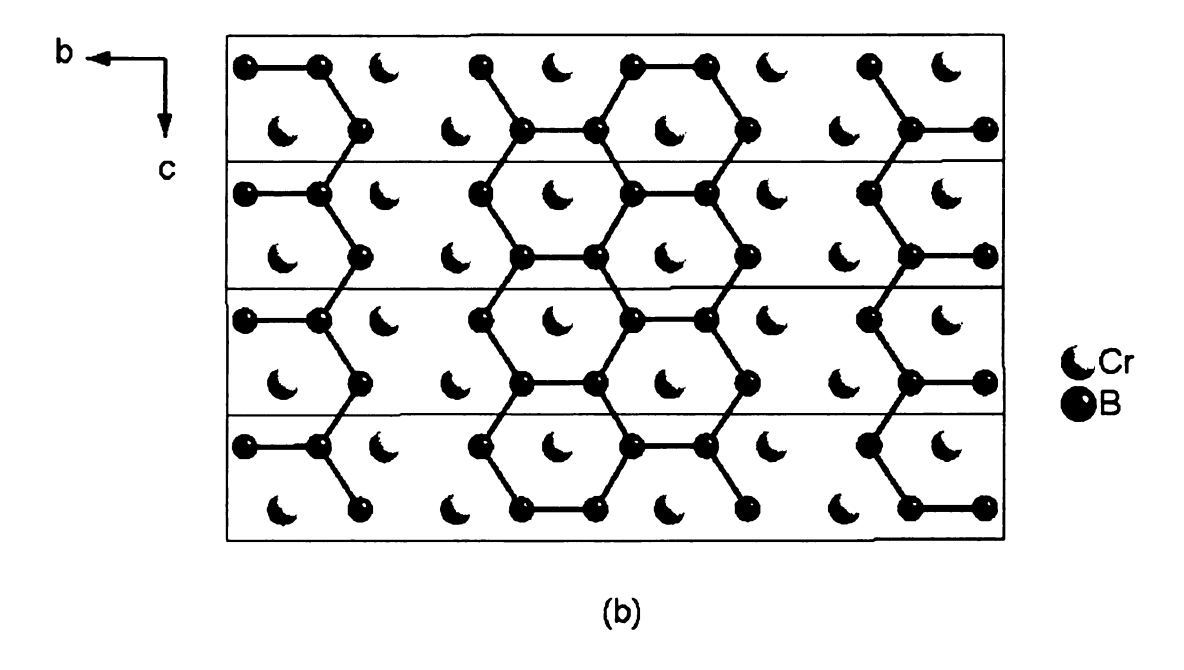


Figure 2-2. Double and triple chains of boron atoms in (a) Cr_3B_4 and (b) Cr_2B_3 , respectively.

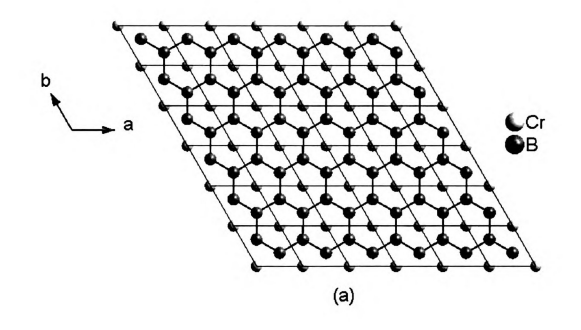
CrB₂: Like most transition metal diborides, CrB₂ crystallizes with the AlB₂-structure type. This structure-type comprises lamellar sheets of boron atoms in a graphite-like arrangement and hexagonally close-packed metal atoms. The structure of CrB₂ is shown in Figure 2-3a and the planar nature of the graphite-like boron layers are emphasized in Figure 2-3b.

MB (M=Mo, W): The monoborides of molybdenum and tungsten both crystallize in the MoB-structure type (Figure 2-4). The structure, first described by Kiessling,² features infinite zigzag chains of boron atoms running parallel to the a-axis in one sheet and parallel to the b-axis in the next. The metal atoms form trigonal prisms around the boron atoms.

E. Results and Discussion

As mentioned, the molten metal flux technique has been used to synthesize group 6 borides with copper and aluminum as the flux metals, so we were interested in extending the technique to include gallium. The synthesis and growth of Cr₂B₃, CrB₂, MoB, and WB from a gallium flux indicates initial success in our extension of the technique. These results are encouraging, but they have been limited to binary borides.

The chromium borides can be formed from systems containing just chromium, boron, and gallium, so the influence of varying the chromium to boron ratio on the resulting borides was briefly investigated. One of the most interesting things found was that CrB_2 was the only boride formed at the most boron-rich ratios. Though it was expected that CrB_4 would form at some point, that was not the case, even when the B:Cr



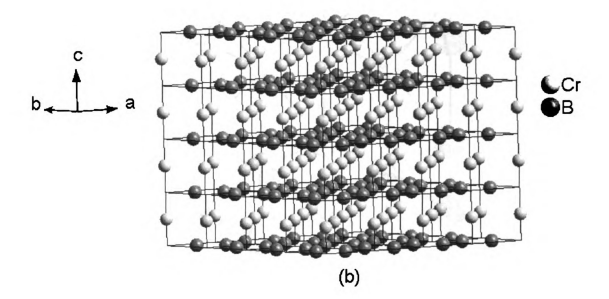


Figure 2-3. (a) CrB_2 structure seen along c-axis (b) Planar-nature of boron layers in CrB_2 .

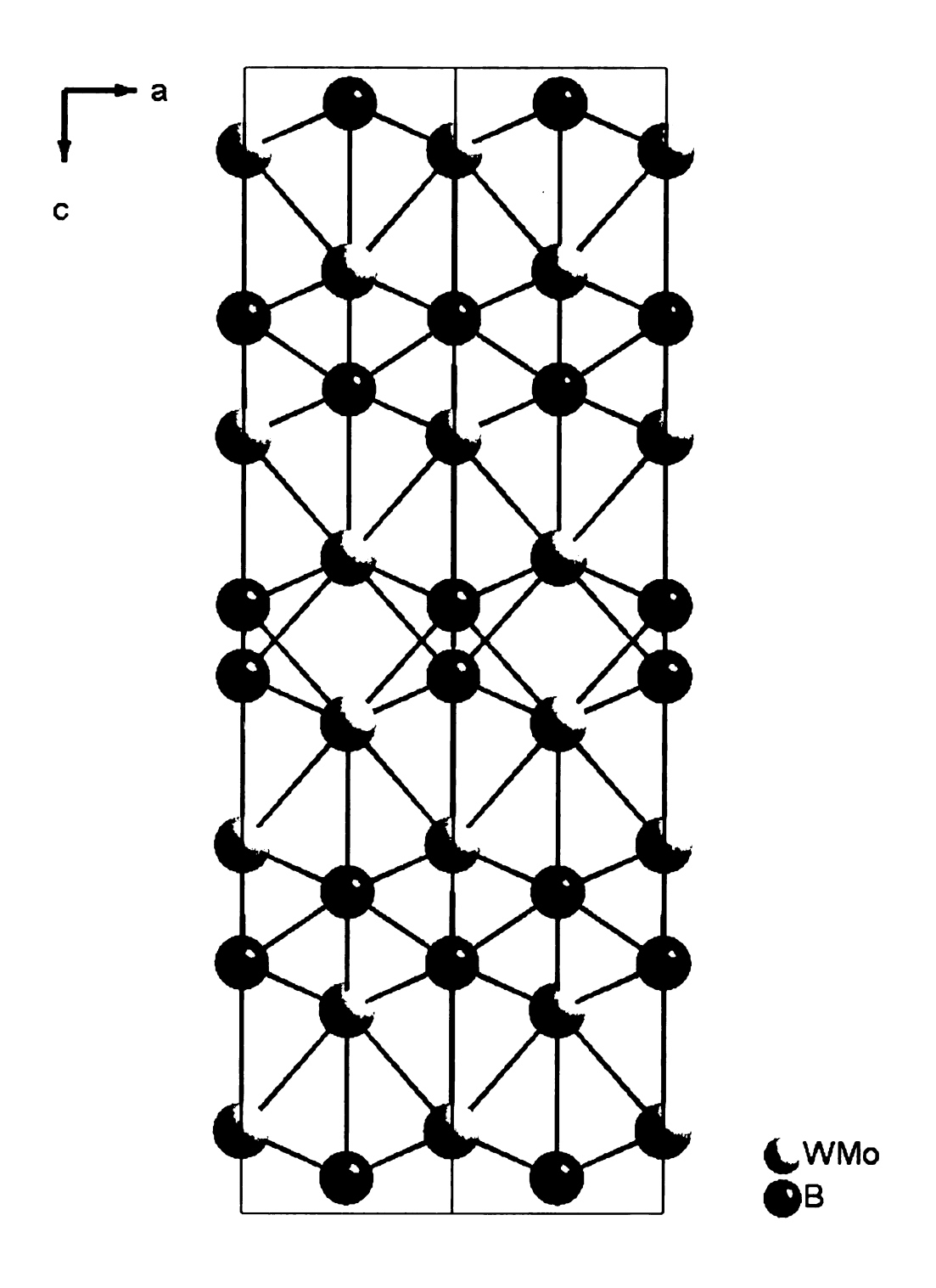


Figure 2-4. Structure of MB (M = Mo, W) viewed down the b-axis.

ratio reached 10:1. It was also slightly troubling that more borides with lower B:Cr ratios were not found. An expanded study looking at more B:Cr ratios should help determine which borides can be synthesized from the gallium flux. The results of the previous aluminum flux studies also imply that cooling rates for the reactions must also be studied.

Our limited attempts to synthesize ternary borides from a gallium flux were unsuccessful. However, monoborides of the heavier group 6 members from these reactions aimed at ternary species were synthesized. Subsequent attempts to isolate these borides from systems containing only the metal, boron, and gallium have not been successful. However, further investigations varying the B:M ratios and heating profiles are needed for a complete study. Varying the heating profiles and reagent ratios may also help in forming ternary group 6 borides when other metals are included in the reactions.

Crystals of Cr₅B₃, Cr₃B₄, and Cr₂B₃ have been successfully grown from reactions utilizing a molten copper flux. The latter two borides were grown from systems containing only chromium, boron, and copper, so there is potential that other borides will be found from similar reactions that vary the B:Cr ratio and heating profiles. While we were unable to isolate borides of the heavier group 6 elements or ternary borides with any group 6 members from copper flux reactions, further studies may be made more successful by varying the reagent stoichiometry and/or heating profiles.

F. Conclusions

The molten metal flux technique has successfully been applied to the synthesis of Group VI borides. Both gallium and copper have been used as the flux metal in the synthesis of Cr₂B₃. Molybdenum monoboride, tungsten monoboride, and chromium

diboride have been synthesized from gallium flux reactions. Cr_5B_3 and Cr_3B_4 have been synthesized from reactions utilizing molten copper. We have not synthesized any ternary Group VI borides from either gallium or copper, but our investigations into these systems are rather limited. We believe that further investigations into the flux reactions are merited and necessary based on these initial results.

References

- 1. Klesnar, H.; Aselage, T. L.; Morosin, B.; Kwei, G. H.; Lawson, A. C., The Diboride Compounds of Molybdenum: MoB_{2-x} and Mo₂B_{5-y}. *Journal of Alloys and Compounds* **1996**, 241, 180-186.
- 2. Kiessling, R., The Crystal Structure of Molybdenum and Tungsten Borides. *Acta Chemica Scandinavica* **1947**, 1, 893-916.
- 3. Lundström, T.; Rosenberg, I., The Crystal Structure of the Molybdenum Boride Mo_{1-x}B₃. Journal of Solid State Chemistry 1973, 6, 299-305.
- 4. Lundström, T., The Structure of Ru_2B_3 and $WB_{2.0}$, as determined by single-crystal diffractometry, and some notes on the W-B system. Arkiv för Kemi 1969, 30, 115-127.
- 5. Romans, P. A.; Krug, M. P., Composition and Crystallographic Data for the Highest Boride of Tungsten: *Acta Crystallographica* **1966**, 20, 313-315.
- 6. Higashi, I.; Takahashi, Y.; Atoda, T., Crystal Growth of Borides and Carbides of Transition Metals from Molten Aluminum Solutions. *Journal of Crystal Growth* **1976**, 33, 207-211.
- 7. Okada, S.; Atoda, T.; Higashi, I., Structural Investigation of Cr₂B₃, Cr₃B₄, and CrB by Single-Crystal Diffractometry. *Journal of Solid State Chemistry* **1987**, 68, 61-67.
- 8. Okada, S.; Atoda, T.; Higashi, I.; Takahashi, Y., Preparation of Single Crystals of MoB₂ by the Aluminum-flux Technique and Some of Their Properties. *Journal of Materials Science* **1987**, 22, 2993-2999.
- 9. Okada, S.; Kudou, K.; Lundström, T., Preparations and Some Properties of W_2B , δ -WB, and WB₂ Crystals from High-Temperature Metal Solutions. *Japanese Journal of Applied Physics* **1995**, 34, (1), 226-231.
- 10. Sheldrick, G. M. SAINT, Version 4; Siemens Analytical X-Ray Instruments, Inc.: Madison, WI.
- 11. Sheldrick, G. M. SHELXTL Structure Determination Program, Version 5.0; Siemens Analytical X-Ray Instruments, Inc.: Madison, WI, 1995.
- 12. X-SHAPE, Version 2.05; STOE & Cie GmbH: 2004.
- 13. X-RED 32, Version 1.10; STOE & Cie GmbH: 2004.
- 14. Bertaut, F.; Blum, P., Etude des borures de chrome. Comptes Rendus Hebdomadaires des Seances de l'Academie des Sciences 1953, 236, 1055-1056.

15. Elfstrom, M., The Crystal Structure of Cr₃B₄. Acta Chemica Scandinavica 1961, 15, (5), 1178.

CHAPTER THREE

The Metal Flux Synthesis of Group Seven Borides

A. Introduction

There are many similarities between the borides of chromium and the borides of manganese. Both metals have borides that display the interesting series of boron atom configurations from isolated boron atoms to a three-dimensional network found only in CrB₄ and MnB₄. Several reports have even mentioned a manganese monoboride that crystallizes with the CrB-type structure, instead of its normal FeB-type structure. However, several manganese analogs are "missing" when compared to the chromium system, such as Mn₅B₃ and Mn₂B₃. We became interested in whether it was possible to use the metal flux to isolate these "missing" borides.

The literature for flux syntheses of manganese borides returned only a ternary phase that incorporated aluminum from the flux, Mn₂AlB₂.⁴ This was a bit surprising, due to the success of the flux technique with the group 6 metals.⁵⁻⁸ During the literature search we also checked for reports on flux synthesis of rhenium borides. Again, we found no previous work done in the area, but the overall lack of work done in the Re-B system did not make this overly surprising.

The Re-B system has produced Re₃B, ReB₂, and Re₇B₃, and only Re₃B had structural characterization performed on a single crystal. Rather large single crystals of

ReB₂ were recently grown using the floating zone method, however, the growth temperature was near 2400°C, well above temperatures the equipment in our labs can attain consistently. The lower temperatures used in our flux reactions would be very attractive for producing crystals of any of these compounds.

Single crystals are useful when looking for anisotropic behavior of properties in a compound. The magnetism in Mn₃B₄ is a fine example of this anisotropy, as ferromagnetism is detected in the *ac*-plane and antiferromagnetism is found between layers along the b-axis. ^{12, 13} Discovering and studying similar phenomena in other compounds would be greatly simplified by using single crystals. The nature of the superconductivity in rhenium borides ^{14, 15} may also be better understood when single crystals are used in the physical measurements. The use of single crystals limits the possibility of minor phases negatively influencing results, while these minor phases may go undetected in powdered samples.

We report here our attempts to use the molten metal flux technique in the synthesis of group 7 borides. A molten gallium flux has been used to synthesize three binary borides, MnB, MnB₄, and ReB₂, and four ternary borides, HoMnB₄, DyReB₄, ErReB₄, and YbReB₄. Our attempts to use alternate flux metals in the syntheses of these compounds are also discussed.

B. Experimental Section

Reagents:

All reagents were used as received without further purification: (i) Boron metal, 99% purity, -325 mesh, Cerac Specialty Inorganics, Milwaukee, WI, (ii) Rhenium

powder, 99.99% purity, Strem Chemicals, Newburyport, MA, (iii) Gadolinium metal (filed from ingot) 99.9% purity, Chinese Rare Earth Information Center, Inner Mongolia, China, (iv) Dysprosium metal (filed from ingot) 99.9% purity, Chinese Rare Earth Information Center, Inner Mongolia, China, (v) Erbium metal (filed from ingot) 99.9% purity, Chinese Rare Earth Information Center, Inner Mongolia, China, (vi) Gallium 3-5 mm shot, 99.999% purity, Plasmaterials, Livermore, CA, (vii) Manganese powder, 99.9% purity, -50 mesh, Aldrich Chemical Company, Milwaukee, WI, (viii) Tantalum powder, 99.9% purity, Cerac Specialty Inorganics, Milwaukee, WI.

Furnaces:

A Lindberg Blue high-temperature, horizontal tube furnace was used with a continuous argon flow of approximately 0.1 L/min. Heating profiles for individual reactions were programmed into the accompanying Lindberg UP150 furnace controller. Thermocouples connected to the furnace controller were used to monitor furnace temperatures during reactions. The maximum operating temperature for the furnace was 1500 °C.

A radio frequency (RF) furnace was constructed from an Ameritherm XP7.5CE Induction Heater and fused quartz reaction chamber. A molybdenum cylinder, machined to act as a reaction crucible holder, was used as a susceptor. A boron nitride cylinder was machined to hold the molybdenum crucible in the center of the reaction chamber. Details on the RF furnace setup are given in the appendix of this work.

RF furnace temperatures were controlled manually using the Ameritherm control unit. Reaction temperatures were monitored using an Ircon SA Series Infrared

Thermometer. During the course of some reactions, films deposited inside the reaction

chamber would prevent the IR thermometer from accurately reporting furnace temperatures. In such circumstances, reaction temperatures were approximated based on power settings for the Ameritherm control unit and a series of calibration runs conducted by heating only the molybdenum cylinder. Temperatures greater than 1700 °C were easily reached with this furnace.

Synthesis and Isolation:

MnB: Boron (4 mmol), tantalum (1 mmol), and manganese (2 mmol) powders were mixed and added to an alumina crucible along with pieces of gallium shot totaling 1.67 g. A quartz filter was placed in the crucible which was then placed in 13 mm diameter quartz tube, evacuated under vacuum to a pressure near 10⁻⁴ Torr, and sealed using an oxygen-acetylene torch. The tube was then heated in a commercial tube furnace under a heating profile that increased the furnace temperature to 1000 °C in 10 hours, held the temperature constant for 48 hours, allowed the furnace to cool to 850 °C in 5 hours, held the temperature constant for an additional 48 hours, and then allowed the furnace to cool to 250 °C in 60 hours.

The quartz tube was removed from the furnace at 250 °C and centrifuged to remove excess gallium. After centrifugation, the tube was opened and the crucible was placed in a bath of 5M I₂ in DMF in order to remove the remaining gallium flux. An overnight soak was found to be insufficient for removing all of the gallium, so soaking continued for an additional 2 days. Extended soaking in the bath was not found to damage the crystals. Silver, prismatic crystals were produced in about 40% yields, based on manganese. Visual distinction between MnB and MnSi crystals is nearly impossible, so EDS analysis was used to differentiate crystals. Elemental analysis performed by EDS

using an SEM showed that manganese and boron were the only elements present in the crystal used for diffraction study. Besides the MnSi, the collected product also contained MnGa₄ and MnGa_{4.5}.

MnB₄: Boron and manganese powder were mixed and added to alumina crucibles in millimolar quantities in boron-to-manganese ratios between 2:1 and 5:1. Pieces of gallium shot totaling between 1.5 g and 2.5 g were then placed in the crucibles. The alumina crucibles were then placed in 13 mm diameter quartz tubes and evacuated under vacuum to a pressure near 10⁻⁴ Torr. The quartz tubes were then sealed using an oxygen-acetylene torch. The quartz tubes were placed in mullite tubes, then heated in commercial tube furnaces under heating profiles that increased the furnace temperature to 1000 °C in 10 hours, held the temperature constant for 48 hours, allowed the furnace to cool to 850 °C in 5 hours, held the temperature constant for an additional 48 hours, and then allowed the furnace to cool to room temperature in 60 hours.

After cooling, the quartz tubes were opened and the alumina crucibles were placed in a half-concentrated HCl bath in order to remove the excess gallium. Most of the gallium was removed after an overnight soak, but longer soaks were used without damage to the recovered product. Silver, plate-like crystals with ridges (later found to be twinned crystals) were produced in 30-40% yields. Elemental analysis performed by EDS using an SEM showed that manganese and boron were the only elements present in the crystals. The remainder of the product comprised MnGa₄ and MnGa_{4.5}.

ReB₂: Boron and rhenium powder were mixed and added to alumina crucibles in millimolar quantities in boron-to-rhenium ratios between 2:1 and 5:1. Pieces of gallium shot totaling between 1.5 g and 2.5 g were then placed in the crucibles. The alumina

crucibles were then placed in 13 mm diameter quartz tubes and evacuated under vacuum to a pressure near 10⁻⁴ Torr. The quartz tubes were then sealed using an oxygen-acetylene torch. The quartz tubes were placed in mullite tubes, then heated in commercial tube furnaces under heating profiles that increased the furnace temperature to 1000 °C in 10 hours, held the temperature constant for 48 hours, allowed the furnace to cool to 850 °C in 5 hours, held the temperature constant for an additional 48 hours, and then allowed the furnace to cool to room temperature in 60 hours.

After cooling, the quartz tubes were opened and the alumina crucibles were placed in a half-concentrated HCl bath in order to remove the excess gallium. Most of the gallium was removed after an overnight soak, but longer soaks were used without damage to the recovered product. Silver, hexagonal plates are produced in 40-50% yields, based on rhenium. Elemental analysis performed by EDS using a SEM showed that rhenium and boron were the only elements present in the crystals. The remainder of the product comprised ReGa_{4.5}.

HoMnB₄: Boron (3.5 mmol) and manganese (0.5 mmol) powders were mixed and added to an alumina crucible along with holmium (1.5 mmol) filings. Pieces of gallium shot totaling 1.5 g were added to the crucible before it was placed in a 13 mm diameter quartz tube and evacuated under vacuum to a pressure near 10⁻⁴ Torr. The quartz tube was then sealed using an oxygen-acetylene torch and placed in a mullite tube. Heating took place in a commercial tube furnace under a heating profiles that increased the furnace temperature to 1000 °C in 10 hours, held the temperature constant for 48 hours, allowed the furnace to cool to 850 °C in 5 hours, held the temperature constant for

an additional 48 hours, and then allowed the furnace to cool to room temperature in 60 hours.

After cooling, the quartz tubes were opened and the alumina crucibles were placed in a half-concentrated HCl bath in order to remove the excess gallium. Most of the gallium was removed after an overnight soak, but longer soaks were used without damage to the recovered product. Silver, plate-like crystals are a minor product (20-30% yields, based on manganese). Elemental analysis performed by Energy Dispersive Spectroscopy (EDS) using a Scanning Electron Microscope (SEM) showed that holmium, manganese, and boron were the only elements present in the crystals. The remainder of the product comprised MnGa₄, MnGa_{4.5}, traces of HoB₆, and unreacted boron.

REReB₄ (RE= Dy, Er, Yb): Boron and rhenium powders were added to alumina crucibles, along with filings from an ingot of a rare-earth metal, in millimolar quantities in a 1.5:1:4 ratio of RE:Re:B. Pieces of gallium shot totaling 2 g were placed atop the reagents in the crucibles. The alumina crucibles were then placed in an alumina boat, which was in turn place inside an alumina tube. The alumina tube was placed in a high-temperature tube furnace and heated under a slow flow of argon. The furnace was heated to 1400 °C in 8 hours and held at that temperature for 10 hours, then cooled to 1200 °C in 5 hours and held at that temperature for 10 hours, and finally cooled to 500 °C in 36 hours, at which point the power to the furnace was shut off and the furnace was allowed to cool to room temperature.

After cooling, the crucibles were removed from the boats in the tube and placed in a half-concentrated HCl bath in order to remove excess the gallium. An overnight soak

was adequate to remove the gallium. DyReB₄ and ErReB₄ were collected in estimated 30-50% yields based on rhenium. YbReB₄ was collected in an estimated 20-40% yield based on rhenium. Side products in the DyReB₄ reaction included ReGa_{4.5} and DyB₆. Side products in the ErReB₄ reaction included ReGa_{4.5} and ErB₆. Side products in the YbReB₄ reaction included ReGa_{4.5} and YbB₆.

C. Physical Measurements

Energy Dispersive Spectroscopy: Energy dispersive spectroscopy (EDS) analyses were carried out on selected crystals to determine their chemical composition. The analyses were performed with a JEOL JSM-6400 scanning electron microscope (SEM) equipped with Noran Vantage Energy Dispersive Spectroscopy (Si:Li) detector and Norvar window for standardless quantization of elements with $Z \ge 4$. The crystals were affixed to an alumina sample holder with double-sided carbon tape. The EDS data were acquired at an accelerating voltage of 10 kV with a 30 to 60 second accumulation time.

Single-Crystal X-ray Crystallography: Single crystals were mounted on a glass fiber with super glue and their intensity data were collected on either a Bruker SMART platform CCD diffractometer, or a STOE IPDS II diffractometer using Mo Kα radiation at 50 kV and 40 mA.

Individual frames of REReB₄ (RE= Dy, Er, Yb) examined with the Bruker machine were collected with a 0.3° ω rotation. The SMART software was used for data collection, and SAINT¹⁶ software was used for data extraction and reduction. After

applying analytical absorption corrections, structure solution and refinement were completed using direct methods and the SHELXTL¹⁷ suite of programs.

Samples examined with the STOE (MnB, MnB₄, ReB₂, and HoMnB₄) had individual frames collected on a 34 cm image plate with a 60 second exposure time and a 1.0° ω rotation. The X-SHAPE¹⁸ and X-RED¹⁹ software packages were used for data extraction and reduction and to apply an analytical absorption correction. Direct methods and the SHELXTL suite were used to solve and refine the structures.

The crystal structure refinement data for MnB are found in Table 3-1. Atomic parameters previously reported⁵ for CrB were used as a starting point for the refinement of the structure. The atomic positions and isotropic displacement parameters are listed in Table 3-2. Anisotropic displacement parameters for the atoms are found in Table 3-3. The bond lengths in MnB and a count of those bonds are listed in Table 3-4.

The refinement data for MnB₄ are found in Table 3-5. The atomic parameters from CrB_4^{20} were used as a starting point for refinement of the structure. Parameters from previous reports on the structure of MnB₄^{21, 22} apply to the monoclinic space group C2/m (a = 5.5029, b = 5.3669, c = 2.9487, $\beta = 122.71$) and are not useful in the orthorhombic Immm space group. Atomic positions and isotropic parameters found in this study of MnB₄ are given in Table 3-6. Anisotropic displacement parameters for the atoms are listed in Table 3-7. The values for these parameters are quite high and may be the result of the twinning in the crystal or a modulated structure. The bond lengths in MnB₄ and a count of those bonds in the unit cell are listed in Table 3-8.

The crystal structure refinement data for ReB₂ are listed in Table 3-9. The atomic parameters reported in the first structural report¹⁰ were used as a starting point for the

refinement of the structure from our data. The atomic positions and isotropic displacement parameters we have found are listed in Table 3-10. Anisotropic displacement parameters for the atoms are listed in Table 3-11. Bond lengths and a count of those bonds in the structure are found in Table 3-12.

The crystal structure refinement data for HoMnB₄ are listed in Table 3-13. The atomic positions and isotropic displacement parameters for HoMnB₄ are listed in Table 3-14. The manganese atoms were distributed over split positions, so anisotropic parameters were not carried out for these atoms. Anisotropic displacement parameters for the remaining atoms are listed in Table 3-15. The anisotropic displacement parameters are high, especially for the boron atoms. Inadequate absorption correction, modulated structure, and a twinned crystal may all play a role in creating these high values. Given the similar crystal morphology between HoMnB₄ and MnB₄, crystal twinning is likely present.

The refinement data for REReB₄ (RE = Dy, Er) are listed in Table 3-16. The refinement data for YbReB₄ are listed in Table 3-17. The atomic parameters for YCrB₄²³ were used as a starting point for the refinement of our data, as all of these compounds are members of the YCrB₄ structure type. The atomic parameters and isotropic displacement parameters for REReB₄ (RE = Dy, Er, Yb) are listed in Table 3-18. The anisotropic displacement parameters for REReB₄ (RE = Dy, Er, Yb) are listed in Table 3-19. Inadequate absorption corrections are most likely responsible for the low values of the parameters for the heavy atoms in all of these compounds. The bond distances for HoMnB₄ and REReB₄ (RE = Dy, Er, Yb) are listed in Table 3-20.

Table 3-1. Crystal data and structure refinement for MnB.

Formula weight	65.75	
Temperature	293(2) K	
Wavelength	0.71073 Å	
Crystal system	Orthorhombic	
Space group	Cmcm	
Unit cell dimensions	a = 3.0113(6) Å	α= 90°
	b = 7.6733(15) Å	β= 90°

c = 2.9610(6) Å $\gamma = 90^{\circ}$

Volume 68.42(2) Å³

Z 4

Density (calculated) 6.383 g/cm³
Absorption coefficient 17.695 mm⁻¹

F(000) 120

Theta range for data collection 5.31 to 34.65°

Index ranges $-4 \le h \le 4, -12 \le k \le 12, -4 \le l \le 4$

Reflections collected 444

Independent reflections 92 [R(int) = 0.0299]

Completeness to theta = 34.65° 91.1 %

Refinement method Full-matrix least-squares on F²

Data / restraints / parameters 92 / 0 / 10

Goodness-of-fit on F^2 1.230 Final R indices [I>2sigma(I)] R1 = 0.0135, wR2 = 0.0324

R indices (all data) R1 = 0.0135, wR2 = 0.0324

Extinction coefficient 0.35(4)

R1 =
$$\sum ||F_o| - |F_c|| / \sum |F_o|$$
 and wR2 = $[\sum (|F_o^2 - F_c^2|)^2 / \sum (wF_o^2)^2]^{1/2}$

Table 3-2. Atomic coordinates ($x 10^4$) and equivalent isotropic displacement parameters ($Å^2x 10^3$) for MnB.

-	х	у	Z	U(eq)
Mn(1)	5000	1438(1)	2500	4(1)
B(1)	0	663(3)	-2500	5(1)

U(eq) is defined as one third of the trace of the orthogonalized U^{ij} tensor.

Table 3-3. Anisotropic displacement parameters $(Å^2x 10^3)$ for MnB.

	U11	U22	П33	U23	Π13	U12
Mn(1)	4(1)	4(1)	4(1)	0	0	0
B(1)	5(1)	5(1)	4(1)	0	0	0

The anisotropic displacement factor exponent takes the form: $-2\pi^2$ [h^2 $a^{*2}U^{11} + ... + 2h$ k a^* b^* U^{12}].

Table 3-4. Bond distances (Å) for MnB.

Mn1	B1	4x	2.1937(3)
Mnl	B1	2x	2.2059(3)
Mnl	B1	1x	2.2245(4)
B1	B1	2x	1.7966(3)
B1	Mnl	4x	2.1937(3)
B1	Mnl	2x	2.2059(3)
B1	Mnl	1x	2.2245(4)

Table 3-5. Crystal data and structure refinement for MnB₄

Formula weight	98.18
Temperature	293(2) K
Wavelength	0.71073 Å
Crystal system	Orthorhombic

Space group Immm

Unit cell dimensions a = 2.9380(6) Å $\alpha = 90^{\circ}$

b = 4.6104(9) Å $\beta = 90^{\circ}$

c = 5.3528(11) Å $\gamma = 90^{\circ}$

Volume 72.51(3) Å³

Z 2

Density (calculated) 4.497 g/cm³

Absorption coefficient 8.403 mm⁻¹

F(000) 90

Theta range for data collection 5.84 to 36.51°

Index ranges $-4 \le h \le 4, -7 \le k \le 7, -8 \le l \le 8$

Reflections collected 589

Independent reflections 119 [R(int) = 0.0512]

Completeness to theta = 36.51° 96.7 %

Refinement method Full-matrix least-squares on F²

Data / restraints / parameters 119 / 0 / 11

Goodness-of-fit on F² 1.255

Final R indices [I>2sigma(I)] R1 = 0.0355, wR2 = 0.0854 R indices (all data) R1 = 0.0355, wR2 = 0.0854

Extinction coefficient 0.61(13)

$$R1 = \sum ||F_o| - |F_c|| / \sum |F_o|$$
 and $wR2 = [\sum (|F_o^2 - F_c^2|)^2 / \sum (wF_o^2)^2]^{1/2}$

Table 3-6. Atomic coordinates (\times 10⁴) and equivalent isotropic displacement parameters (Å²x 10³) for MnB₄.

	х	у	Z	U(eq)
Mn(1)	0	0	0	8(1)
B(1)	0	1995(13)	3440(11)	28(1)

U(eq) is defined as one third of the trace of the orthogonalized U^{ij} tensor.

Table 3-7. Anisotropic displacement parameters (Å²x 10³) for MnB₄.

	U11	U22	U33	U ²³	U13	U12
Mn(1)	22(1)	2(1)	1(1)	0	0	0
B(1)	3(1)	45(3)	35(2)	-38(2)	0	0

The anisotropic displacement factor exponent takes the form: $-2\pi^2$ [h^2 $a^{*2}U^{11} + ... + 2h$ k a^* b^* U^{12}]

Table 3-8. Bond distances (Å) for MnB₄.

Mn1	B 1	4x	2.0580(3)
Mn1	B1	8x	2.1853(3)
B1	B1	1x	1.6706(3)
Bl	B1	1x	1.8391(4)
B1	B1	2x	1.8403(3)

Table 3-9. Crystal data and structure refinement for ReB₂.

Formula weight 207.82

Temperature 293(2) K

Wavelength 0.71073 Å

Crystal system Hexagonal

Space group P63/mmc

Unit cell dimensions a = 2.8891(4) Å $\alpha = 90^{\circ}$

b = 2.8891(4) Å $\beta = 90^{\circ}$

c = 7.4606(15) Å $\gamma = 120^{\circ}$

Volume 53.930(15) Å³

Z 2

Density (calculated) 12.798 g/cm³
Absorption coefficient 111.675 mm⁻¹

F(000) 170

Crystal size $0.140 \times 0.140 \times 0.010 \text{ mm}^3$

Theta range for data collection 8.17 to 35.91°

Index ranges $-1 \le h \le 4, -4 \le k \le 4, -8 \le l \le 11$

Reflections collected 270

Independent reflections 66 [R(int) = 0.0842]

Completeness to theta = 35.91° 89.9 %

Refinement method Full-matrix least-squares on F²

Data / restraints / parameters 66 / 0 / 7

Goodness-of-fit on F² 1.352

Final R indices [I>2sigma(I)] R1 = 0.0218, wR2 = 0.0509 R indices (all data) R1 = 0.0263, wR2 = 0.0517

Extinction coefficient 0.091(17)

 $R1 = \sum ||F_o| - |F_c|| / \sum |F_o|$ and $wR2 = [\sum (|F_o|^2 - F_c|^2)^2 / \sum (wF_o|^2)^2]^{1/2}$

Table 3-10. Atomic coordinates ($x 10^4$) and equivalent isotropic displacement parameters ($\mathring{A}^2x 10^3$) for ReB₂.

	x	У	z	U(eq)
Re(1)	6667	3333	2500	2(1)
B(1)	6667	3333	5460(20)	1(2)

U(eq) is defined as one third of the trace of the orthogonalized U^{ij} tensor.

Table 3-11. Anisotropic displacement parameters (Å²x 10³) for ReB₂.

	Π_{11}	U22	U33	U ²³	Π13	U12
Re(1)	1(1)	1(1)	5(1)	0	0	1(1)
B(1)	1(3)	1(3)	0(4)	0	0	1(2)

The anisotropic displacement factor exponent takes the form: $-2\pi^2$ [h^2 $a^{*2}U^{11} + ... + 2h$ k a^* b^* U^{12}]

Table 3-12. Bond distances (Å) for ReB₂.

Rel	B1	2x	2.2094(4)
Rel	B1	6x	2.2573(3)
B1	B1	3x	1.8045(2)
B1	Rel	1x	2.2094(4)
B1	Rel	3x	2.2573(3)

Table 3-13. Crystal data and structure refinement for HoMnB₄.

Formula weight

r ommuna worghi	203.11	
Temperature	293(2) K	
Wavelength	0.71073 Å	
Crystal system	Orthorhombic	
Space group	Pbam	
Unit cell dimensions	a = 5.8946(12) Å	α= 90°
	b = 11.411(2) Å	β= 90°
	c = 3.4041(7) Å	γ= 90°
Volume	228.96(8) Å ³	
Z	4	
Density (calculated)	7.633 g/cm^3	
Absorption coefficient	39.388 mm ⁻¹	
F(000)	448	

263.11

Theta range for data collection 4.97 to 36.07°

Index ranges $-9 \le h \le 9, -17 \le k \le 18, -5 \le l \le 4$

Reflections collected 3176

Independent reflections 606 [R(int) = 0.1861]

Completeness to theta = 36.07° 97.9 %

Refinement method Full-matrix least-squares on F²

Data / restraints / parameters 606 / 0 / 38

Goodness-of-fit on F² 1.118

Final R indices [I>2sigma(I)] R1 = 0.0949, wR2 = 0.2203 R indices (all data) R1 = 0.1477, wR2 = 0.2535

Extinction coefficient 0.033(8)

 $R1 = \sum ||F_o| - |F_c|| / \sum |F_o|$ and $wR2 = [\sum (|F_o^2 - F_c^2|)^2 / \sum (wF_o^2)^2]^{1/2}$

Table 3-14. Atomic coordinates (x 10^4) and equivalent isotropic displacement parameters ($Å^2x 10^3$) for HoMnB₄.

	x	y	Z	U(eq)	Occupancy
Mn(1)	8711(10)	5846(5)	-5000	10(1)	0.86728
Mn(15)	8400(60)	6470(30)	-5000	10(1)	0.13272
Ho(1)	6278(3)	3495(1)	5000	14(1)	
B(2)	8700(100)	4520(30)	0	19(8)	
B(3)	6480(110)	5350(50)	0	35(15)	
B(4)	7110(70)	6830(30)	0	14(6)	
B(5)	10200(50)	6930(40)	0	18(7)	

U(eq) is defined as one third of the trace of the orthogonalized Uij tensor.

Table 3-15. Anisotropic displacement parameters (Å²x 10³) for HoMnB₄.

	U11	U22	U33	U ²³	U13	U12
Ho(1)	16(1)	15(1)	10(1)	0	0	0(1)
B(2)	50(20)	5(11)	2(9)	0	0	19(18)
B(3)	60(30)	40(20)	4(11)	0	0	60(30)
B(4)	31(18)	6(11)	6(11)	0	0	8(13)
B(5)	0(9)	30(19)	24(18)	0	0	10(11)

The anisotropic displacement factor exponent takes the form: $-2\pi^2[h^2 a^{*2}U^{11} + ... + 2h]$

k a* b* U12]

Table 3-16. Crystal data and structure refinement for REReB₄ (RE= Dy, Er).

Formula	DyReB ₄	ErReB ₄
Formula weight	391.94	396.70
Crystal system	Orthorhombic	Orthorhombic
Space group	Pbam	Pbam
Unit cell dimensions	a = 5.9710(12) Å	a = 5.9490(12) Å
	b = 11.545(2) Å	b = 11.508(2) Å
	c = 3.5980(7) Å	c = 3.5820(7) Å
Volume	248.03(9) Å ³	245.23(8) Å ³
Z, Density (calculated)	4, 10.496 g/cm ³	4, 10.745 g/cm ³
Absorption coefficient	78.259 mm ⁻¹	82.905 mm ⁻¹
F(000)	644	652
Crystal size, mm	0.044 x 0.044 x 0.064	0.038 x 0.046 x 0.050
Theta range for data collection	3.53 to 28.06°	3.54 to 28.08°
Index ranges	$-7 \le h \le 7,$	$-7 \le h \le 7$,
	$-14 \le k \le 15,$	$-14 \le k \le 15,$
	$-4 \le l \le 4$	$-4 \le l \le 4$
Reflections collected	2410	2459
Independent reflections	340 [R(int) = 0.0490]	335 [R(int) = 0.0559]
Completeness to θ_{max}	97.7 %	97.1 %
Refinement method	Full-matrix least-square	es on F ²
Data / restraints / parameters	340 / 0 / 38	335 / 0 / 38
Goodness-of-fit on F ²	1.064	1.131
Final R indices [I>2σ(I)]	R1 = 0.0275,	R1 = 0.0395,
	wR2 = 0.0788	wR2 = 0.0887
R indices (all data)	R1 = 0.0278,	R1 = 0.0413,
	wR2 = 0.0790	wR2 = 0.0898
Extinction coefficient	0.0324 (18)	0.00138(11)

R1 = $\sum ||F_o| - |F_c|| / \sum |F_o|$ and wR2 = $[\sum (|F_o|^2 - F_c|^2)^2 / \sum (wF_o|^2)^2]^{1/2}$

Table 3-17. Crystal data and structure refinement for YbReB₄

Formula weight 402.48

Temperature 273(2) K

Wavelength 0.71073 Å

Crystal system Orthorhombic

Space group Pbam

Unit cell dimensions a = 5.9273(9) Å $\alpha = 90^{\circ}$

b = 11.4497(18) Å $\beta = 90^{\circ}$

c = 3.5617(6) Å $\gamma = 90^{\circ}$

Volume 241.72(7) Å³

Z 4

Density (calculated) 11.060 g/cm³
Absorption coefficient 88.080 mm⁻¹

F(000) 660

Crystal size $0.052 \times 0.052 \times 0.104 \text{ mm}^3$

Theta range for data collection 3.56 to 28.28°

Index ranges $-7 \le h \le 7, -14 \le k \le 15, -4 \le l \le 4$

Reflections collected 2363

Independent reflections 333 [R(int) = 0.0605]

Completeness to theta = 28.28° 96.2 %

Refinement method Full-matrix least-squares on F²

Data / restraints / parameters 333 / 0 / 38

Goodness-of-fit on F² 1.143

Final R indices [I>2sigma(I)] R1 = 0.0431, wR2 = 0.1076

R indices (all data) R1 = 0.0448, wR2 = 0.1088

Extinction coefficient 0.0134(13)

R1 = $\sum ||F_o| - |F_c|| / \sum |F_o|$ and wR2 = $[\sum (|F_o|^2 - F_c|^2)^2 / \sum (wF_o|^2)^2]^{1/2}$

Table 3-18. Atomic coordinates (x 10^4) and equivalent isotropic displacement parameters ($Å^2x$ 10^3) for REReB₄ (RE = Dy, Er, Yb).

	x	у	z	U(eq)
Re(1)	1328(1)	4133(1)	0	2(1)
Dy(2)	1264(1)	1504(1)	0	2(1)
B(1)	2860(30)	3183(14)	-5000	3(3)
B(2)	-240(30)	3087(15)	-5000	6(3)
B(3)	-1130(30)	4520(17)	-5000	7(3)
B(4)	3630(30)	4703(16)	-5000	6(3)
Re(1)	1335(1)	4131(1)	0	0(1)
Er(2)	1267(2)	1502(1)	0	0(1)
B(1)	2860(40)	3140(20)	5000	1(4)
B(2)	3850(40)	490(20)	5000	2(5)
B(3)	4770(40)	1920(20)	5000	1(5)
B(4)	3650(40)	4700(20)	5000	3(5)
Yb(1)	1271(2)	1501(1)	0	0(1)
Re(2)	1339(2)	4132(1)	0	2(1)
B(1)	3610(50)	4690(20)	5000	4(6)
B(2)	1120(50)	5510(30)	5000	3(6)
B(3)	2830(50)	3140(30)	5000	4(6)
B(4)	-170(60)	3070(30)	5000	9(6)

U(eq) is defined as one third of the trace of the orthogonalized U^{ij} tensor.

Table 3-19. Anisotropic displacement parameters ($Å^2x\ 10^3$) for REReB₄ (RE = Dy, Er, Yb).

	Ω_{11}	U^{22}	U33	U ²³	П ₁₃	U12
Re(1)	2(1)	0(1)	4(1)	0	0	0(1)
Dy(2)	1(1)	0(1)	4(1)	0	0	0(1)
B(1)	4(7)	0(8)	6(8)	0	0	-3(6)
B(2)	4(7)	0(7)	13(8)	0	0	0(6)
B(3)	5(7)	4(8)	11(9)	0	0	5(6)
B(4)	2(7)	6(9)	11(8)	0	0	0(6)
Re(1)	0(1)	0(1)	0(1)	0	0	1(1)
Er(2)	0(1)	0(1)	0(1)	0	0	0(1)
B(1)	3(11)	0(11)	0(11)	0	0	0(9)
B(2)	1(11)	5(11)	0(11)	0	0	-5(9)
B(3)	0(10)	0(11)	3(11)	0	0	5(8)
B(4)	0(10)	0(11)	8(12)	0	0	1(8)
Yb(1)	0(1)	1(1)	0(1)	0	0	0(1)
Re(2)	2(1)	4(1)	0(1)	0	0	1(1)
B(1)	11(13)	0(12)	0(12)	0	0	15(11)
B(2)	7(14)	0(12)	3(13)	0	0	0(10)
B(3)	11(14)	0(12)	0(13)	0	0	2(11)
B(4)	18(16)	0(13)	10(15)	0	0	-4(12)

The anisotropic displacement factor exponent takes the form: $-2\pi^2$ [h^2 $a^{*2}U^{11} + ... + 2h$ k a^* b^* U^{12}]

Table 3-20. Bond distances (Å) for HoMnB₄ and REReB₄ (RE = Dy, Er, Yb).

	HoMnB ₄	DyReB ₄	ErReB ₄	YbReB ₄
RE(1)–M(1)	2.76(3)	3.0359(11)	3.0230(13)	3.0115(14)
M(1)–M(1)	2.457(11)	2.5537(11)	2.5546(17)	2.545(2)
M(1)–B(1)	2.28(2)	2.298(11)	2.309(16)	2.32(2)
M(1)–B(2)	2.22(5)	2.361(11)	2.364(15)	2.340(19)
M(1)–B(3)	2.25(2)	2.366(10)	2.357(16)	2.290(19)
M(1)–B(4)	2.28(3)	2.357(10)	2.352(15)	2.33(2)
RE(1)–B(1)	2.51(4)	2.737(12)	2.734(18)	2.74(2)
RE(1)–B(2)	2.72(4)	2.718(13)	2.632(19)	2.62(2)
RE(1)-B(3)	2.65(3)	2.655(13)	2.699(19)	2.74(2)
RE(1)-B(4)	2.61(3)	2.750(14)	2.739(19)	2.67(3)
B(1)-B(2)	1.61(7)	1.86(3)	1.80(4)	1.80(7)
B(1)–B(4)	1.78(5)	1.81(2)	1.86(4)	1.83(4)
B(2)–B(3)	1.83(5)	1.74(3)	1.74(4)	1.74(4)
B(3)–B(3)	1.92(15)	1.75(4)	1.84(4)	1.77(6)
B(3)–B(4)	1.73(7)	1.74(2)	1.74(3)	1.72(5)
B(4)–B(4)	1.89(12)	1.78(3)	1.75(5)	1.82(5)

D. Structural Description

MnB: The structure of MnB, shown in Figure 3-1a, is composed of trigonal prisms of manganese atoms centered by a zigzag chain of boron atoms. The most interesting feature of the structure is the arrangement of the prisms and chains. Normally, MnB crystallizes with the FeB-type structure (Figure 3-1b), where the prisms share corners. We have isolated a variant phase of MnB that crystallizes in the CrB structure-type (Figure 3-1c) where the prisms in each layer share trigonal faces. The layers in the CrB-type MnB are more distinct, but overall, the two structure types are very similar. Actually, the volume of this MnB phase is only 0.3% less than the volume of the FeB-type.

As mentioned in the introduction to this chapter, CrB-type MnB has been reported.^{2, 3} However, the powder pattern in each of the previous reports also showed lines attributed to FeB-type MnB. We saw no evidence of disorder in our diffraction data suggesting a mix of the FeB and CrB-structure types, as seen by Kanaizuka.² Manganese was the only metal atom detected by the refinement of the atom occupancy during refinement. EDS analyses on the single crystals confirm this finding.

MnB₄: The structure of MnB₄ reported here is analogous to that first found for CrB₄,²⁰ and may be the "semi-MnB₄" structure described by Burdett and Canadell.¹ The defining feature in the structure of MnB₄ (Figure 3-2a) is a three-dimensional network of boron atoms. The network comprises boron atom rectangles lying parallel to the *bc*-plane that bond to boron atoms in other rectangles, extending the network in all three dimensions. The manganese atoms sit in the middle of channels formed by six neighboring rectangles.

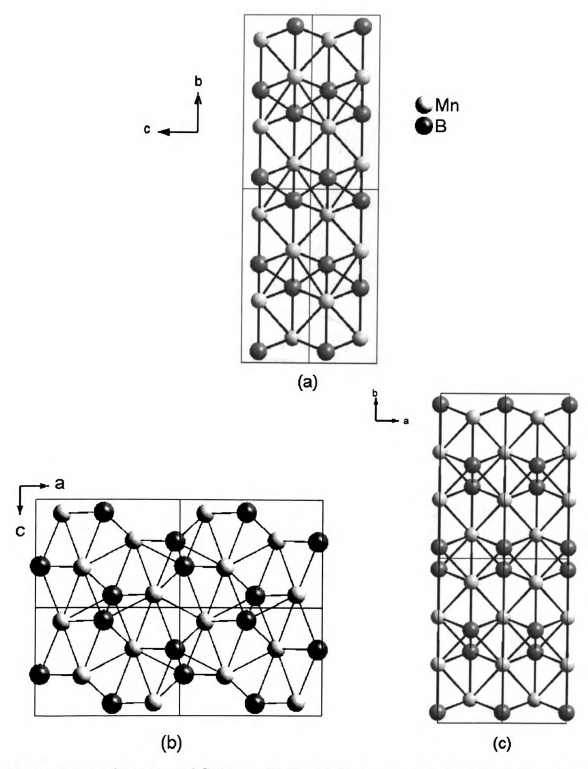


Figure 3-1. (a) Structure of CrB-type MnB with boron atom chains parallel to page. The boron atom chains are perpendicular to the page in (b) FeB-type MnB and (c) CrB-type MnB.

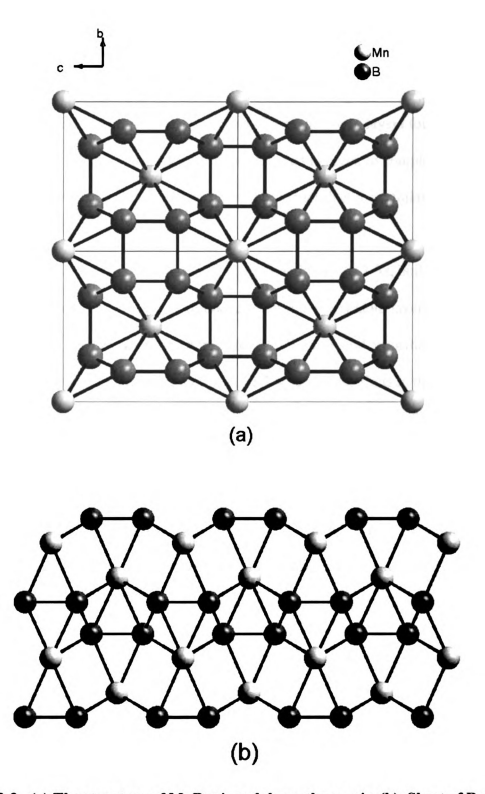


Figure 3-2. (a) The structure of MnB $_4$ viewed down the a-axis (b) Sheet of RuB $_2$ with similarly puckered hexagonal sheets of B atoms..

An alternate way to consider the structure is in terms of layers. From this perspective, the structure is made of puckered hexagonal layers of boron atoms, with layers of manganese atoms centering the boron hexagons. The boron layers are puckered in the boat-type confirmation, which is very similar to the boron layers found in RuB₂ (Figure 3-2b). The interlayer bonds, which would need to break to completely reduce the MnB₄ structure into separate RuB₂-type layers, are longer than the intralayer bonds by about 8%.

ReB₂: Rhenium diboride has a structure, seen in Figure 3-3a, built along the *c*-axis by puckered hexagonal layers of boron atoms and metal atom layers where rhenium atoms sit directly above the boron atoms in the 1, 3, and 5 positions of the hexagon in one layer and above the atoms in the 2, 4, and 6 positions in the next boron layer. The layers in ReB₂ (Figure 3-3b) display hexagons in a chair conformation, in contrast to the planar hexagons in AlB₂-type structures and the boat conformation for boron hexagons in RuB₂-type structures. The distance between rhenium atoms in the *c*-direction is larger than the bonding distance for rhenium–rhenium bonds. Similarly, the distances between successive boron layers are larger than boron–boron bonding distances, suggesting that the structure is held together along the *c*-axis only through rhenium–boron bonds.

HoMnB₄ and REReB₄ (RE = Dy, Er, Yb): The group 7 ternary borides we have synthesized all crystallize in the YCrB₄ structure type. This structure type (Figure 3-4a) has an interesting 2-D network of boron atoms. The boron atoms form both 5- and 7-membered rings that sit in one planar layer. The metal atoms in the structure reside in their own layer, halfway between boron layers. The rare earth atoms sit below the

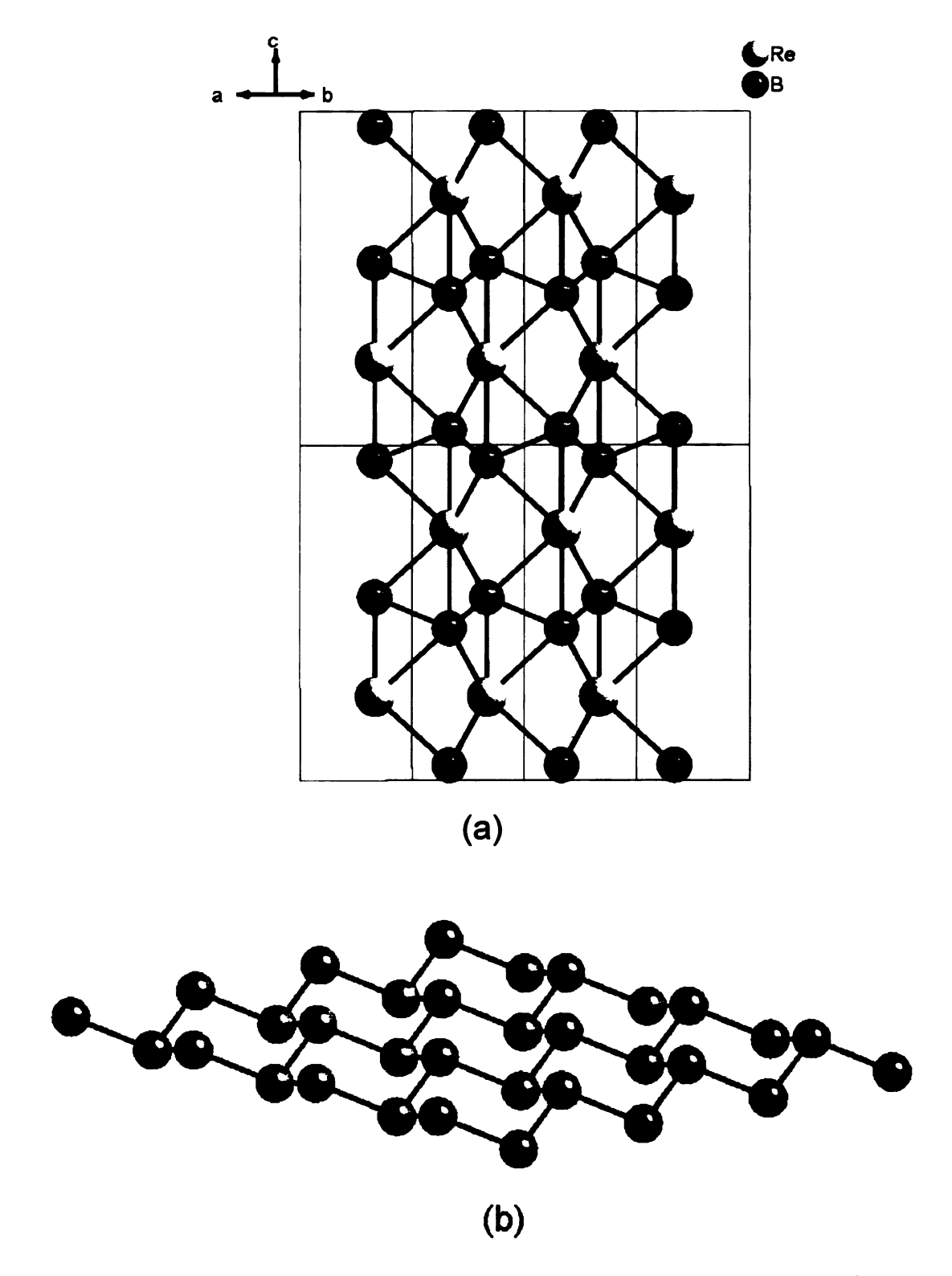
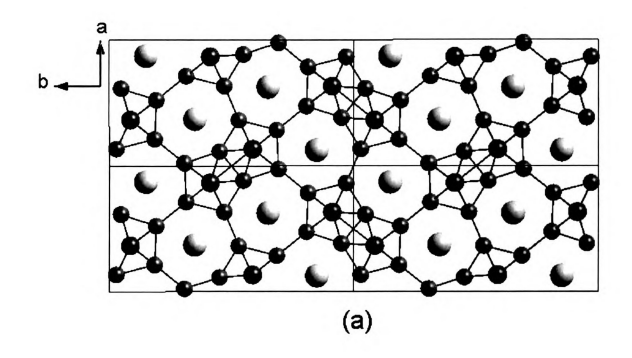


Figure 3-3. (a) Structure of ReB_2 and (b) an individual graphite-like layer of boron atoms.



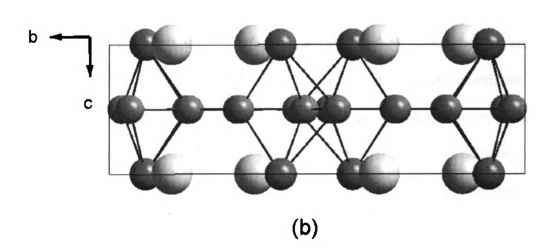


Figure 3-4. (a) Structure of YCB_4 -type compounds (b) View down a-axis showing alternating layers of metal atoms and boron atoms.

centers of the 7-membered rings, while the transition metals sit below the centers of the 5-membered rings.

Generally, when the B:M ratio reaches 2.0, a layered structure results. The boron atoms in these layers typically have a hexagonal arrangement, planar or puckered conformation depending on the metal. The rare earth atoms and transition metals in the YCrB₄ structure type have such different radii that the rings must also be of different sizes. The boron atoms accommodate the metals by moving from 6-membered rings to the 5- and 7-membered rings.

E. Results and Discussion

All of the compounds described in this chapter have been previously synthesized using traditional solid state methods. However, single crystals have not been previously isolated for all of these compounds. Our group has used the molten metal flux technique in the synthesis and crystallization of all these compounds. Gallium was the only molten metal from which the group 7 borides would grow. Reactions using aluminum, copper, indium, or tin as the flux metal did not yield borides as a product. The products from these reactions were generally binary phases of either manganese or rhenium and the flux metal. Our success using a gallium flux should be seen as a starting point for further research, because our synthesis procedures were not optimized.

MnB: One of the main problems encountered in the synthesis of MnB was in picking the crystals out from the entire reaction product. The majority of the product from the initial MnB reaction was actually MnSi. The alumina crucibles used for this reaction had a cement bottom and we concluded that the gallium flux pulled silicon out of

the cement and into the reaction. The crystals for MnB and MnSi look nearly identical, so EDS on the crystal is necessary to ensure that only manganese and boron are present in the crystal. Reactions with identical conditions were carried out again, except in purely alumina crucibles. These reactions produced some crystals, but still in low yields. In these reactions, the major products were manganese gallides, which will be discussed in a later chapter of this work. Crystals of the gallides can also look like the MnB phase, so again it was difficult to separate boride crystals from the product mixtures.

MnB₄: The crystals of MnB₄, while easier to identify, do not form single crystals. We believe that the crystals we have isolated are a series of thin plates stacked atop each other. This stacking leads to the ridged appearance of the crystals (Figure 3-5). For the "single crystal" diffraction study a specimen with the smoothest faces possible was selected. The most intense peaks were used to index the unit cell. While this technique was in no way an ideal method, the results do give some structural insight.

As noted, the crystal were indexed in an orthorhombic cell to match CrB₄, rather than the monoclinic cell used in previous studies on MnB₄.^{21, 22} The previous studies found a 0.3° deviation from a 90° angle for the β angle when the cell was transformed to the orthorhombic *I* setting. In our crystal, the largest deviation from 90° was approximately 0.15°, changing slightly when different orientations of the cell were used. These findings are inconclusive because of the aforementioned imperfections of the specimen. The quality of the data from previous studies has also been questioned. Further research is needed to see whether MnB₄ really crystallizes in the orthorhombic *I* setting, or if our metal flux synthesis is trapping a metastable phase of the compound.



Figure 3-5. SEM micrograph of a MnB₄ crystal.

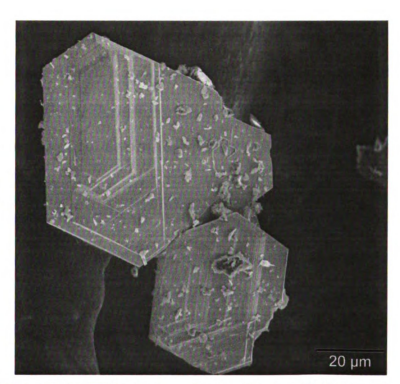


Figure 3-6. SEM micrograph of a cluster of ReB2 crystals.

ReB₂: At a lower flux reaction temperature (1000°C) ReB₂ crystals are thin hexagonal plates. The plates turn into hexagonal prisms at a higher flux reaction temperature (1400°C), with the prisms narrowing toward each end. The hexagonal plates will often grow together, forming clusters of plates (Figure 3-6). Single plates are often available, but they can be manually broken from these clusters if needed. An optimized synthesis would help increase yields of the plates, making physical property measurements easier. Property measurements have not been carried out because of the time consuming separation of enough crystals for measurement.

HoMnB₄: The synthesis of HoMnB₄ is very similar to MnB₄ and faces similar obstacles to single crystal isolation. Crystals of HoMnB₄ (Figure 3-7) are thin plates and appear to also have the ridges seen in the MnB₄ crystals. The diffraction data did not show any obvious signs of twinned or intergrown crystals, but the quality of the refinement data is not as high as is expected for a true single crystal. Reactions specifically targeting this compound are needed to obtain better crystals, not only for better diffraction studies, but also for other physical properties measurements, especially magnetic measurements.

REReB₄ (RE = Dy, Er, Yb): The ternary rhenium borides were first seen in reactions heated to 1000°C, but the crystals were very small and poorly formed.

Reactions were repeated at 1400°C and the crystals grew larger and better formed despite shorter soaking and cooling times. A crystal of DyReB₄ is shown in Figure 3-8.

Reactions including other rare earth elements yielded similar looking products, but a short scan on the single crystal machine revealed that the rare earth tetraboride had

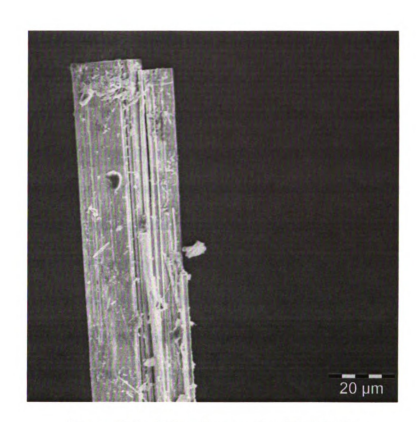


Figure 3-7. SEM micrograph of HoMnB₄.



Figure 3-8. SEM micrograph of DyReB4.

formed. Rhenium diboride and rhenium gallides, which are discussed later in this work, also crystallized from these reactions.

The refinements on the single crystals of these ternary rhenium borides are consistently accurate. Problems do arise are in the displacement parameters, both isotropic and anisotropic. These problems were a bit unexpected since the crystal faces were measured, indexed, and then used to make an analytical absorption correction. Low temperature diffraction studies may be needed to reduce the thermal motion of the atoms.

General Discussion: The gallium flux is a useful medium in the synthesis of group 7 borides. The exploratory nature of our research in this group changed after finding MnB and MnB₄, focusing more on repeating and optimizing reactions aimed at these products. While some improvements were made, there is still a great deal of synthesis refinement to be done. Further research should also be carried out, searching for the "missing" Mn₅B₃ and Mn₂B₃ phases mentioned in the introduction to this chapter. Ternary systems with the rare earths should also continue to yield results. Even if the structures have been reported before, very few have had any physical properties measured. The large crystals grown from molten gallium would be ideal specimens to investigate.

The only binary rhenium boride we focused on was ReB₂, so further research into this system needs to consider Re₃B and Re₇B₃. Exploratory work should also be carried out to see if the flux can isolate other phases that traditional syntheses can not. This work should also carry-over into the synthesis of ternary systems, especially since it has been successfully performed with rare earth metals. As with manganese, compounds have been structurally characterized, but their physical properties remain unmeasured.

F. Conclusions

In this chapter we successfully used a molten gallium as a solvent to synthesize and grow crystals of MnB, MnB₄, ReB₂, HoMnB₄, DyReB₄, ErReB₄, and YbReB₄. While the structural characterization of some compounds needs additional work, the overall picture is encouraging. The synthesis of ternary borides is especially encouraging, since the technique was unsuccessful with group 6 borides. These results set a foundation for continued research into group 7 borides using the metal flux technique.

References

- 1. Burdett, J. K.; Canadell, E., CrB₄ and MnB₄: Electronic Structures of Two Unusual Systems Containing the Tetragonal Carbon Net. *Inorganic Chemistry* **1988**, 27, 4437-4444.
- 2. Kanaizuka, T., Phase Diagram of Pseudobinary CrB-MnB and MnB-FeB Systems: Crystal Structure of the Low Temperature Modification of FeB. *Journal of Solid State Chemistry* **1982**, 41, 195-204.
- 3. Papesch, G.; Nowotny, H.; Benesovsky, F., Untersuchungen in den Systemen: Chrom-Bor-Kohlenstoff, Mangan-Bor-Kohlenstoff und Mangan-Germanium-Kohlenstoff. *Monatshefte für Chemie* **1973**, 104, 933-942.
- 4. Becher, H. J.; Krogmann, K.; Peisker, E., Über das ternäre Borid Mn₂AlB₂. Zeitschrift für anorganische und allgemeine Chemie 1966, 344, (3-4), 140-147.
- 5. Okada, S.; Atoda, T.; Higashi, I., Structural Investigation of Cr₂B₃, Cr₃B₄, and CrB by Single-Crystal Diffractometry. *Journal of Solid State Chemistry* **1987**, 68, 61-67.
- 6. Okada, S.; Atoda, T.; Higashi, I.; Takahashi, Y., Preparation of Single Crystals of MoB₂ by the Aluminum-flux Technique and Some of Their Properties. *Journal of Materials Science* **1987**, 22, 2993-2999.
- 7. Higashi, I.; Takahashi, Y.; Atoda, T., Crystal Growth of Borides and Carbides of Transition Metals from Molten Aluminum Solutions. *Journal of Crystal Growth* 1976, 33, 207-211.
- 8. Okada, S.; Kudou, K.; Lundström, T., Preparations and Some Properties of W₂B, δ-WB, and WB₂ Crystals from High-Temperature Metal Solutions. *Japanese Journal of Applied Physics* **1995**, 34, (1), 226-231.
- 9. Aronsson, B.; Backman, M.; Rundqvist, S., The Crystal Structure of Re₃B. Acta Chemica Scandinavica 1960, 14, 1001-1005.
- 10. Placa, S. L.; Post, B., The Crystal Structure of Rhenium Diboride. *Acta Crystallographica* **1962**, 15, 97-99.
- 11. Aronsson, B.; Stenberg, E.; Aselius, J., Borides of Rhenium and the Platinum Metals. *Acta Chemica Scandinavica* **1960**, 14, 733-741.
- 12. Ishii, T.; Shimada, M.; Koizumi, M.; Sakakibara, T.; Date, M., Magnetic Properties of Mn₃B₄ Under High Magnetic Field. Solid State Communications 1984, 51, (2), 103-105.
- 13. Ishii, T.; Shimada, M.; Koizumi, M., Synthesis and Magnetic Properties of (Mn₁. _xCr_x)₃B₄ and (Mn_{1-x}Mo_x)₃B₄. *Inorganic Chemistry* **1982**, 21, 1670-1674.

- 14. Kawano, A.; Mizuta, Y.; Takagiwa, H.; Muranaka, T.; Akimitsu, J., The Superconductivity in Re-B System. *Journal of the Physical Society of Japan* **2003**, 72, (7), 1724-1728.
- 15. Strukova, G. K.; Degtyareva, V. F.; Shovkun, D. V.; Zverev, V. N.; Kiiko, V. M.; Ionov, A. M.; Chaika, A. N., Superconductivity in the Re-B System. *eprint arXiv:cond-mat/0105293* **2001**.
- 16. Sheldrick, G. M. SAINT, Version 4; Siemens Analytical X-Ray Instruments, Inc.: Madison, WI.
- 17. Sheldrick, G. M. SHELXTL Structure Determination Program, Version 5.0; Siemens Analytical X-Ray Instruments, Inc.: Madison, WI, 1995.
- 18. X-SHAPE, Version 2.05; STOE & Cie GmbH: 2004.
- 19. X-RED 32, Version 1.10; STOE & Cie GmbH: 2004.
- 20. Andersson, S.; Lundström, T., The Crystal Structure of CrB₄. Acta Chemica Scandinavica 1968, 22, 3103-3110.
- 21. Andersson, S., A Note on the Crystal Structure of MnB₄. Acta Chemica Scandinavica 1969, 23, (2), 687-688.
- 22. Andersson, S.; Carlsson, J.-O., The Crystal Structure of MnB₄. Acta Chemica Scandinavica 1970, 24, (5), 1791-1799.
- 23. Kuz'ma., Y. B., Crystal Structure of the compound YCrB₄ and its analogs. Kristallografiya 1970, 15, 372-374.

CHAPTER FOUR

The Metal Flux Synthesis of Ruthenium Borides

A. Introduction

The structure and composition of many binary borides have been reported for the past half-century. However, few of the physical properties of these compounds have ever been reported. The discovery of superconductivity in MgB₂ in 2001¹ has renewed interest in binary borides of all kinds. This finding led to a study of group 8 borides by the Kaner group in 2005, who first reported on the hardness and incompressibility of osmium diboride.² While the structures of OsB₂ and RuB₂ were first reported in 1962,³ property studies have been limited to a single report on their superconductivity in 1975⁴ and a few reports on the electronic structures of the compounds⁵⁻⁷ in the past decade. Chapnik⁸ actually called for further study on these unique compounds, and we were interested in preparing single crystals to investigate the unknown physical properties of group 8 binary borides.

Physical measurements carried out on single crystals are advantageous in eliminating minor phases in powdered samples and allow researchers to search for anisotropy in the properties of the compound. Single crystals of the ruthenium borides have been isolated from arc-melted pellets, but we were interested in using the molten metal flux technique to grow higher quality crystals. Our success in synthesizing and crystallizing borides from groups 6 and 7 and reports of ternary rhodium borides grown

from flux⁹ led us to believe that the technique could also work for ruthenium borides.

The reports of ternary rhodium borides from flux synthesis also inspired us to investigate ternary ruthenium borides as well.

In this chapter we report on the synthesis and crystal growth of the known compounds Ru_7B_3 , Ru_2B_3 , RuB_2 , and $RERu_4B_4$ (RE = Y, Ce, Sm, Dy, and Yb). A new phase of ruthenium diboride, β -RuB₂, crystallizing in the ReB_2 -type structure is presented. A brief report on two ternary borides, $Pr_x(Ru_4B_4)_y$ and $Nd_x(Ru_4B_4)_y$, with modulated structures follows as well.

B. Experimental

Reagents:

All reagents were used as received without further purification: (i) Boron metal, 99% purity, -325 mesh, Cerac Specialty Inorganics, Milwaukee, WI, (ii) Ruthenium metal, 99.95% purity, -325 mesh, Cerac Specialty Inorganics, Milwaukee, WI, (iii) Copper shot, 99% purity, -3 +14 mesh, Aldrich Chemical Company, Milwaukee, WI, (iv) Yttrium metal, 99.9% purity, -40 mesh, Cerac Specialty Inorganics, Milwaukee, WI, (v) Dysprosium metal (filed from ingot) 99.9% purity, Chinese Rare Earth Information Center, Inner Mongolia, China, (vi) Cerium metal (filed from ingot) 99.9% purity, Chinese Rare Earth Information Center, Inner Mongolia, China, (vii) Samarium metal (filed from ingot) 99.9% purity, Chinese Rare Earth Information Center, Inner Mongolia, China, (viii) Ytterbium metal (filed from ingot) 99.9% purity, Chinese Rare Earth Information Center, Inner Mongolia, China, (viii) Ytterbium metal (filed from ingot) 99.9% purity, Chinese Rare Earth Information Center, Inner Mongolia, China, (x) Lanthanum

metal (filed from ingot) 99.9% purity, Chinese Rare Earth Information Center, Inner Mongolia, China, (xi) Erbium metal (filed from ingot) 99.9% purity, Chinese Rare Earth Information Center, Inner Mongolia, China, (xii) Praseodymium metal (filed from ingot) 99.9% purity, Chinese Rare Earth Information Center, Inner Mongolia, China, (xiii) Neodymium metal (filed from ingot) 99.9% purity, Chinese Rare Earth Information Center, Inner Mongolia, China, (xiv) Holmium metal (filed from ingot) 99.9% purity, Chinese Rare Earth Information Center, Inner Mongolia, China, (xv) Boron metal, 99.9% purity, typically 1 μm or less, Cerac Specialty Inorganics, Milwaukee, WI.

Furnaces:

A Lindberg Blue high-temperature, horizontal tube furnace was used with a continuous argon flow of approximately 0.1 L/min. Heating profiles for individual reactions were programmed into the accompanying Lindberg UP150 furnace controller. Thermocouples connected to the furnace controller were used to monitor furnace temperatures during reactions. The maximum operating temperature for this furnace was 1500 °C.

A radio frequency (RF) furnace was constructed from an Ameritherm XP7.5CE Induction Heater and fused quartz reaction chamber. A molybdenum cylinder, machined to act as a reaction crucible holder, was used as a susceptor. A boron nitride cylinder was machined to hold the molybdenum crucible in the center of the reaction chamber. Details on the RF furnace setup are given in the appendix of this work.

RF furnace temperatures were controlled manually using the Ameritherm control unit. Reaction temperatures were monitored using an Ircon SA Series Infrared

Thermometer. During the course of some reactions, films deposited inside the reaction

chamber would prevent the IR thermometer from accurately reporting furnace temperatures. In such circumstances, reaction temperatures were approximated based on power settings for the Ameritherm control unit and a series of calibration runs conducted by heating only the molybdenum cylinder. Temperatures greater than 1700 °C were easily reached with this furnace.

Synthesis:

Ru₇B₃, Ru₂B₃, and RuB₂: Boron and ruthenium powders were added in millimolar quantities, with B:M ratios from 0.25 to 4, to alumina crucibles and topped with 40 mmol of copper shot. The crucibles were capped individually with alumina lids and then place into rectangular alumina boats. The boats were loaded into the mullite tube of a commercial high temperature furnace preheated to 500 °C. The furnace was then heated to 1450 °C in 10 hours, held for 48 hours at that temperature, and then cooled to 1100 °C in 24 hours. Upon reaching 1100°C, the furnace was turned off, allowing the products to cool to 500 °C (a preset hold temperature for the furnace), at which time the alumina boats were removed.

β-RuB₂: Boron (10 mmol) and ruthenium (1 mmol) powders were added to an alumina crucible along with holmium (2 mmol) filings. Copper shot (40 mmol) was then added to the crucible, as was an alumina lid. The RF furnace was evacuated under vacuum and flushed with N₂. Heating was initiated with the RF furnace under dynamic vacuum. Over 30 minutes the furnace temperature was raised to 1400 °C. After holding for 30 minutes at 1400 °C, the power to the furnace was shutoff due to mechanical problems. The furnace cooled to room temperature over the course of 1 hour, at which time the reaction crucible was removed.

RERu₄B₄ (RE = Y, Ce, Sm, Dy, Yb): Boron (1–4 mmol) and ruthenium (1 mmol) powders and rare earth metal (0.5–1 mmol) filings were added to alumina crucibles. After adding copper shot (40 mmol) and alumina lids to the crucibles, the crucibles were placed in the RF furnace. The RF furnace was evacuated under vacuum and flushed with N₂. Heating was initiated with the RF furnace under dynamic vacuum. Over 30 minutes the furnace temperature was raised to 1350 °C or 1400 °C. After holding for 60 minutes at the maximum temperature, the power to the furnace was shutoff and the furnace was allowed to cool to room temperature.

RE_x(Ru₄B₄)_y (RE = Pr, Nd): Boron (3 mmol), ruthenium (1 mmol), and the rare earth metal (2.5 mmol) were added to an alumina crucible. After adding copper shot (40 mmol) and lids, the crucibles were placed in an alumina boat. The boat was loaded into the mullite tube of a commercial high temperature furnace preheated to 500 °C. The furnace was then heated to 1450 °C in 8 hours, held for 33 hours at that temperature, and then the furnace was turned off, allowing the products to cool to 500 °C (a preset hold temperature for the furnace), at which time the alumina boat was removed.

Isolation from flux:

When fully cooled to room temperature, crucibles were placed in individual baths of half-concentrated HNO₃ in order to remove the copper flux. An overnight soak was used to completely remove the copper flux, however, many crystals were removed from the flux after a 2-3 hour soak. Extended soaking in the bath was not found to damage the crystals. The crystals were filtered from the acid bath, washed with H₂O, and dried with ethanol. The well-faceted crystals were easily distinguishable from the spherical elemental ruthenium that remained in most reactions.

The products from reactions aimed at binary borides all contained unreacted elemental ruthenium, with the amount of residual ruthenium decreasing as the B:M ratio increased. The yield of Ru_7B_3 from reactions with a B:M ratio of 0.25, 0.33, 0.5, and 1.0 was between 70% and 80%, based on boron. Ru_7B_3 was found as a minor product in the reactions with B:M ratios of 2.0, 3.0, and 4.0. Ru_2B_3 was the major product from the B:M = 2.0 reaction, with an estimated yield of 60%, based on ruthenium. RuB_2 was a minor product in the B:M = 2.0 reaction, but was the major product in the B:M = 3.0 and 4.0 reactions. The yield of RuB_2 was approximately 75% in the B:M = 3.0 reaction and nearly 90% in the B:M = 4.0 reaction, based on ruthenium.

The new β -RuB₂ phase was collected in an estimated 25% yield, based on ruthenium. The ordinary RuB₂ phase was present in approximately the same ratio. The remainder of the collected product was unreacted ruthenium and boron.

The RERu₄B₄ compounds were collected in an estimated 50% yield, based on ruthenium. The side products in the reactions producing these compounds were RERuB₄, traces of REB₆ and Ru₇B₃, and elemental ruthenium. YRu₃B₂ was a minor side product in the reaction producing YRu₄B₄.

C. Physical Measurements

Energy Dispersive Spectroscopy:

Energy dispersive spectroscopy (EDS) analyses were carried out on selected crystals to determine their chemical composition. The analyses were performed with a JEOL JSM-6400 scanning electron microscope (SEM) equipped with Oxford Inca Energy Dispersive Spectroscopy (Si:Li) detector and Norvar window for standardless

quantization of elements with $Z \ge 4$. The crystals were affixed to an alumina sample holder with double-sided carbon tape. The EDS data were acquired at an accelerating voltage of 10kV with a 30 to 60 second accumulation time.

Single-Crystal X-ray Crystallography:

Single crystals were mounted on a glass fiber with super glue and their intensity data were collected on either a Bruker SMART platform CCD diffractometer, or a STOE IPDS II diffractometer using Mo K α radiation at 50 kV and 40 mA.

Individual frames of Ru_7B_3 , Ru_2B_3 , $RERu_4B_4$ (RE = Y, Ce, Sm, Yb) and $RE_x(Ru_4B_4)_y$ (RE = Pr, Nd) examined with the Bruker machine were collected with a 0.3° ω rotation. The SMART software was used for data collection, and SAINT software was used for data extraction and reduction. After applying analytical absorption corrections, structure solution and refinement were completed using direct methods and the SHELXTL suite of programs.

Samples examined with the STOE (RuB₂, and DyRu₄B₄) had individual frames collected on a 34 cm image plate with a 60 second exposure time and a 1.0° ω rotation. The X-SHAPE and X-RED-32 software packages were used for data extraction and reduction and to apply an analytical absorption correction. Direct methods and the SHELXTL suite were used to solve and refine the structures.

The crystal structure refinement data for Ru₇B₃ are found in Table 4-1.

Previously reported¹⁰ atomic parameters were used as a starting point for the refinement of the structure. The atomic positions and isotropic displacement parameters are listed in Table 4-2. Anisotropic displacement parameters for the atoms are found in Table 4-3.

Selected bond lengths in Ru₇B₃ and a count of those bonds are listed in Table 4-4.

The crystal structure refinement data for Ru₂B₃ are found in Table 4-5.

Previously reported¹¹ atomic parameters were used as a starting point for the refinement of the structure. The atomic positions and isotropic displacement parameters are listed in Table 4-6. Anisotropic displacement parameters for the atoms are found in Table 4-7.

Selected bond lengths in Ru₂B₃ and a count of those bonds are listed in Table 4-8.

The crystal structure refinement data for RuB₂ are found in Table 4-9. Previously reported³ atomic parameters were used as a starting point for the refinement of the structure. The atomic positions and isotropic displacement parameters are listed in Table 4-10. Anisotropic displacement parameters for the atoms are found in Table 4-11. Selected bond lengths in Ru₂B₃ and a count of those bonds are listed in Table 4-12.

The crystal structure refinement data for β-RuB₂ are found in Table 4-13. Atomic parameters for ReB₂¹² were used as a starting point for the refinement of the structure. The atomic positions and isotropic displacement parameters are listed in Table 4-14. Anisotropic displacement parameters for the atoms are found in Table 4-15. Selected bond lengths in Ru₂B₃ and a count of those bonds are listed in Table 4-16.

The crystal structure refinement data for YRu₄B₄ and CeRu₄B₄ are found in Table 4-17, in Table 4-18 for SmRu₄B₄ and DyRu₄B₄, and in Table 4-19 for YbRu₄B₄.

Previously reported atomic parameters for LuRu₄B₄¹³ were used as a starting point for the refinement of the structure. The atomic positions and isotropic displacement parameters are listed in Table 4-20. Anisotropic displacement parameters for the atoms are found in Table 4-21. The bond distances for RERu₄B₄ (RE = Y, Ce, Sm, Dy, Yb) are listed in Table 4-22.

Initial indexing of the single crystal data for $RE_x(Ru_4B_4)_y$ (RE = Pr, Nd): suggested that these compounds crystallized with the $LaRu_4B_4$ structure. However, during refinement, it became obvious that this suggestion was incorrect. When examining the reciprocal lattice, two distinct lattices became visible along the c-axis. One lattice corresponds to a c-axis length of 3.67 Å and the other corresponds to a length of 4.04 Å. While we found no reports of incommensurate ruthenium borides, several reports on incommensurate iron borides with similar cell (and substructure) parameters exist. Further data collection is necessary for complete structural characterization.

Table 4-1. Crystal data and structure refinement for Ru₇B₃.

Formula weight 739.92

Temperature 293(2) K

Wavelength 0.71073 Å

Crystal system Hexagonal

Space group P63mc

Unit cell dimensions a = 7.4570(11) Å $\alpha = 90^{\circ}$

b = 7.4570(11) Å $\beta = 90^{\circ}$

c = 4.7140(9) Å $\gamma = 120^{\circ}$

Volume 227.01(6) Å³

Z 2

Density (calculated) 10.825 g/cm³
Absorption coefficient 22.466 mm⁻¹

F(000) 646

Crystal size $0.052 \times 0.052 \times 0.326 \text{ mm}^3$

Theta range for data collection 3.15 to 28.23°

Index ranges $-9 \le h \le 9, -9 \le k \le 9, -6 \le l \le 6$

Reflections collected 2328

Independent reflections 226 [R(int) = 0.0316]

Completeness to theta = 28.23° 99.2 %

Refinement method Full-matrix least-squares on F²

Data / restraints / parameters 226 / 1 / 23

Goodness-of-fit on F² 1.273

Final R indices [I>2sigma(I)] R1 = 0.0116, wR2 = 0.0288

R indices (all data) R1 = 0.0116, wR2 = 0.0288

Absolute structure parameter 0.1(4)

Extinction coefficient 0.0254(8)

Largest diff. peak and hole 0.512 and -0.573 e.Å-3

R1 = $\sum ||F_o| - |F_c|| / \sum |F_o|$ and wR2 = $[\sum (|F_o|^2 - F_c|^2)^2 / \sum (wF_o|^2)^2]^{1/2}$

Table 4-2. Atomic coordinates ($x 10^4$) and equivalent isotropic displacement parameters ($\mathring{A}^2x 10^3$) for Ru₇B₃.

	х	У	Z	U(eq)
Ru(1)	3333	6667	9527(3)	6(1)
Ru(2)	1226(1)	8774(1)	7754(1)	5(1)
Ru(3)	5429(1)	4571(1)	9623(1)	7(1)
B(1)	1891(6)	8109(6)	11911(18)	9(2)

U(eq) is defined as one third of the trace of the orthogonalized Uij tensor.

Table 4-3. Anisotropic displacement parameters (Å²x 10³) for Ru₇B₃.

	Π11	U22	П33	U23	U13	U12
Ru(1)	6(1)	6(1)	6(1)	0	0	3(1)
Ru(2)	4(1)	4(1)	6(1)	0(1)	0(1)	2(1)
Ru(3)	7(1)	7(1)	7(1)	0(1)	0(1)	3(1)
B(1)	6(2)	6(2)	12(4)	1(2)	-1(2)	-1(3)

The anisotropic displacement factor exponent takes the form: $-2\pi^2$ [h^2 $a^{*2}U^{11} + ... + 2h$ k a^* b^* U^{12}]

Table 4-4. Selected bond distances (Å) for Ru₇B₃.

Rul	B1	3x	2.1756(2)
Ru2	B1	1x	2.1395(3)
Ru2	B1	2x	2.1825(2)
Ru3	B1	2x	2.1637(2)
Rul	Ru3	3x	2.7075(4)
Rul	Ru3	3x	2.8105(4)
Rul	Ru2	3x	2.8472(3)
Rul	Ru3	3x	2.8852(4)
Ru2	Ru2	2x	2.7427(4)
Ru2	Ru3	2x	2.7913(3)
Ru2	Ru2	4x	2.8395(4)
Ru2	Ru1	1x	2.8472(3)
Ru2	Ru3	2x	2.8539(4)
Ru3	Ru3	2x	2.6049(4)
Ru3	Ru1	1 x	2.7075(3)
Ru3	Ru3	2x	2.7680(4)
Ru3	Ru2	2x	2.7913(3)
Ru3	Ru1	1 x	2.8105(4)
Ru3	Ru2	2x	2.8539(4)
Ru3	Rul	1x	2.8852(4)

Table 4-5. Crystal data and structure refinement for Ru₂B₃.

Formula weight	234.57	
Temperature	293(2) K	
Wavelength	0.71073 Å	
Crystal system	Hexagonal	
Space group	P6 ₃ /mmc	
Unit cell dimensions	a = 2.9029(4) Å	α= 90°
	b = 2.9029(4) Å	β= 90°
	c = 12.814(3) Å	γ = 120°
Volume	93.51(3) Å ³	
Z	2	
Density (calculated)	8.331 g/cm ³	
Absorption coefficient	15.613 mm ⁻¹	
F(000)	206	
Crystal size	0.038 x 0.084 x 0.084 m	m ³
Theta range for data collection	3.18 to 27.76°	
Index ranges	$-3 \le h \le 3, -3 \le k \le 3, -1$	6 ≤ l ≤ 16
Reflections collected	899	
Independent reflections	65 [R(int) = 0.0327]	

Completeness to theta = 27.76° 95.4 %

Refinement method Full-matrix least-squares on F²

Data / restraints / parameters 65 / 0 / 10

Goodness-of-fit on F² 1.211

Final R indices [I>2sigma(I)] R1 = 0.0148, wR2 = 0.0353

R indices (all data) R1 = 0.0163, wR2 = 0.0366

Extinction coefficient 0.169(13)

Largest diff. peak and hole 0.751 and -0.503 e.Å-3

R1 = $\sum ||F_o| - |F_c|| / \sum |F_o|$ and wR2 = $[\sum (|F_o^2 - F_c^2|)^2 / \sum (wF_o^2)^2]^{1/2}$

Table 4-6. Atomic coordinates ($x 10^4$) and equivalent isotropic displacement parameters ($\mathring{A}^2x 10^3$) for Ru₂B₃.

	x	у	z	U(eq)
Ru(1)	6667	3333	1400(1)	3(1)
B(1)	6667	3333	9697(7)	4(2)
B(2)	6667	3333	7500	5(3)

U(eq) is defined as one third of the trace of the orthogonalized U^{ij} tensor.

Table 4-7. Anisotropic displacement parameters (Å²x 10³) for Ru₂B₃.

	Π11	U22	П33	U23	П13	U12
Ru(1)	3(1)	3(1)	1(1)	0	0	2(1)
B(1)	5(3)	5(3)	3(4)	0	0	2(1)
B(2)	5(4)	5(4)	5(6)	0	0	2(2)

The anisotropic displacement factor exponent takes the form: $-2\pi^2$ [h^2 $a^{*2}U^{11} + ... + 2h$ k a^* b^* U^{12}]

Table 4-8. Selected bond distances (Å) for Ru₂B₃.

Ru1	B1	1x	2.1821(4)
Rul	B1	3x	2.1871(3)
Rul	B2	3x	2.1901(3)
B1	B1	3x	1.8474(2)
B1	Rul	1x	2.1821(4)
B1	Ru1	3x	2.1871(3)
B2	Rul	6x	2.1901(3)

Table 4-9. Crystal data and structure refinement for RuB₂.

Formula weight 122.69 Temperature 293(2) K 0.71073 Å Wavelength Orthorhombic

Space group **Pmmn**

Crystal system

Unit cell dimensions a = 4.6322(9) Å $\alpha = 90^{\circ}$

> b = 2.8542(6) Åβ= 90°

> c = 4.0292(8) Å $\gamma = 90^{\circ}$

Volume 53.271(19) Å³

Z 2

 7.649 g/cm^3 Density (calculated)

13.716 mm⁻¹ Absorption coefficient

F(000) 108

 $0.031 \times 0.040 \times 0.048 \text{ mm}^3$ Crystal size

5.06 to 36.38° Theta range for data collection

 $-7 \le h \le 7, -4 \le k \le 4, -6 \le l \le 6$ Index ranges

Reflections collected 863

Independent reflections 165 [R(int) = 0.0595]

Completeness to theta = 36.38° 100.0 %

Full-matrix least-squares on F² Refinement method

Data / restraints / parameters 165 / 0 / 12

Goodness-of-fit on F² 1.210

Final R indices [I>2sigma(I)] R1 = 0.0157, wR2 = 0.0341R indices (all data) R1 = 0.0165, wR2 = 0.0344

Extinction coefficient 0.200(16)

1.204 and -1.141 e.Å-3 Largest diff. peak and hole

 $R1 = \sum ||F_o| - |F_c|| / \sum |F_o|$ and $wR2 = \left[\sum (|F_o|^2 - F_c|^2)^2 / \sum (wF_o|^2)^2\right]^{1/2}$

Table 4-10. Atomic coordinates ($x 10^4$) and equivalent isotropic displacement parameters ($\mathring{A}^2x 10^3$) for RuB₂.

	х	у	Z	U(eq)
Ru(1)	2500	2500	6512(1)	1(1)
B(1)	5550(8)	-2500	8615(6)	4(1)

U(eq) is defined as one third of the trace of the orthogonalized U^{ij} tensor.

Table 4-11. Anisotropic displacement parameters (Å²x 10³) for RuB₂.

	Πιι	U22	П33	U23	U13	U12
Ru(1)	1(1)	1(1)	1(1)	0	0	0
B(1)	4(1)	4(1)	3(1)	0	0(1)	0

The anisotropic displacement factor exponent takes the form: $-2\pi^2$ [h^2 $a^{*2}U^{11} + ... + 2h$ k a^* b^* U^{12}]

Table 4-12. Selected bond distances (Å) for RuB₂.

Ru1	B 1	2x	2.1612(4)
Ru1	B 1	4x	2.1796(3)
Ru1	B 1	2x	2.2547(4)
B1	B1	1x	1.8067(4)
B1	B1	2x	1.8818(3)
B1	Rul	1x	2.1612(4)
B1	Rul	2x	2.1796(3)
B1	Ru1	1x	2.2547(4)

Table 4-13. Crystal data and structure refinement for β -RuB₂.

Formula weight	122.69	
Temperature	273(2) K	
Wavelength	0.71073 Å	
Crystal system	Hexagonal	
Space group	P6 ₃ /mmc	
Unit cell dimensions	a = 2.9142(4) Å	α= 90°
	b = 2.9142(4) Å	β= 90°
	c = 7.283(2) Å	γ = 120°
Volume	53.565(19) Å ³	
Z	2	
Density (calculated)	7.607 g/cm ³	
Absorption coefficient	13.640 mm ⁻¹	
F(000)	108	
Crystal size	0.008 x 0.084 x 0.090 m	m ³
Theta range for data collection	5.60 to 27.73°	
Index ranges	$-3 \le h \le 3, -3 \le k \le 3, -9$	$\leq l \leq 9$

Reflections collected 475

Independent reflections 38 [R(int) = 0.0276]

Completeness to theta = 27.73° 94.7 %

Refinement method Full-matrix least-squares on F²

Data / restraints / parameters 38 / 0 / 7

Goodness-of-fit on F² 0.936

Final R indices [I>2sigma(I)] R1 = 0.0239, wR2 = 0.0820

R indices (all data) R1 = 0.0276, wR2 = 0.0880

Extinction coefficient 0.07(4)

Largest diff. peak and hole 0.789 and -1.243 e.Å-3

R1 = $\sum ||F_o| - |F_c|| / \sum |F_o|$ and wR2 = $[\sum (|F_o|^2 - F_c|^2)^2 / \sum (wF_o|^2)^2]^{1/2}$

Table 4-14. Atomic coordinates (x 10^4) and equivalent isotropic displacement parameters (2 X 3) for 3 RuB₂.

	х	у	Z	U(eq)
Ru(1)	3333	6667	7500	5(1)
B(2)	6667	3333	5590(30)	8(4)

U(eq) is defined as one third of the trace of the orthogonalized Uij tensor.

Table 4-15. Anisotropic displacement parameters ($Å^2x 10^3$) for β -RuB₂.

	Π11	U ²²	П33	U ²³	U13	U12
Ru(1)	4(1)	4(1)	6(1)	0	0	2(1)
B(2)	8(7)	8(7)	7(8)	0	0	4(3)

The anisotropic displacement factor exponent takes the form: $-2\pi^2$ [h^2 $a^{*2}U^{11} + ... + 2h$ k a^* b^* U^{12}]

Table 4-16. Selected bond distances (Å) for β -RuB₂.

Rul	B2	6x	2.1838(3)
Rul	B2	2x	2.2493(7)
B2	B2	3x	1.8882(2)
B2	Rul	3x	2.1838(3)
B2	Ru1	1x	2.2493(7)

Table 4-17. Crystal data and structure refinement for RERu₄B₄ (RE= Y, Ce).

		1,00).
Formula	YRu ₄ B ₄	CeRu ₄ B ₄
Formula weight	536.43	587.64
Temperature	297(2) K	297(2) K
Crystal system	Tetragonal	Tetragonal
Space group	I4 ₁ /acd	I4 ₁ /acd
Unit cell dimensions	a = 7.4525(14) Å	a = 7.4744(4) Å
	c = 14.988(6) Å	c = 15.0642(19) Å
Volume	832.4(4) Å ³	841.59(12) Å ³
Z, Density (calculated)	8, 8.560 g/cm ³	8, 9.276 g/cm ³
Absorption coefficient	27.561 mm ⁻¹	24.417 mm ⁻¹
F(000)	1880	2032
Crystal size, mm	0.050 x 0.150 x 0.150	0.028 x 0.066 x 0.066
Theta range for data collection	4.73 to 28.31°	4.71 to 28.30°
Index ranges	$-9 \le h \le 9,$	$-9 \le h \le 9,$
	$-9 \le k \le 9,$	$-9 \le k \le 9,$
	$-18 \le l \le 19$	$-19 \le l \le 18$
Reflections collected	3793	3898
Independent reflections	253 [R(int) = 0.0413]	257 [R(int) = 0.0317]
Completeness to θ_{max}	96.9 %	97.0 %
Refinement method	Full-matrix least-squar	es on F ²
Data / restraints / parameters	253 / 0 / 23	257 / 0 / 23
Goodness-of-fit on F ²	1.337	1.013
Final R indices [I>2σ(I)]	R1 = 0.0271,	R1 = 0.0185,
	wR2 = 0.1355	wR2 = 0.0599
R indices (all data)	R1 = 0.0274,	R1 = 0.0193,
	wR2 = 0.1358	wR2 = 0.0604
Extinction coefficient	0.0053(8)	0.00236(18)
Largest diff. peak & hole	2.084 & -1.244 e.Å ⁻³	1.106 & - 0.916 e.Å ⁻³

R1 = $\sum ||F_o| - |F_c|| / \sum |F_o|$ and wR2 = $[\sum (|F_o|^2 - F_c|^2)^2 / \sum (wF_o|^2)^2]^{1/2}$

Table 4-18. Crystal data and structure refinement for RERu₄B₄ (RE= Sm, Dy).

	(
Formula	SmRu₄B₄	DyRu₄B₄
Formula weight	597.87	610.02
Temperature	297(2) K	100(2) K
Crystal system	Tetragonal	Tetragonal
Space group	I4 ₁ /acd	I4 ₁ /acd
Unit cell dimensions	a = 7.4801(4) Å	a = 7.4195(10) Å
	c = 15.0375(18) Å	c = 14.930(3) Å
Volume	841.38(12) Å ³	821.9(2) Å ³
Z, Density (calculated)	8, 9.440 g/cm ³	$8, 9.860 \text{ g/cm}^3$
Absorption coefficient	27.761 mm ⁻¹	32.109 mm ⁻¹
F(000)	2064	2096
Crystal size, mm	0.050 x 0.150 x 0.150	0.070 x 0.079 x 0.080
Theta range for data collection	4.71 to 28.97°	4.75 to 36.59°
Index ranges	$-10 \le h \le 10,$	$-12 \le h \le 12$,
	$-10 \le k \le 9,$	$-9 \le k \le 12$,
	$-20 \le l \le 19$	$-24 \le 1 \le 20$
Reflections collected	4297	6128
Independent reflections	278[R(int) = 0.1325]	511 [R(int) = 0.0760]
Completeness to θ_{max}	97.5 %	99.0 %
Refinement method	Full-matrix least-squar	res on F ²
Data / restraints / parameters	278 / 0 / 23	511/0/23
Goodness-of-fit on F ²	1.202	1.317
Final R indices [I>2σ(I)]	R1 = 0.0304,	R1 = 0.0450,
	wR2 =0.0928	wR2 = 0.1397
R indices (all data)	R1 = 0.0304,	R1 = 0.0491,
	wR2 = 0.0928	wR2 = 0.1733
Extinction coefficient	0.0038(4)	0.0039(6)
Largest diff. peak & hole	2.288 & -2.497 e.Å ⁻³	6.45 8 & - 12.129 e.Å ⁻³

R1 = $\sum ||F_o| - |F_c|| / \sum |F_o|$ and wR2 = $[\sum (|F_o^2 - F_c^2|)^2 / \sum (wF_o^2)^2]^{1/2}$

Table 4-19. Crystal data and structure refinement for YbRu₄B₄.

Formula weight 620.56

Temperature 297(2) K

Wavelength 0.71073 Å

Crystal system Tetragonal

Space group I4₁/acd

Unit cell dimensions a = 7.4185(10) Å $\alpha = 90^{\circ}$

b = 7.4185(10) Å $\beta = 90^{\circ}$

c = 14.957(3) Å $\gamma = 90^{\circ}$

Volume 823.2(2) Å³

Z 8

Density (calculated) 10.015 g/cm³
Absorption coefficient 36.626 mm⁻¹

F(000) 2128

Theta range for data collection 4.75 to 29.15°

Index ranges $-10 \le h \le 9, -9 \le k \le 9, -20 \le l \le 19$

Reflections collected 4234

Independent reflections 272 [R(int) = 0.0369]

Completeness to theta = 29.15° 96.1 %

Refinement method Full-matrix least-squares on F²

Data / restraints / parameters 272 / 0 / 23

Goodness-of-fit on F² 0.945

Final R indices [I>2sigma(I)] R1 = 0.0183, wR2 = 0.0425 R indices (all data) R1 = 0.0188, wR2 = 0.0427

Extinction coefficient 0.0054(2)

Largest diff. peak and hole 0.957 and -0.969 e.Å-3

 $R1 = \sum ||F_o| - |F_c|| / \sum |F_o|$ and $wR2 = [\sum (|F_o^2 - F_c^2|)^2 / \sum (wF_o^2)^2]^{1/2}$

Table 4-20. Atomic coordinates ($x 10^4$) and equivalent isotropic displacement parameters ($Å^2x 10^3$) for RERu₄B₄ (RE = Y, Ce, Sm, Dy, Yb).

	x	y	Z	U(eq)
Y(1)	0	2500	1250	8(1)
Ru(1)	-3519(1)	3654(1)	1867(1)	6(1)
B(1)	-3329(12)	3920(13)	433(7)	9(2)
Ce(1)	0	2500	1250	4(1)
Ru(1)	-3520(1)	1355(1)	1864(1)	3(1)
B(1)	-3533(11)	4174(10)	2068(6)	5(1)
Sm(1)	0	2500	1250	2(1)
Ru(1)	3844(1)	1033(1)	633(1)	2(1)
B(1)	1675(14)	-1058(13)	438(8)	3(2)
Dy(1)	0	2500	1250	5(1)
Ru(1)	3846(1)	3982(1)	632(1)	4(1)
B(1)	6662(15)	3889(15)	425(8)	4(2)
Yb(1)	0	2500	1250	3(1)
Ru(1)	3504(1)	1347(1)	1868(1)	2(1)
B(1)	1410(10)	836(11)	2941(6)	4(1)

U(eq) is defined as one third of the trace of the orthogonalized U^{ij} tensor.

Table 4-21. Anisotropic displacement parameters ($^{A}2x 10^{3}$) for RERu₄B₄ (RE = Y, Ce, Sm, Dy, Yb).

	U11	U ²²	U33	U23	U13	U12
Y(1)	8(1)	8(1)	8(1)	0	0	2(1)
Ru(1)	5(1)	6(1)	6(1)	0(1)	-1(1)	0(1)
B(1)	0(4)	18(5)	9(4)	13(3)	-8(4)	4(3)
Ce(1)	4(1)	4(1)	3(1)	0	0	-1(1)
Ru(1)	4(1)	3(1)	2(1)	0(1)	-1(1)	0(1)
B(1)	9(4)	1(3)	3(3)	0(3)	-10(3)	1(3)
Sm(1)	3(1)	3(1)	0(1)	0	0	0(1)
Ru(1)	3(1)	3(1)	1(1)	-1(1)	0(1)	0(1)
B(1)	3(4)	5(4)	1(3)	6(3)	-1(3)	1(3)
Dy(1)	3(1)	3(1)	7(1)	0	0	1(1)
Ru(1)	3(1)	3(1)	5(1)	0(1)	0(1)	0(1)
B(1)	5(4)	7(4)	0(4)	8(3)	3(3)	2(3)
Yb(1)	4(1)	4(1)	3(1)	0	0	1(1)
Ru(1)	3(1)	2(1)	1(1)	0(1)	1(1)	0(1)
B(1)	4(3)	3(3)	5(3)	3(3)	4(3)	-4(3)

The anisotropic displacement factor exponent takes the form: $-2\pi^2$ [h^2 $a^{*2}U^{11} + ... + 2h$ k a^* b^* U^{12}]

Table 4-22. Bond distances (Å) for RERu₄B₄ (RE = Y, Ce, Sm, Dy, Yb).

	YRu ₄ B ₄	CeRu ₄ B ₄	SmRu ₄ B ₄	DyRu ₄ B ₄	YbRu ₄ B ₄
RE-Ru	2.9109(9)	2.9170(6)	2.9315(7)	2.8981(9)	2.8884(9)
RE-B	2.962(7)	2.983(7)	2.973(10)	2.952(11)	2.9467(9)
	3.006(10)	3.031(9)	3.029(12)	2.972(13)	3.0025(9)
Ru-B	2.127(10)	2.130(8)	2.138(10)	2.114(11)	2.1102(9)
	2.163(11)	2.176(9)	2.165(12)	2.165(11)	2.1462(9)
	2.216(10)	2.258(8)	2.229(10)	2.185(11)	2.2075(9)
	2.273(10)	2.259(8)	2.273(11)	2.265(10)	2.2622(9)
	2.269(10)	2.259(8)	2.279(11)	2.284(13)	2.2655(9)
Ru–Ru	2.7089(11)	2.7087(9)	2.7103(11)	2.6989(14)	2.7100(9)
	2.7612(13)	2.7879(11)	2.7687(14)	2.7484(16)	2.7511(9)
	2.7979(12)	2.7980(10)	2.7943(13)	2.7869(15)	2.8024(9)
	2.9770(14)	2.9876(11)	2.9316(7)	2.8981(9)	2.9529(9)
	3.1047(12)	3.1178(10)	3.1246(13)	3.0910(16)	3.0824(9)
В-В	1.79(2)	1.793(18)	1.81(2)	1.78(2)	1.810(10)

D. Structural Description

Ru₇B₃: The structure of Ru₇B₃ (Figure 4-1a) comprises ruthenium tetrahedra and octahedra and isolated boron atoms. ¹⁰ The structure can also be described with a more complex building unit known as a stellaquadrangula. ¹⁷ The stellaquadrangula (Figure 4-1b) comprises a central tetrahedron sharing each face with another capping tetrahedron. The central tetrahedron in the stellaquadrangula has a corner pointing into the page, and the fourth capping tetrahedron has a corner coming out of the page. In Ru₇B₃, the stellaquadrangula share corners with the octahedra to form a 3-D network of ruthenium atoms. The boron atoms reside in cavities in the framework.

Ru₂B₃: A structural description of Ru₂B₃ was first reported in 1962. The structure (Figurer 4-2a) is made of alternating metal and boron atom layers. The metal atoms are hexagonally close-packed. The boron atoms form two distinct layers, one with puckered hexagonal rings (Figure 4-2b), and the other with a hexagonally packed layer of non-bonding atoms (Figure 4-2c). The structure is quite different from the Cr₂B₃ structure reported in Chapter 2. In the Ru₂B₃ structure, the boron atoms form 2-D networks instead of the triple chains seen in Cr₂B₃ and expected based on the B:M ratio of 1.5. A previous report¹⁸ on Ru₂B₃ suggests that the larger ruthenium atoms would force unreasonably short boron-boron bonds should the compound crystallize with the Cr₂B₃ structure. The puckered layers in Ru₂B₃ distance the boron atoms from each other sufficiently.

RuB₂: The structure of RuB₂, first reported in 1962,³ contains corrugated layers of boron atoms (Figure 4-3a). The corrugated boron rings are limited to RuB₂ and OsB₂ among diborides. The ruthenium atoms in the structure appear to be two separate layers,

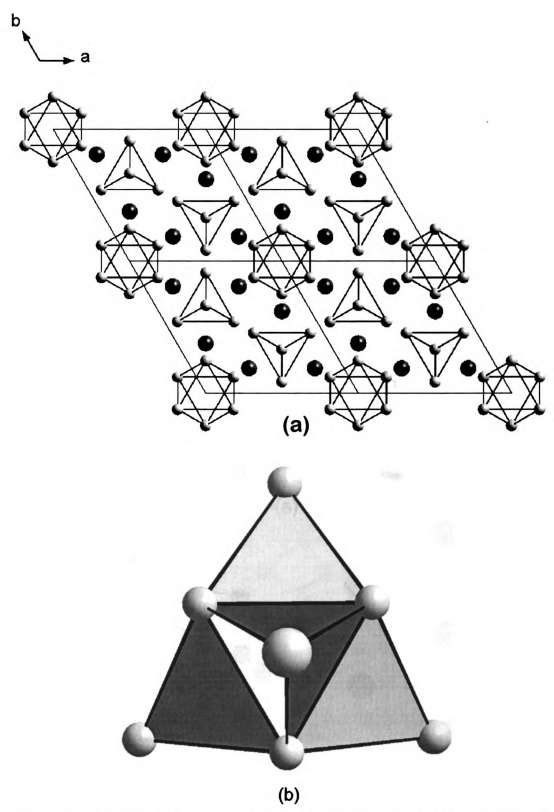


Figure 4-1. (a) Structure of Ru₇B₃ and (b) the stellaquadrangula building unit.

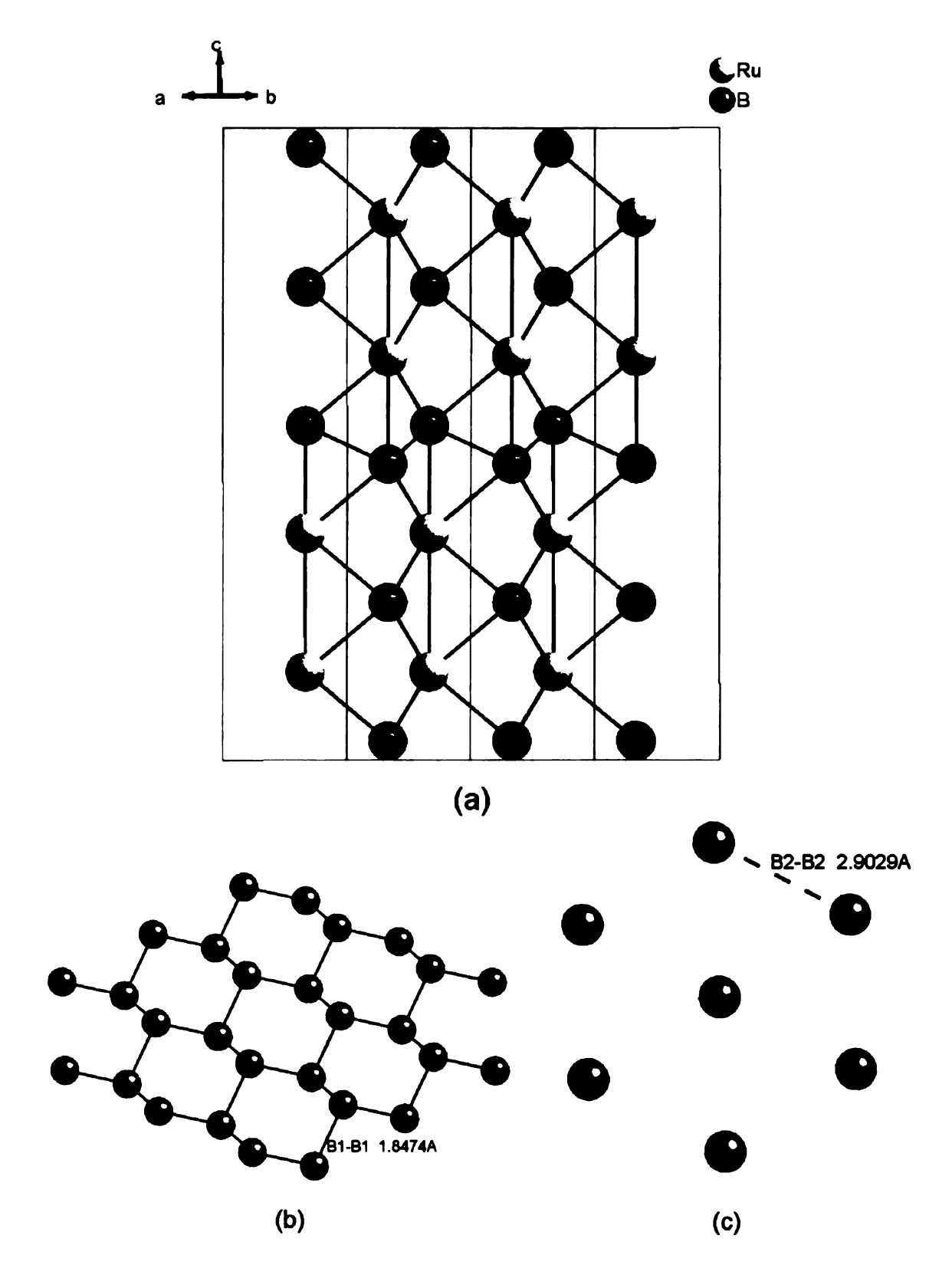


Figure 4-2. (a) Structure of Ru_2B_3 and the (b) puckered boron layer and (c) planar layer of boron atoms.

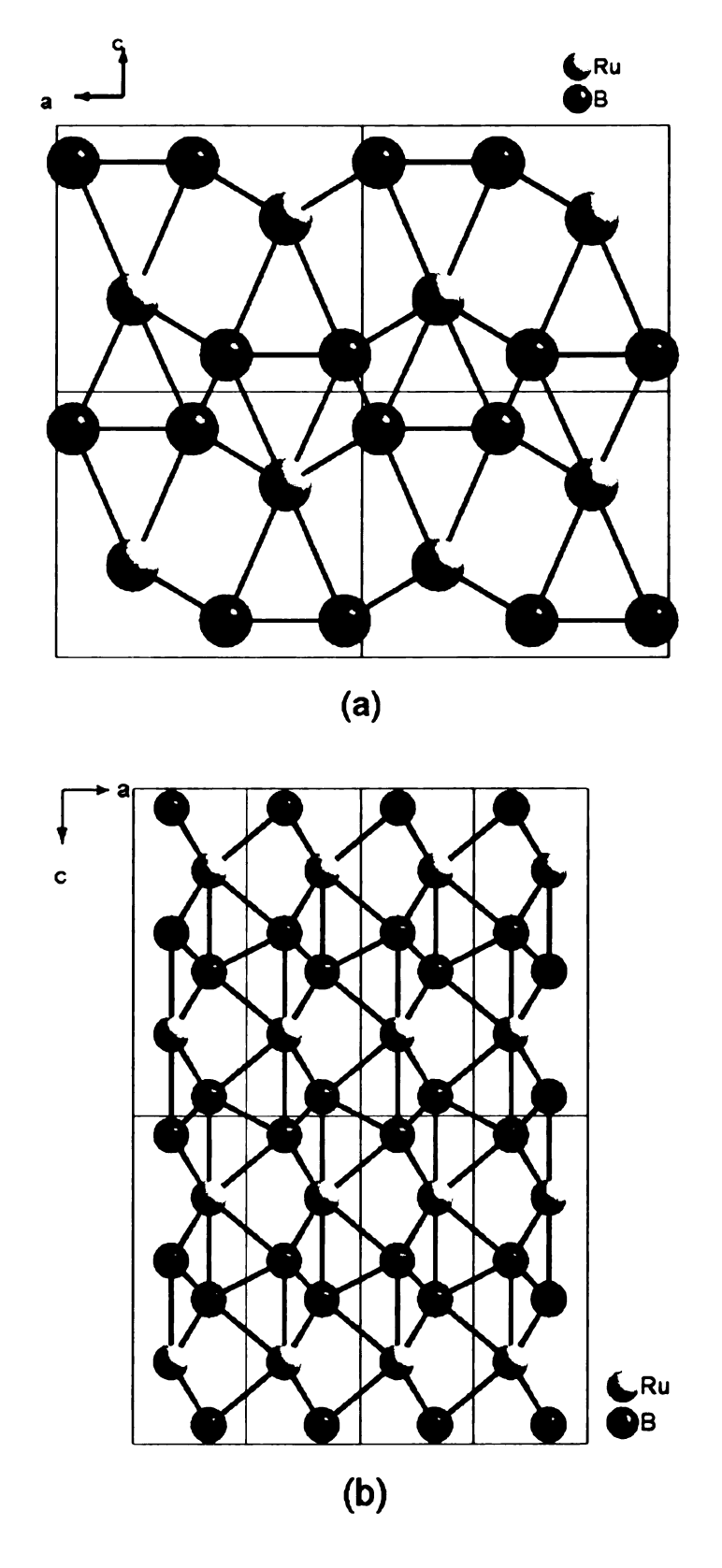


Figure 4-3. Structure of RuB_2 crystallizing with the (a) RuB_2 -type and (b) ReB_2 -type structures.

as they alternately center boron rings above and below one metal atom layer. Recent quantum mechanical studies suggest that the corrugated layers are a result of limited electron donation from the ruthenium atoms to the boron layers.⁷

β-RuB₂: This phase of RuB₂ crystallizes in the ReB₂-structure type¹² described in Chapter 3. In this newly discovered phase, the boron atoms are in puckered hexagonal rings, with the "chair" conformation. In the known RuB₂, the layers are more corrugated, with the boron atoms sitting in the "boat" conformation of a hexagonal ring. β-RuB₂, shown in Figure 4-3b, crystallizes in the hexagonal space group P6₃/mmc, rather than the orthorhombic Pmmn space group of the known RuB₂.

RERu₄B₄ (RE= Y, Ce, Sm, Dy, Yb): All of these compounds crystallize in the LuRu₄B₄ structure type¹³ (Figure 4-4). The ruthenium atoms in these compounds form tetrahedra that bond to each other in a zigzag fashion. A distorted NaCl lattice is formed as the centers of the ruthenium tetrahedra reside on the anion sites and the rare earth atoms reside on the cation sites. Boron atoms are found in pairs throughout the voids of this distorted face-centered cubic lattice.

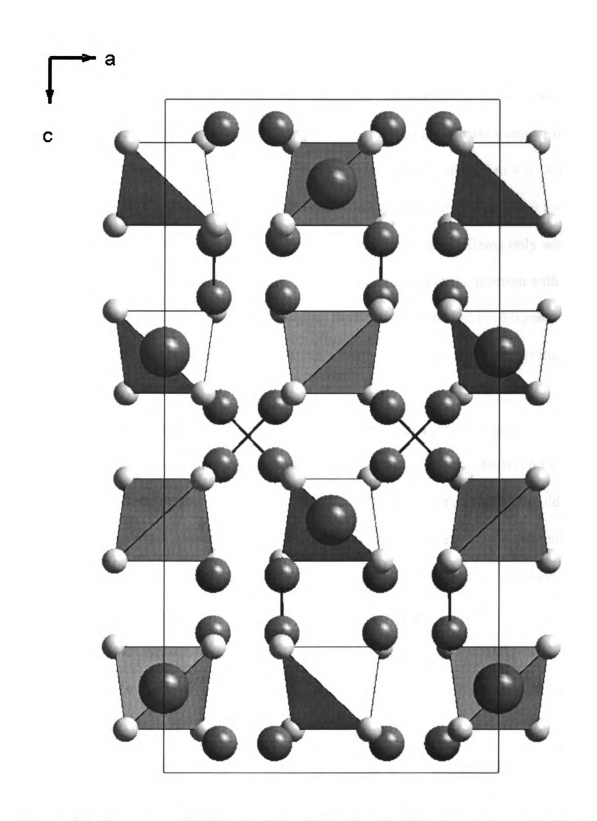


Figure 4-4. Structure of RERu₄B₄ (RE = Y, Ce, Sm, Dy, Yb) shown down the b-axis.

E. Results and Discussion

After initially synthesizing RuB₂ from a copper flux reaction in the RF furnace, we decided to do a study on the ruthenium borides that would grow from a copper flux at varying B:Ru ratios. Seven reactions with varying B:Ru ratios from 0.25 to 4.0. Ru₇B₃ crystallized from all metal rich reactions and traces of the compound were still found in reactions with B:Ru ratios up to 2.0. Ru₂B₃ was more limited, crystallizing only when the B:Ru ratio was 2.0. Crystals of RuB₂ were found beginning in the reaction with a B:Ru ratio of 2.0 and became the major product for B:M = 3.0 and B:M = 4.0 reactions. Elemental ruthenium was found in all products, though the amount decreased as the B:Ru ratio increased.

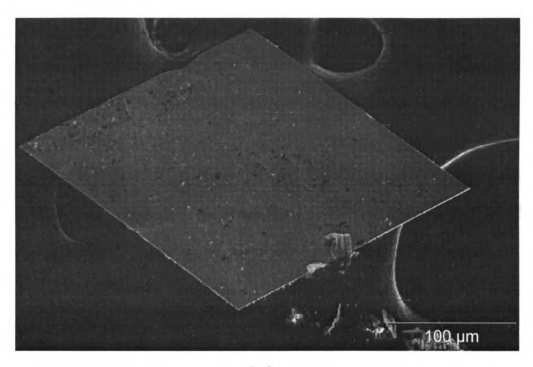
Surprisingly, no Ru₁₁B₈ or RuB_{1.1} crystals were found during the study.

Reactions targeted specifically at these reported phases yielded mostly Ru₇B₃ and Ru₂B₃.

Further research using more varied B:Ru ratios and different heating profiles should be conducted before the flux synthesis of more ruthenium boride phases can be discounted.

To see further varying of B:M ratios is necessary, we need only look at the synthesis of β-RuB₂. Our study on binary ruthenium borides would have produced this phase had we extended the B:Ru ratio to 10.0.

The initial synthesis of β-RuB₂ was quite unexpected, as the reaction was aimed at producing an analog to the Th₂MB₁₀ phases found by the Jeitschko group.¹⁹ Finding that RuB₂ can crystallize with the ReB₂ structure should not be quite as surprising. There are a couple of reports of molybdenum- and tungsten-substituted RuB₂ and OsB₂ crystallizing in the ReB₂ structure.^{20,21} Despite several reports on the stability of the RuB₂ structure versus the AlB₂-type structure,^{5,7} we found no reports comparing the



(a)

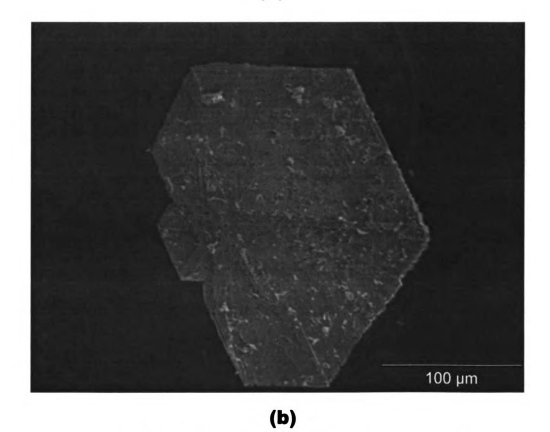
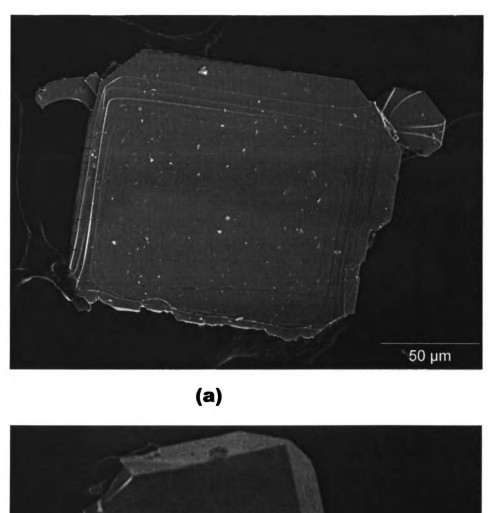


Figure 4-5. SEM micrographs of (a) RuB_2 and (b) β - RuB_2 .

RuB₂ and ReB₂ structures. It would be interesting to conduct a study on both RuB₂ phases to see if the structure really depends on how many electrons the ruthenium atoms donate to the boron layers. Crystals of RuB₂ and β -RuB₂ are shown in Figures 4-5a and 4-5b, respectively.

Synthesis of the RERu₄B₄ compounds was fairly easy for most rare earths with the aid of the flux. In addition to the compounds reported here, LaRu₄B₄ and ErRu₄B₄ were also synthesized. Most reactions containing a rare earth metal, ruthenium and boron, regardless of the stoichiometry, would produce a RERu₄B₄ compound. Unfortunately, RERuB₄ compounds also crystallized along with the RERu₄B₄ compounds, sometimes with very similar crystal morphology. Figure 4-6 clearly displays the similar morphology of CeRu₄B₄ and CeRuB₄ crystals.

The synthesis of incommensurate ruthenium borides was very interesting. The previous report on LuRu₄B₄ compounds¹³ did not mention any problems in synthesizing Pr or Nd members of the series. Because we were able to synthesize the Ce member of the series, we feel the size of the rare earth should not be a factor in determining whether or not the structure is incommensurate. Heating profiles do seem to play a decisive role in determining which phase is produced. The reaction temperature producing incommensurate phases was at least 50°C greater than in reactions producing the commensurate phases. The reaction time for the reactions yielding incommensurate phases was also quite extended when compared to the reaction times for reactions yielding the commensurate phases. It should be noted, however, that reactions at lower temperatures and run for a shorter duration failed to produce any ternary borides for either Pr or Nd.



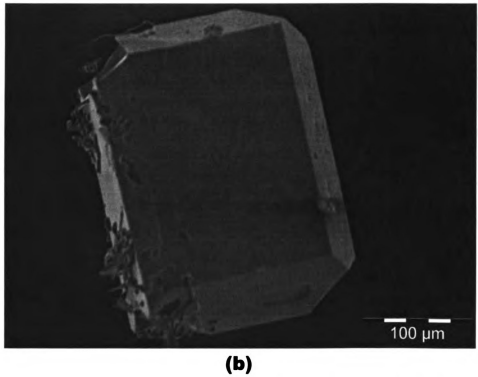


Figure 4-6. SEM micrographs of (a) CeRu₄B₄ and (b) CeRuB₄.

F. Conclusions

Presented here are the details of the copper flux synthesis and crystallographic studies on single crystals of the known binary ruthenium borides Ru₇B₃, Ru₂B₃, and RuB₂. A new binary phase, β-RuB₂, was synthesized and crystals of the compound were grown from a copper flux. The crystallographic data and atomic positions for β-RuB₂ are reported here for the first time. We successfully targeted and synthesized YRu₄B₄, CeRu₄B₄, SmRu₄B₄, DyRu₄B₄, and YbRu₄B₄. Single crystals of these compounds, all known compounds of the LuRu₄B₄-structure type, were grown from a copper flux. The first report of incommensurate ternary ruthenium borides is also presented here.

We have learned that varying reaction parameters can have quite an effect on compounds isolated from the flux. For instance, by increasing the B:Ru ratio to 10.0 a new phase of ruthenium diboride, β-RuB₂ was isolated. Additionally, increased flux reaction temperatures also play a role in the formation of incommensurate phases of PrRu₄B₄ and NdRu₄B₄. Further investigations into the synthesis adjustments that create these variations should be able to pinpoint a stronger cause and effect relationship to the molten flux synthesis techniques.

References

- 1. Nagamatsu, J.; Nakagawa, N.; Muranaka, T.; Zenitani, Y.; Akimitsu, J., Superconductivity at 39K in Magnesium Diboride. *Nature* **2001**, 410, 63-64.
- 2. Cumberland, R. W.; Weinberger, M. B.; Gilman, J. J.; Clark, S. M.; Tolbert, S. H.; Kaner, R. B., Osmium Diboride, An Ultra-Incompressible, Hard Material. *Journal of the American Chemical Society* **2005**, 127, 7264-7265.
- 3. Roof, R. B.; Kemper, C. P., New Orthorhombic Phase in the Ru-B and Os-B Systems. *Journal of Chemical Physics* **1962**, 37, (7), 1473-1476.
- 4. Vandenberg, J. M.; Matthias, B. T.; Corenzwit, E.; Barz, H., Superconductivity of Some Binary and Ternary Transition-Metal Borides. *Materials Research Bulletin* 1975, 10, 889-894.
- 5. Ivanovskii, A. L.; Medvedeva, N. I., Electronic Structure and Energies of Interatomic Interactions in Technetium, Rhenium, Ruthenium, and Osmium Diborides. *Russian Journal od Inorganic Chemistry* 1999, 44, (10), 1633-1641.
- 6. Chiodo, S.; Gotsis, H. J.; Russo, N.; Sicilia, E., OsB₂ and RuB₂, ultra-incompressible, hard materials: First-principles electronic structure calculations. *Chemical Physics Letters* **2006**, 425, 311-314.
- 7. Pallas, A.; Larsson, K., Structure Determination of the 4d Metal Diborides: A Quantum Mechanical Study. *Journal of Physical Chemistry B* **2006**, 110, 5367-5371.
- 8. Chapnik, I. M., On the Possibility of Semiconducting Properties in Diborides ReB₂, TcB₂, OsB₂, and RuB₂. *Physica Status Solidi* **1977**, A41, K71-K73.
- 9. Shishido, T.; Ye, J.; Sasaki, T.; Note, R.; Obara, K.; Takahashi, T.; Matsumoto, T.; Fukuda, T., Growth of Single Crystals in the Systems with R-Rh-B and r-Rh-B-C (R= Rare Earth Element) from Molten Copper Flux. *Journal of Solid State Chemistry* 1997, 133, 82-87.
- 10. Aronsson, B., The Crystal Structure of Ru₇B₃. Acta Chemica Scandinavica 1959, 13, 109-114.
- 11. Lundström, T., The Structure of Ru₂B₃ and WB_{2.0}, as determined by single-crystal diffractometry, and some notes on the W-B system. Arkiv för Kemi 1969, 30, 115-127.
- 12. Placa, S. L.; Post, B., The Crystal Structure of Rhenium Diboride. *Acta Crystallographica* **1962**, 15, 97-99.
- 13. Johnston, D. C., Superconductivity in a New ternary Structure Class of Boride Compounds. *Solid State Communications* 1977, 24, 699-702.

- 14. Grüttner, A.; Yvon, K., Lanthanum Ruthenium Boride, LaRu₄B₄. Acta Crystallographica 1979, B35, 451-453.
- 15. Bezinge, A.; Yvon, K.; Braun, H. F.; Muller, J.; Nissen, H.-U., Nd_{1+ε}Fe₄B₄: A composition-modulated compound with incommensurate composite crystal structure. *Physical Review B* **1987**, 36, (3), 1406-1414.
- 16. Gubich, I. B.; Zavalii, P. Y.; Kuz'ma, Y. B., Ho₂₀(Fe₄B₄)₁₇ Boride- A New Representative of Disproportionate Structures. *Inorganic Materials* **1993**, 29, (2), 301-303.
- 17. Nyman, H.; Andersson, S., The Stella Quadrangula as a Structure Building Unit. Acta Crystallographica 1979, A35, 934-937.
- 18. Aronsson, B., The Crystal Structure of RuB₂, OsB₂, and IrB_{1.35} and Some General Comments on the Crystal Shemistry of Borides in the Composition Range MeB-MeB₃. *Acta Chemica Scandinavica* **1963**, 17, 2036-2050.
- 19. Konrad, T.; Jeitschko, W., The Thorium transition Metal Borides Th_2TB_{10} (T = Fe, Co, Ni) with a Structure Very Similar to that of CaB_6 . Zeitschrift für Naturforschung 1995, 50b, 1195-1199.
- 20. Rogl, P.; Nowotny, H.; Benesovsky, F., Komplexboride mit ReB₂-Struktur. *Monatshefte für Chemie* **1970**, 101, 27-31.
- 21. Rogl, P.; Rudy, E., New Complex Borides with ReB₂- and Mo₂IrB₂-type Structure. *Journal of Solid State Chemistry* **1978**, 24, 175-181.

Chapter Five

Gallium-Rich Gallides Isolated as By-Products from Molten Flux Reactions Containing Boron

A. Introduction

One of the main obstacles to overcome in the molten flux technique is the formation of binary phases containing one reagent and the flux metal.^{1,2} These binaries are often so stable that it is nearly impossible to form the intended products. During the course of our research on synthesizing borides from a metal flux we frequently encountered this problem due to the limited solubility of boron in the flux metals. The other reagents in the reaction would react with the flux metal before boron had a chance to dissolve in the flux. This was especially true when gallium was used as the flux metal.

We have had a good deal of success in synthesizing borides from a gallium flux, producing Cr₂B₃, CrB₂, MoB, WB, MnB, MnB₄, ReB₂, and HoMnB₄. However, even in reactions producing these borides, gallides were a side product, if not the main product. Many of the gallides we have encountered throughout our research, such as V₂Ga₅, MGa₄ (M = Cr, Mn), MGa₃ (M = Fe, Co, Ru), and Ni₂Ga₃, have been known for some time and have been well studied. Given the amount of research done on gallium systems, we were fairly surprised to find several binary gallides that had little, if any structural characterization. In this chapter we will discuss the synthesis, single crystal growth, and

characterization of gallium-rich compounds from the Mn-Ga, Re-Ga, and Ni-Ga systems.

B. Experimental

Reagents:

All reagents were used as received without further purification: (i) Boron metal, 99% purity, -325 mesh, Cerac Specialty Inorganics, Milwaukee, WI, (ii) Rhenium powder, 99.99% purity, Strem Chemicals, Newburyport, MA, (iii) Manganese powder, 99.9% purity, -50 mesh, Aldrich Chemical Company, Milwaukee, WI, (iv) Gallium 3-5 mm shot, 99.999% purity, Plasmaterials, Livermore, CA, (v) Tungsten metal, 99.9% purity, Cerac Specialty Inorganics, Milwaukee, WI, (vi) Nickel metal powder, 98-99% purity, -325 mesh, E.H. Sargent & Company.

Furnaces:

Commercial tube furnaces from Applied Test Systems, Inc. were used to heat reactions sealed in quartz tubes. Furnace controllers from the Omega Company were used to program heating profiles for individual reactions. Furnace temperatures were monitored during reactions by thermocouples connected to the Omega controllers. To extend the life of the furnaces, the operating temperature for prolonged heating was limited to 1000 °C.

Synthesis and Isolation:

MnGa_{4.65}: Boron and manganese powder were mixed and added to alumina crucibles in millimolar quantities in boron-to-manganese ratios between 2:1 and 5:1. Pieces of gallium shot totaling between 1.5 g and 2.5 g were then placed in the crucibles. The alumina crucibles were then placed in 13 mm diameter quartz tubes and evacuated

under vacuum to a pressure near 10⁻⁴ Torr. The quartz tubes were then sealed using an oxygen-acetylene torch. The quartz tubes were placed in mullite tubes, then heated in commercial tube furnaces under heating profiles that increased the furnace temperature to 1000 °C in 10 hours, held the temperature constant for 48 hours, allowed the furnace to cool to 850 °C in 5 hours, held the temperature constant for an additional 48 hours, and then allowed the furnace to cool to room temperature in 60 hours.

After cooling, the quartz tubes were opened and the alumina crucibles were placed in a half-concentrated HCl bath in order to remove the excess gallium. Most of the gallium was removed after an overnight soak, but longer soaks were used without damage to the recovered product. Silver, octahedral crystals were recovered in 50-60% yields, based on manganese. Elemental analysis performed by Energy Dispersive Spectroscopy (EDS) using a Scanning Electron Microscope (SEM) showed that manganese and gallium were the only elements present in the crystals. MnB₄ and MnGa₄ were side products in these reactions. Elemental boron also remained in the collected products

ReGa_{4.5}: Boron and rhenium powder were mixed and added to alumina crucibles in millimolar quantities in boron-to-rhenium ratios between 2:1 and 5:1. Pieces of gallium shot totaling between 1.5 g and 2.5 g were then placed in the crucibles. The alumina crucibles were then placed in 13 mm diameter quartz tubes and evacuated under vacuum to a pressure near 10⁻⁴ Torr. The quartz tubes were then sealed using an oxygen-acetylene torch. The quartz tubes were placed in mullite tubes and then heated in commercial tube furnaces under heating profiles that increased the furnace temperature to 1000 °C in 10 hours, held the temperature constant for 48 hours, allowed the furnace to

cool to 850 °C in 5 hours, held the temperature constant for an additional 48 hours, and then allowed the furnace to cool to room temperature in 60 hours.

After cooling, the quartz tubes were opened and the alumina crucibles were placed in a half-concentrated HCl bath in order to remove the excess gallium. Most of the gallium was removed after an overnight soak, but longer soaks were used without damage to the recovered product. Silvery, octahedral crystals were recovered in 50-60% yields. Elemental analysis performed by EDS using an SEM showed that rhenium and gallium were the only elements present in the crystals. ReB₂ was a side product in these reactions.

Ni_{0.57}Ga_{4.43}: Boron (7.5 mmol), nickel (0.5 mmol), and tungsten (1 mmol) powders were mixed and added to an alumina crucible along with pieces of gallium shot totaling 1.45 g. A quartz filter was placed in the crucible which was then placed in a 13 mm diameter quartz tube, evacuated under vacuum to a pressure near 10⁻⁴ Torr, and sealed using an oxygen-acetylene torch. The tube was then heated in a commercial tube furnace under a heating profile that increased the furnace temperature to 1000 °C in 10 hours, held the temperature constant for 48 hours, allowed the furnace to cool to 850 °C in 5 hours, held the temperature constant for an additional 48 hours, and then allowed the furnace to cool to 250 °C in 60 hours.

The quartz tube was removed from the furnace at 250 °C and centrifuged to remove excess gallium. After centrifugation, the tube was opened and the crucible was placed in a bath of 5M I₂ in DMF in order to remove the remaining gallium flux. An overnight soak was found to be insufficient for removing all of the gallium, so soaking was continued for an additional 2 days. A subsequent investigation still found remaining gallium, so an overnight soak in half-concentrated HCl was used to finally remove all

gallium. Silver, rectangular prisms are a minor product (10-20% yield). Ni₂Ga₃ and WB were side products in this reaction. Elemental boron was also present in the collected product.

C. Physical Measurements

Energy Dispersive Spectroscopy: Energy dispersive spectroscopy (EDS) analyses were carried out on selected crystals to determine their chemical composition. The analyses were performed with a JEOL JSM-6400 scanning electron microscope (SEM) equipped with Noran Vantage Energy Dispersive Spectroscopy (Si:Li) detector and Norvar window for standardless quantization of elements with $Z \ge 4$. The crystals were affixed to an alumina sample holder with double-sided carbon tape. The EDS data were acquired at an accelerating voltage of 10 kV with a 30 to 60 second accumulation time.

Single-Crystal X-ray Crystallography: Single crystals were mounted on a glass fiber with super glue and their intensity data were collected on either a Bruker SMART platform CCD diffractometer, or a STOE IPDS II diffractometer using Mo Kα radiation at 50 kV and 40 mA.

Samples examined with the STOE (MnGa_{4.65} and ReGa_{4.5}) had individual frames collected on a 34 cm image plate with a 60 second exposure time and a 1.0° ω rotation. The X-SHAPE and X-RED-32 software packages^{7,8} were used for data extraction and reduction and to apply an analytical absorption correction. Direct methods and the SHELXTL suite were used to solve and refine the structures.

Individual frames of $Ni_{0.57}Ga_{4.43}$ examined with the Bruker machine were collected with a 0.3° ω rotation. The SMART software was used for data collection, and SAINT software⁹ was used for data extraction and reduction. After applying analytical absorption corrections, structure solution and refinement were completed using direct methods and the SHELXTL suite of programs.¹⁰

Previous reports^{11, 12} suggested that the space group for MnGa₆ was either Ccc2 or Cccm. The value of |E²-1| was 0.863 for MnGa_{4.65} and 0.972 for ReGa_{4.5}, indicating a centrosymmetric structure, so Cccm was chosen. During initial indexing of the cell we noticed weaker satellite reflections in the reciprocal lattice, as described previously by another group.¹¹ We have not yet attempted to include these satellites for a solution of the supercell structure.

During refinement we encountered a problem in placing gallium atom Ga5. The most stable position for the atom leads to Ga—Ga bonds of unacceptably short lengths (1.58 Å). The occupancy of the Ga5 atom was refined to nearly 50%, making the short "bond" distance more acceptable. The real atom is assumed to be in one of the Ga5 locations in half of the structure, and in the other site in the remaining half of the structure. Despite these adjustments, the anisotropic displacement parameters for Ga5 are quite large. Gallium atom Ga4 also has large anisotropic thermal parameters, but these are most likely a result of the problems with Ga5. The crystal structure refinement data for MnGa4.65 and ReGa4.5 are listed in Table 5-1. The atomic positions and isotropic displacement parameters are listed in Table 5-2. Anisotropic displacement parameters for the atoms are listed in Table 5-3. Bonding distances for MnGa4.65 and ReGa4.5 are listed in Table 5-4.

The crystal structure solution and refinement for Ni_{0.57}Ga_{4.43} were based on parameters from a previous structural report from powder diffraction data.¹³ The refinement data for our study are listed in Table 5-5. During refinement we found that the Ni1 site had a mixed occupancy of nickel and gallium atoms. Occupancy refinements on this crystal showed the site contained 57% nickel, though results likely vary from crystal to crystal. Atomic parameters and isotropic displacement parameters are listed in Table 5-6. Anisotropic refinement was performed on the non-mixed sites, and the results are listed in Table 5-7. Bonding distances for Ni_{0.57}Ga_{4.43} are listed in Table 5-8.

Table 5-1. Crystal data and structure refinement for MnGa $_{4.65}$ and ReGa $_{4.5}$.

Formula	MnGa _{4.65}	ReGa _{4.5}			
Formula weight	368.68	499.94			
Crystal system	Orthorhombic	Orthorhombic			
Space group	Cccm				
Unit cell dimensions	a = 8.8323(18) Å	a = 9.0077(18) Å			
	b = 8.9523(18) Å	b = 9.0618(18) Å			
	c = 9.939(2) Å	c = 10.158(2) Å			
Volume	785.8(3) Å ³	829.2(3) Å ³			
Z, Density (calculated)	8, 6.232 g/cm ³	8, 8.009 g/cm ³			
Absorption coefficient	33.309 mm ⁻¹	57.695 mm ⁻¹			
F(000)	1316	1716			
Crystal size, mm	0.144 x 0.179 x 0.185	0.157 x 0.164 x 0.260			
Theta range for data collection	3.83 to 34.54°	4.50 to 36.00°			
Index ranges	$0 \le h \le 14,$	$0 \le h \le 14,$			
	$0 \le k \le 14,$	$0 \le k \le 14,$			
	$0 \le l \le 15$	$0 \le l \le 16$			
Reflections collected	5655	3898			
Independent reflections	875[R(int) = 0.2593]	1027[R(int) = 0.1536]			
Completeness to θ_{max}	99.4 %	99.2 %			
Refinement method	Full-matrix least-squar	es on F ²			
Data / restraints / parameters	875 / 0 / 35	1027 / 0 / 35			
Goodness-of-fit on F ²	1.068	1.079			
Final R indices [I>2σ(I)]	R1 = 0.1020,	R1 = 0.0825,			
	wR2 = 0.1590	wR2 = 0.1866			
R indices (all data)	R1 = 0.0274,	R1 = 0.1451,			
	wR2 = 0.1358	wR2 = 0.2032			
Extinction coefficient	0.0026(9)	0.0022(3)			

R1 = $\sum ||F_o| - |F_c|| / \sum |F_o|$ and wR2 = $[\sum (|F_o^2 - F_c^2|)^2 / \sum (wF_o^2)^2]^{1/2}$

Table 5-2. Atomic coordinates $(x \ 10^4)$ and equivalent isotropic displacement parameters $(\mathring{A}^2x \ 10^3)$ for MnGa_{4.65} and ReGa_{4.5}.

	x	y	Z	U(eq)	Occupancy
Mn(1)	2500	2500	3458(3)	4(1)	
Ga(1)	1164(4)	4293(4)	5000	12(1)	
Ga(2)	711(4)	1150(4)	5000	14(1)	
Ga(3)	2407(4)	0	2500	14(1)	
Ga(4)	0	2588(5)	2500	50(2)	
Ga(5)	2500	2500	817(11)	48(3)	0.65
Re(1)	2500	2500	3461(1)	9(1)	
Ga(1)	1187(5)	4369(4)	5000	15(1)	
Ga(2)	623(5)	1182(5)	5000	18(1)	
Ga(3)	2383(5)	0	2500	20(1)	
Ga(4)	0	2607(6)	2500	33(1)	
Ga(5)	2500	2500	751(7)	33(2)	0.50

U(eq) is defined as one third of the trace of the orthogonalized U^{ij} tensor.

Table 5-3. Anisotropic displacement parameters (Å²x 10³) for MnGa_{4.65} and ReGa_{4.5}.

	U11	U ²²	U33	U ²³	U13	U12
Mn(1)	7(1)	2(1)	3(1)	0	0	-1(1)
Ga(1)	12(1)	13(1)	10(1)	0	0	10(1)
Ga(2)	12(1)	16(1)	15(2)	0	0	-11(1)
Ga(3)	16(1)	8(1)	17(1)	-10(1)	0	0
Ga(4)	56(3)	22(2)	71(4)	0	-57(3)	0
Ga(5)	99(9)	18(4)	28(5)	0	0	-16(5)
Re(1)	17(1)	8(1)	3(1)	0	0	-1(1)
Ga(1)	16(2)	12(2)	16(2)	0	0	8(1)
Ga(2)	18(2)	16(2)	19(2)	0	0	-9(2)
Ga(3)	24(2)	15(1)	21(1)	-11(1)	0	0
Ga(4)	42(2)	21(2)	35(2)	0	-28(2)	0
Ga(5)	60(7)	29(5)	9(3)	0	0	-8(6)

The anisotropic displacement factor exponent takes the form: $-2\pi^2$ [h^2 $a^{*2}U^{11} + ... + 2h$ k a^* b^* U^{12}]

Table 5-4. Bond distances (Å) for MnGa_{4.65} and ReGa_{4.5}.

***************************************	MnGa _{4.65}	ReGa _{4.5}	
M-M	3.066(7)	3.1276(19)	
M-Ga(1)	2.513(3)	2.591(3)	
M-Ga(2)	2.512(3)	2.594(3)	
M-Ga(3)	2.4334(14)	2.4689(6)	
M-Ga(4)	2.4057(14)	2.4562(6)	
Ga(1)-Ga(1)	2.415(6)	2.424(7)	
Ga(1)-Ga(2)	2.788(5)	2.917(6)	
Ga(1)–Ga(3)	2.858(2)	2.905(3)	
Ga(2)–Ga(2)	2.412(6)	2.419(8)	
Ga(2)-Ga(4)	2.868(3)	2.904(3)	
Ga(3)-Ga(5)	2.796(6)	2.881(5)	
Ga(4)-Ga(5)	2.772(6)	2.870(5)	
Ga(5)-Ga(5)	1.62(2)	1.526(15)	

Table 5-5. Crystal data and structure refinement for Ni_{0.57}Ga_{4.43}.

Empirical formula Ga4.43 Ni0.57

Formula weight 342.30
Temperature 296(2) K

Crystal system Cubic

Space group I23

Unit cell dimensions a = 8.4240(10) Å $\alpha = 90^{\circ}$

b = 8.4240(10) Å $\beta = 90^{\circ}$

c = 8.4240(10) Å $\gamma = 90^{\circ}$

Volume 597.80(12) Å³

Z 8

Density (calculated) 7.607 g/cm³

Absorption coefficient 42.607 mm⁻¹

F(000) 1226

Crystal size $0.082 \times 0.072 \times 0.072 \text{ mm}^3$

Theta range for data collection 3.42 to 28.26°.

Index ranges $-11 \le h \le 11, -10 \le k \le 11, -11 \le l \le 10$

Reflections collected 2475

Independent reflections 245 [R(int) = 0.0504]

Completeness to theta = 28.26° 96.8 %

Refinement method Full-matrix least-squares on F²

Data / restraints / parameters 245 / 0 / 18

Goodness-of-fit on F² 1.093

Final R indices [I>2sigma(I)] R1 = 0.0329, wR2 = 0.0739

R indices (all data) R1 = 0.0445, wR2 = 0.0780

Absolute structure parameter 0.5(4)

Extinction coefficient 0.0022(3)

Largest diff. peak and hole 1.534 and -2.056 e.Å-3

$$R1 = \sum ||F_o| - |F_c|| / \sum |F_o|$$
 and $wR2 = [\sum (|F_o|^2 - F_c|^2)^2 / \sum (wF_o|^2)^2]^{1/2}$

Table 5-6. Atomic coordinates (x 10^4) and equivalent isotropic displacement parameters (2 x 3) for Ni_{0.57}Ga_{4.43}.

	х	у	Z	U(eq)	Occupancy
Ni(1)	-1617(5)	1617(5)	1617(5)	3(1)	0.57
Ga(11)	-1617(5)	1617(5)	1617(5)	3(1)	0.43
Ga(1)	1610(5)	1610(5)	1610(5)	4(1)	
Ga(2)	0	3506(2)	0	11(1)	
Ga(3)	0	5000	2499(2)	11(1)	

U(eq) is defined as one third of the trace of the orthogonalized U^{ij} tensor.

Table 5-7. Anisotropic displacement parameters (Å²x 10³) for Ni_{0.57}Ga_{4.43}.

	U11	U ²²	U33	U ²³	U13	U12
Ga(1)	4(1)	4(1)	4(1)	1(1)	1(1)	1(1)
Ga(2)	12(1)	10(1)	12(1)	0	9(2)	0
Ga(3)	15(1)	15(1)	3(1)	0	0	-3(3)

The anisotropic displacement factor exponent takes the form: $-2\pi^2$ [h^2 $a^{*2}U^{11} + ... + 2h$ k a^* b^* U^{12}]

Table 5-8. Bond distances (Å) for Ni_{0.57}Ga_{4.43}.

Ni-Ga(1)	2.7184(16)
Ni-Ga(1)	2.587(3)
Ga(1)-Ga(2)	2.496(2)
Ga(2)-Ga(2)	2.518(3)
Ga(2)-Ga(3)	2.4540(17)
Ga(2)–Ga(3)	2.4532(17)
Ga(3)-Ga(3)	2.9783(4)

D. Structural Description

MGa_{4.5} (M = Mn, Re): The MGa_{4+x} compounds have a structure (Figure 5-1) that is caught between the PtHg₄ structure of the MGa₄ compounds (Figure 5-2a) and the PdGa₅ structure (Figure 5-2b). In the PtHg₄ structure, the metals reside in the center of gallium cubes. As more gallium is incorporated into the structure, the metal-centered cubes distort into metal-centered square antiprisms connecting along the *c*-axis (Figure 5-3a,b). The squares of the antiprisms in the MGa_{4.5} structure are not quite offset by 45 degrees, as they are in the PdGa₅ structure. This distortion may not be exactly the same for every antiprism, and may lead to the satellite reflections we found in the reciprocal lattice and the superstructure reflections mentioned by Girgis and Schulz.¹¹

In the MGa_{4.5} structure, gallium atoms Ga1 and Ga2 form intra-square bonds (2.788 Å) in one of the antiprism squares. The atoms in the other square, atoms Ga3 and Ga4, are separated beyond Ga–Ga bonding distance (3.1445 Å). In the PdGa₅ structure, all intra-square gallium atoms are separated from each other beyond Ga–Ga bonding distance (3.472 Å). There is inter-square Ga–Ga bonding in both the MGa_{4+x} (Ga1–Ga3 2.858 Å, Ga1–Ga4 2.858 Å, and Ga2–Ga4 2.868 Å) and PdGa₅ structures (Ga2–Ga2 2.858 Å). The antiprisms in PdGa₅ connect to form a rectangular prism that is centered by a gallium atom. In the MnGa_{4.5} structure, the rectangular prism is elongated and centered by a pair of gallium atoms. However, during refinement of the MnGa_{4.5} structure we found that the Ga5 atoms forming this pair are approximately half-occupied. Attempts to place a fully occupied atom at the center of this pair have not been successful.

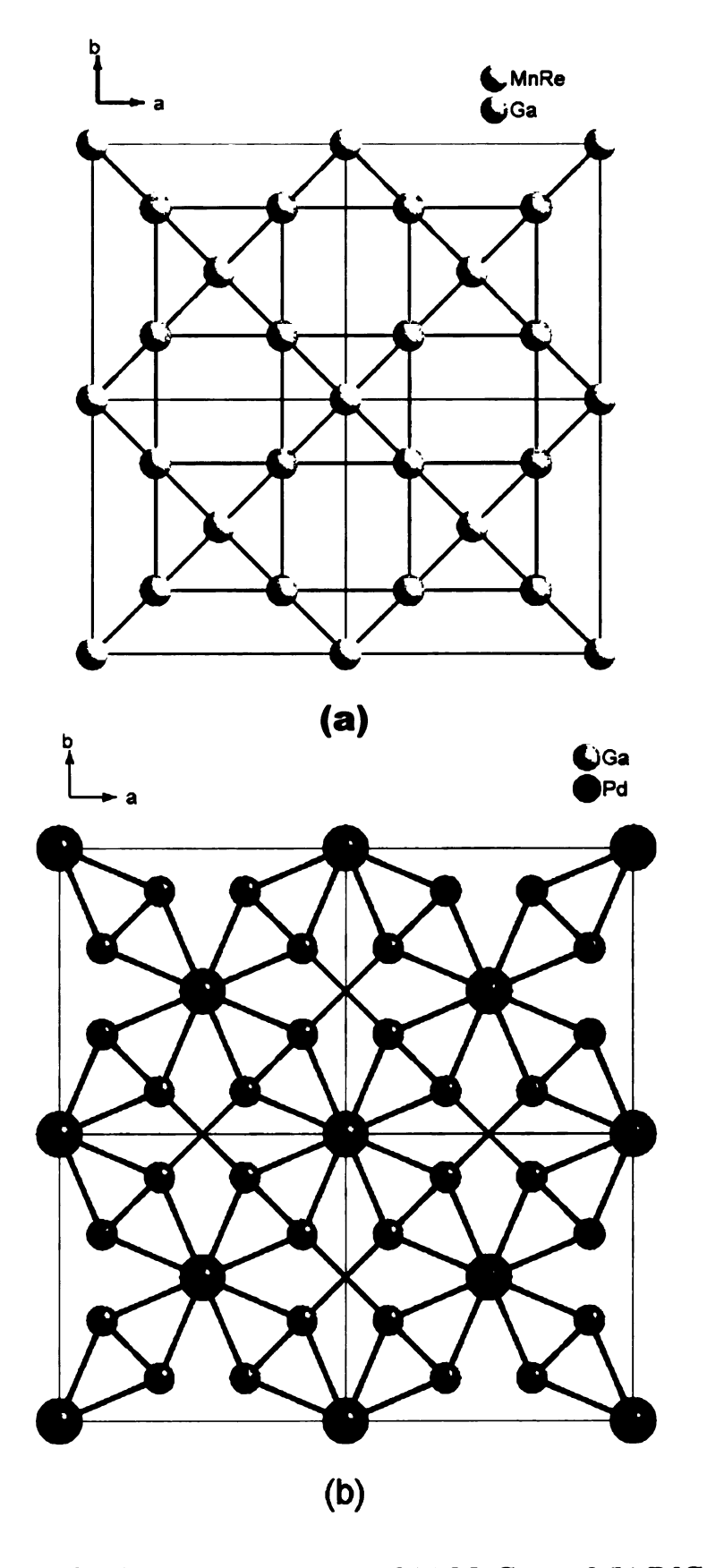
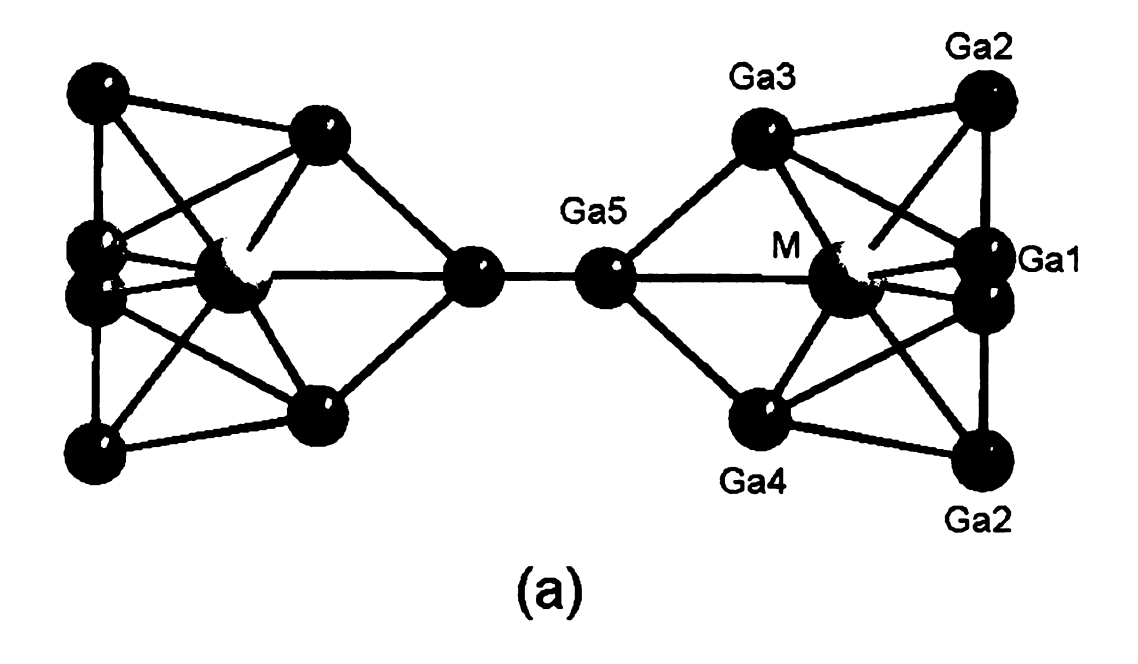


Figure 5-2. View down the c-axis of (a) MnGa₄ and (b) PdGa₅.



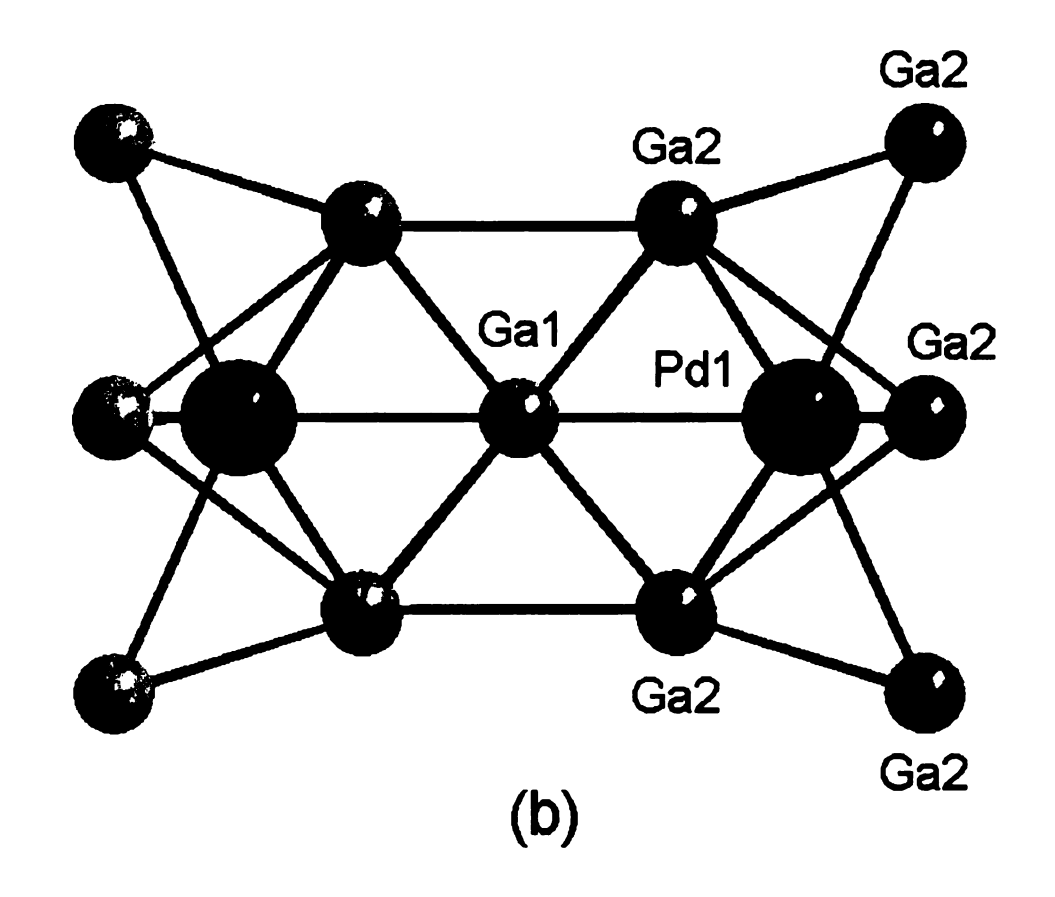


Figure 5-3. Connectivity along the c-axis in (a) MGa_{4.5} and (b) PdGa₅.

Ni_{0.57}Ga_{4.43}: The Ni_{0.57}Ga_{4.43} structure is based on the γ -brass structure.¹³ The structures are composed of a series of body-centered cubes and chains of intersecting rhombi. Ni_{0.57}Ga_{4.43} (Figure 5-1a) and γ -brass (Figure 5-1b) crystallize in different space groups, I23 and I $\overline{4}$ 3m respectively, because of the position the nickel atoms occupy in Ni_{0.57}Ga_{4.43}. As shown in Figure 5-1a, the nickel atoms (Ni1) occupy two corners of the central body-centered cube in the Ni_{0.57}Ga_{4.43} structure, while gallium atoms (Ga1) occupy the other two corners . This lowers the degree of the rotation axis along the *b*-axis from a 4-fold axis to 2-fold axis. This in turn lowers the space group symmetry of Ni_{0.57}Ga_{4.43} from I $\overline{4}$ 3m to I23.

Through occupancy refinements we found that the Ni1 position was split between nickel atoms and gallium atoms. If the Ga1 position had the same mixed occupancy of the Ni1 position, the I 43m symmetry of the parent γ-brass structure would be preserved. The I 43m symmetry could also be preserved if the mixed occupancy site were in the Ga2 position. However, our occupancy refinements for both of these positions found them to be completely occupied by gallium atoms.

The original structural report of NiGa₄ describes the structure as a vacancy controlled γ -brass phase. ¹³ The vacancies in the structure arise because the Ga3 atoms in NiGa₄ would reside in the 12d position of I $\overline{4}$ 3m, instead of the 24g position that the Zn2 atom occupies in the γ -brass structure. This reduces the number of atoms in the unit cell from 52 to 40.

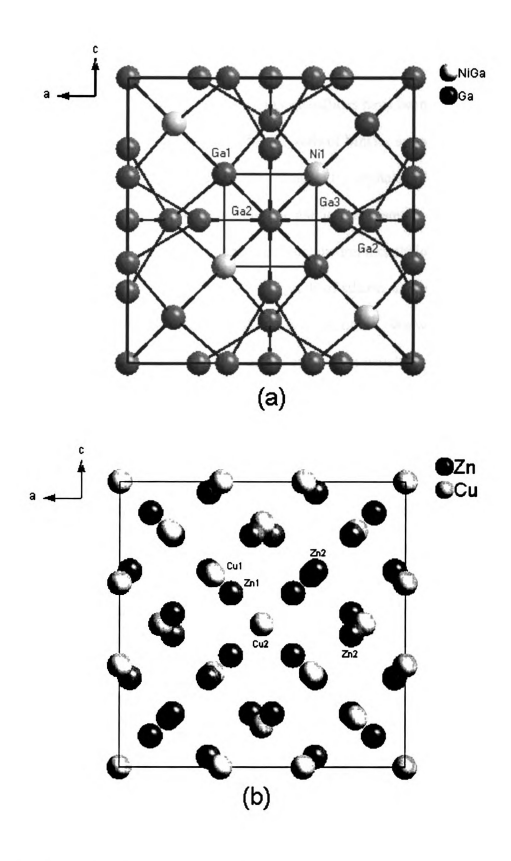


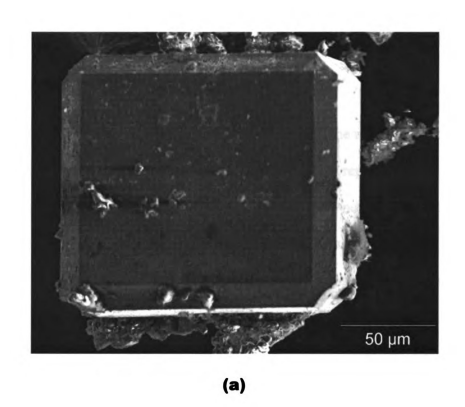
Figure 5-4. (a) Structure of $Ni_{0.57}Ga_{4.43}$ and (b) the parent γ -brass structure.

E. Results and Discussion

As mentioned in Chapter Three, manganese gallides have been isolated from every reaction targeting a manganese boride. Crystals of MnGa₄ are often rectangular plates or prisms (Figure 5-5a), so they can be mistaken for crystals of boride phases we have seen. While we have seen some needle-like and larger prismatic crystals of MnGa_{4.65}, the crystals of this phase often have an octahedral morphology. These octahedral crystals are indistinguishable from crystals of silicon, another common, unintended side product in many of our gallium flux reactions. We were quite lucky to choose a gallide crystal when picking octahedral crystals on which to perform EDS analysis, otherwise, we may have completely overlooked the compound.

After fortuitously finding MnGa_{4.65}, we knew to check the octahedral crystals from rhenium-containing reactions, hoping to find the ReGa_{4.5} analog. We were a bit surprised to find that the rectangular plates and prisms (Figure 5-5b) formed in these reactions were not ReGa₄, because the rhenium- and manganese-containing reactions were carried out under identical conditions. The prisms and plates were the same ReGa_{4.5} phase as the octahedral crystals.

The synthesis of Ni_{0.57}Ga_{4.43} was also a chance occurrence. Our synthesis targeting NiW₂B₁₅ happened to have a heating profile that ended with a hold at 250 °C in order to centrifuge the reaction tube and remove the excess gallium. Our literature search on NiGa₄ later revealed that the compound forms near 250 °C, though single crystals had not yet been isolated.^{6, 13} This may explain why we have not found this product in other reactions, as the centrifugation step was removed from most of the later reaction parameters. The absence of NiGa₄ from other reaction products indicates that the



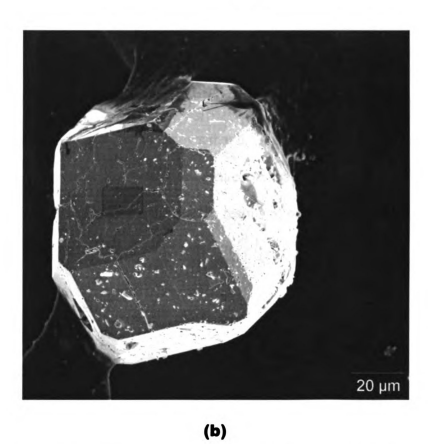


Figure 5-5. SEM micrographs of (a) MnGa₄ and (b) ReGa_{4.5}.

reaction temperature is the most important reaction parameter, and not necessarily the stoichiometry.

The goal of this project was to synthesize borides using the metal flux technique. Therefore, as unintended products to these reactions, the gallides reported here are an interesting side-note to the main focus of this research. We have not yet initiated reactions targeting only these compounds, however such reactions will likely be carried out in the future. Possible physical and electronic properties measurements should provide even more inspiration to conduct further research on this interesting group of gallides.

F. Conclusions

We have synthesized and grown single crystals of MnGa_{4.65}, ReGa_{4.5}, and Ni_{0.57}Ga_{4.43} from gallium flux reactions originally targeting borides. The first structural refinement on MnGa_{4.65} and ReGa_{4.5} shows that the compounds have an intermediate structure between the PtHg₄ and PdGa₅ structures. Single crystal x-ray diffraction analysis of a Ni_{0.57}Ga_{4.43} crystal confirms the results of previous work by Jinkui and Sishen on powder data.

References

- 1. Fisk, Z.; Remeika, J. P., Growth of Single Crystals from Molten Metal Fluxes. In *Handbook on the Physics and Chemistry of the Rare Earths*, ed.; K.A. Gschneidner, J.; Eyring, L., Eds. Elsevier Science: 1989; Vol. 12, pp 53-70.
- 2. Kanatzidis, M. G.; Pöttgen, R.; Jeitschko, W., The Metal Flux- A Preparative Tool for Intermetallic Compounds. *Angewandte Chemie International Edition* **2005**, 44, (43), 6996-7023.
- 3. Lobring, K. C.; Check, C. E.; Zhang, J.; Li, S.; Zheng, C.; Rogacki, K., Single Crystal Growth, Bonding Analysis and Superconductivity of V₂Ga₅. *Journal of Alloys and Compounds* **2002**, 347, 72-78.
- 4. Häussermann, U.; Viklund, P.; Boström, M.; Simak, S. I., Bonding and Physical Properties of Hume-Rothery Compounds with the PtHg₄ Structure. *Physical Review B* **2001**, 63, (12), 125118.
- 5. Häussermann, U.; Boström, M.; Viklund, P.; Rapp, O.; Björnängen, T., FeGa₃ and RuGa₃-Semiconducting Intermetallic compounds. *Journal of Solid State Chemistry* **2002**, 165, 94-99.
- 6. Feschotte, P.; Eggimann, P., Les Systemes Binaries Cobalt-Gallium et Nickel-Gallium Etude Comparee. *Journal of Less-Common Metals* 1974, 63, 15-30.
- 7. X-SHAPE, Version 2.05; STOE & Cie GmbH: 2004.
- 8. X-RED 32, Version 1.10; STOE & Cie GmbH: 2004.
- 9. Sheldrick, G. M. SAINT, Version 4; Siemens Analytical X-Ray Instruments, Inc.: Madison, WI.
- 10. Sheldrick, G. M. SHELXTL Structure Determination Program, Version 5.0; Siemens Analytical X-Ray Instruments, Inc.: Madison, WI, 1995.
- 11. Girgis, K.; Schulz, H., A Gallium-rich Mn-Ga Compound. *Naturwissenschaften* 1971, 58, (2), 95.
- 12. Meissner, H. G.; Schubert, K.; Ananthraman, T. R., The Constitution and Structure of Manganese-Gallium Alloys. *Proceedings of the Indian Academy of Sciences* 1965, 56A, (16), 340-367.
- 13. Jingkui, L.; Sishen, X., The Structure of NiGa₄ Crystal-a New vacancy Controlled γ-Brass Phase. Scientia Sinica 1983, 26A, (12), 1305-1313.

CHAPTER SIX

Conclusions and Future Work

When we began this research, we knew that the metal flux technique had been used with some degree of success in boride synthesis. Much of the preliminary work on metal flux boride synthesis covered the use of aluminum as the flux metal. Our goals were to extend the flux technique to include gallium, and to expand on the work using copper as a flux for boride synthesis. Not only have we synthesized borides using metal fluxes, but we have also learned some of the limitations to using either gallium or copper as a flux.

While we have tried to use gallium to synthesize borides for most of the transition metals, our success has been limited to groups 6 and 7. Crystals of Cr₂B₃, CrB₂, MoB, and WB all grew from reactions targeting ternary borides. We have not yet synthesized a ternary boride from group 6; however, we have grown crystals of group 7 ternary borides. Gallium was used to grow crystals of HoMnB₄, DyReB₄, ErReB₄, and YbReB₄. Binary group 7 borides synthesized in flux reactions are MnB, MnB₄, and ReB₂.

Further research on gallium flux synthesis of group 6 and 7 borides should begin with a focus on reproducing all known binaries for each metal in the groups. This may seem like a trivial task at first, but our synthesis of new phases for MnB and RuB₂ illustrate the possibilities when using a flux to grow known compounds. Exploratory

syntheses of "missing" analogs to known phases can also be carried out during this study.

After the binary systems are well analyzed, the ternary systems can be targeted.

The remaining YCrB₄-type borides for manganese and rhenium should be among the first ternary targets. Commensurate and incommensurate RETM₄B₄ phases are reported for both manganese and rhenium, so the influence of the flux on which phases formed in this stoichiometry would be an interesting study. Exploratory synthesis in ternary systems should also be carried out because of the flux's ability to trap metastable phases that are inaccessible using other synthesis techniques.

When gallium flux reactions were used with metals outside of groups 6 and 7, they tended to include the first row metals. Further research with gallium should include more of the second- and third-row transition metals. Reactions with rhodium, iridium, and platinum would be particularly interesting, since several borides from these metals also include gallium in their structures.² Preliminary reactions with rhodium and iridium have produced thin plates too fragile to study with EDS or single-crystal diffraction.

Rhodium and iridium are also the next metals we would like to investigate using a copper flux. Several ternary rhodium borides have been synthesized using a copper flux,³ but similar work with iridium has not yet been reported. Research targeting just binary borides could be as fruitful as our work with ruthenium. A potential complication is that copper forms ternary borides with rhodium and iridium.⁴

Further research into the ruthenium system still needs to be conducted. Despite synthesizing Ru₇B₃, Ru₂B₃, and two phases of RuB₂, we were unable to isolate Ru₁₁B₈ or RuB_{1.1}. Our studies with the copper flux varied the B:Ru ratio in 1.0 increments. Ru₁₁B₈ and RuB_{1.1} have empirical formulas close enough to other phases that a 1.0 difference in

the B:M ratios between reactions can easily bypass favorable reaction stoichiometries for these phases. Future studies should decrease the difference between B:M ratios of reactions to 0.5 or 0.25.

To study properties of the new β-RuB₂ phase, a little crystal engineering needs to be done. We looked into having microhardness and incompressibility measurements conducted on this phase, but our crystals were too small. Magnetic measurements can also be performed once more crystals are isolated. Electronic structure calculations should be carried out to determine the stability of the ReB₂-structure versus the RuB₂-structure for ruthenium and other metal diborides.

The primary goal in further copper flux syntheses of ternary ruthenium borides should be completing the series of LuRu₄B₄-type compounds. It will be interesting to see if the entire series can be synthesized from a copper flux. Reactions temperatures need to be varied to determine whether Pr and Nd always form the modulated phases from a flux, or if the commensurate phases can be isolated under different reaction parameters. Substitution of other metals for ruthenium presents possible extension of our work.

After synthesizing the LuRu₄B₄-type compounds, more of their physical properties need to be measured. The magnetic properties of these compounds have already been determined from bulk samples, but single crystals will allow us to examine the system more thoroughly, searching for anisotropy in the magnetic ordering. It will also be interesting to compare the results of these studies with a study on LaRu₄B₄, to see if the different connectivity in the Ru₄ tetrahedra influences the magnetic properties.

Copper flux growth of binary niobium borides has been reported,⁵ and we have grown needle-like crystals of Nb₃Co₄B₇. These results indicate that more group 5 borides

should be targeted in copper flux reactions. A few reactions targeting vanadium or tantalum analogs to Nb₃Co₄B₇ have not been successful. Initial attempts to synthesize binary vanadium borides have been unsuccessful, yielding only large crystals of V-doped boron. Initial attempts to synthesize other ternary niobium borides have only produced Nb₃B₄.

One of the most challenging tasks in metal flux synthesis of boride is finding a suitable flux metal for the late first-row transition metals. We were fairly surprised that the copper flux did not produce iron or cobalt borides, considering that both ruthenium and rhodium borides grow from that metal flux. Aluminum, gallium, indium, and tin, though unsuccessful so far, are the metals most likely to produce borides. Canfield has also used Ni₂B to grow quaternary nickel borocarbides, however the isolation calls for decanting the flux while above 1000 °C.

The results presented in this work set a foundation for continued research into the metal flux synthesis of borides. The above suggestions for future work are just a brief glimpse of what could be done in this field.

References

- 1. Zavalii, P. Y.; Mikhalenko, S. I.; Kuz'ma, Y. B., New incommensurate structures of the borides Pr₄₁(Mn₄B₄)₃₅ and Pr₇(Re₄B₄)₆. Journal of Alloys and Compounds **1994**, 203, 55-59.
- 2. Klünter, W.; Jung, W., Ga₈Ir₄B ein Gallium-Iridiumborid mit isolierten, annähernd quadratisch planaren Ir₄B-Gruppen in einer vom CaF₂-Typ abgeleiteten Struktur. Zeitschrift für anorganische und allgemeine Chemie 1995, 621, 197-200.
- 3. Shishido, T.; Ye, J.; Sasaki, T.; Note, R.; Obara, K.; Takahashi, T.; Matsumoto, T.; Fukuda, T., Growth of Single Crystals in the Systems with R-Rh-B and r-Rh-B-C (R= Rare Earth Element) from Molten Copper Flux. *Journal of Solid State Chemistry* 1997, 133, 82-87.
- 4. Klünter, W.; Jung, W., The Copper Iridium Boride Cu₂Ir₄B₃ with a Layered Structure Derived from teh ZnIr₄B₃ Type. Zeitschrift für anorganische und allgemeine Chemie **2000**, 626, 502-505.
- 5. Okada, S.; Hamano, K.; Lundström, T.; Higashi, I. In Crystal Growth of the New Compound Nb₂B₃, and the Borides NbB, Nb₅B₆, Nb₃B₄, and NbB₂, Using the Copper-Flux Method, Boron-Rich Solids, Albuquerque, New Mexico, 1986, 1985; Emin, D.; Aselage, T.; Beckel, C. L.; Howard, I. A.; Wood, C., Eds. American Institute of Physics: Albuquerque, New Mexico, 1985; pp 456-459.
- 6. Canfield, P. C.; Fisher, I. R., High-Temperature Solution Growth of Intermetallic Single Crystals and Quasicrystals. *Journal of Crystal Growth* **2001**, 225, 155-161.

Appendix

RF Furnace Design and Setup

The RF furnace has been a vital instrument for high-temperature synthesis in our group for a number of years. However, several issues repeatedly arose and led to a redesign of the furnace. A brief examination of the previous design and the associated problems help illustrate the benefits of the new design.

In the previous design, a thin sheet of molybdenum foil was wrapped around a reaction crucible to act as a susceptor to the magnetic fields generated by the copper induction coil. The crucible and susceptor were then balanced in a small mullite tube packed with insulating wool. The tube was placed into a pyrex reaction chamber, which was also packed with insulating wool. A flow of argon was introduced into the reaction chamber and upon turning on the power to the induction coil heating commenced.

The main problem with the previous design was that the crucible and susceptor would frequently tip over and contact the reaction chamber. The reaction chamber would then crack because of the extreme heat of the susceptor. The chamber also cracked a few times because the insulating wool was packed too tightly and expanded slightly on heating. Another small problem was that the molybdenum foil became brittle after several reactions, and new pieces had to be used often. These problems and the inability to run reactions under vacuum led to the new furnace design.

The new RF furnace has a reaction chamber made of fused quartz, which is more thermally stable than the previous pyrex chamber. A boron nitride cylinder (Figure A-1a) has replaced the insulating wool and mullite tube from the previous furnace. The cylinder is centered along the central axis of the reaction chamber by a small dimple in the floor of the chamber. Instead of using molybdenum foil as a susceptor, we machined a crucible holder from a molybdenum cylinder (Figure A-1b,c) capable of holding crucibles of different sizes. The crucible holder sits on the BN cylinder and is more stable than the molybdenum foil. Many reactions have been run and the new crucible holder / susceptor is still working quite well.

In order to run reactions under vacuum, we installed a three-way valve that opens the reaction chamber to a gas flow or a vacuum pump. With this design the chamber can be filled and purged several times before the reaction is initiated. T-joints have been added to the gas lines, allowing for argon, nitrogen, or a mix of the two to be used for flushing the chamber or during reactions. Running reactions under dynamic vacuum slows the deposition of films on the inside of the reaction chambers. This allows the thermometer to have a clear view of the crucible and susceptor, resulting in more accurate temperature monitoring.

While the design of several components has changed, the overall setup of the RF furnace has not changed (Figure A-2). The reaction chamber is placed in the induction coil, with the susceptor located in the middle of the induction coil. The induction coil is connected to a remote power station, which is controlled by the main control unit. The reaction temperatures are monitored with an IR thermometer aimed between the copper tubing and reported on a furnace controller connected to the thermometer.

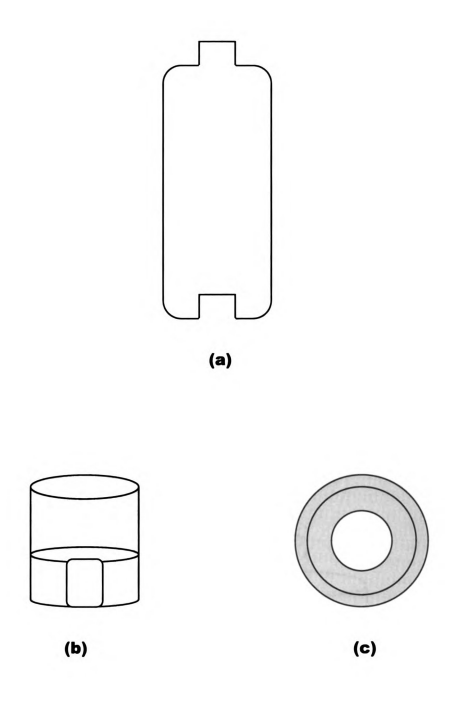


Figure A-1. Cross-sectional view of (a) BN susceptor holder and Mo susceptor along (b) vertical and (c) horizontal axes.

